



THE HONG KONG
POLYTECHNIC UNIVERSITY

香港理工大學

Pao Yue-kong Library

包玉剛圖書館

Copyright Undertaking

This thesis is protected by copyright, with all rights reserved.

By reading and using the thesis, the reader understands and agrees to the following terms:

1. The reader will abide by the rules and legal ordinances governing copyright regarding the use of the thesis.
2. The reader will use the thesis for the purpose of research or private study only and not for distribution or further reproduction or any other purpose.
3. The reader agrees to indemnify and hold the University harmless from and against any loss, damage, cost, liability or expenses arising from copyright infringement or unauthorized usage.

IMPORTANT

If you have reasons to believe that any materials in this thesis are deemed not suitable to be distributed in this form, or a copyright owner having difficulty with the material being included in our database, please contact lbsys@polyu.edu.hk providing details. The Library will look into your claim and consider taking remedial action upon receipt of the written requests.

**SILK FIBROIN-BASED NANOPARTICLES DRUG
DELIVERY SYSTEM BY SUPERCRITICAL CO₂
TECHNOLOGY**

ZHAO ZHENG

Ph.D

The Hong Kong Polytechnic University

2013

THE HONG KONG POLYTECHNIC UNIVERSITY
INSTITUTE OF TEXTILES AND CLOTHING

SILK FIBROIN-BASED NANOPARTICLES DRUG
DELIVERY SYSTEM BY SUPERCRITICAL CO₂
TECHNOLOGY

ZHAO ZHENG

A thesis submitted in partial fulfilment of the requirements for
the degree of Doctor of Philosophy

September 2012

CERTIFICATE OF ORIGINALITY

I hereby declare that this thesis is my own work and that, to the best of my knowledge and belief, it reproduces no material previously published or written, nor material that has been accepted for the award of any other degree or diploma, except where due acknowledgement has been made in the text.

_____ (Signed)

ZHAO ZHENG (Name of student)

ABSTRACT

Current cytotoxic chemotherapy in the field of biomedical engineering, especially cancer therapy has been limited by poor efficiency and high toxicity due to immediate drug release, non-specific tissue distribution, degradation by chemical and enzymatic hydrolysis, and low cellular uptake efficiency. The purposes of this study were to develop a silk fibroin-based nanoparticles drug delivery system by supercritical CO₂ technology to decrease the adverse side effects of the drugs and enhance drug performance.

To achieve the objectives of the research, in the first part, silk fibroin (SF) nanoparticles were fabricated via solution-enhanced dispersion by supercritical CO₂ (SEDS) for the first time successfully. The influence of process parameters on particle size and SF nanoparticles formation mechanism were investigated. The results indicated that precipitation temperature, concentration and flow rate of SF solution have a positive effect, while precipitation pressure has a negative effect. The nanoparticle formation mechanism was elucidated with the formation and growth of silk fibroin nuclei in the gaseous miscible phase evolved from initial droplets generated by the liquid-liquid phase split.

Secondly, to characterize silk fibroin (SF) nanoparticles and explore their application in drug delivery systems, ethanol was used to treat drug loaded SF nanoparticles for inducing water insolubility. The SF nanoparticles demonstrated excellent biocompatibility, time-dependent and concentration-dependent cellular uptake properties, and thus can be used as

drug carrier. However, the drug leakage is a critical issue in the process of ethanol treatment.

Thirdly, in order to overcome the disadvantages of SF nanoparticles and develop a novel SF/PPP nanoparticles drug carrier with the advantages of natural SF and synthetic PLLA-PEG-PLLA (PPP) polymer, a modified SEDS process was designed to prepare the SF/PPP composite nanoparticles. The results of biological evaluation showed that the silk fibroin can improve the property of PPP as drug carrier. SF/PPP nanoparticles possessed much better biocompatibility and can accelerate cell adhesion and internalization compared with PPP nanoparticles.

Furthermore, in order to study the application of SF/PPP nanoparticles in cancer therapy, anti-cancer drug, paclitaxel (PTX) was loaded into SF/PPP nanoparticles by the SEDS process. The resulting PTX loaded SF/PPP (PTX-SF/PPP) nanoparticles do not need induction of water solubility so that the drug loss of PTX loaded silk fibroin nanoparticles in post-treatment can be avoided. PTX-SF/PPP nanoparticle could enhance the solubility of PTX and exhibited controlled drug release property. Especially the drug release rate in PBS solution could be accelerated with decrease of the pH value from 7.4 to 6.0. This property can benefit the tumor-specific therapy due to the unique tumor environment. MTS assay demonstrated *in vitro* anti-tumor activity of the PTX-SF/PPP nanoparticles for MCF-7 and HePG-2 cells after one week was slightly higher than that of free PTX. In terms of the characteristics of

nanoparticles, PTX-SF/PPP nanoparticles have potential application in the field of tumor therapy.

Finally, in order to enhance the targeting efficiency of the SF/PPP nanoparticles to the tumor site, a tumor-specific ligand, folic acid (FA), was grafted onto the surface of the SF/PPP nanoparticles successfully by conjugation of the amino group on the silk fibroin with the carboxylic group of folic acid activated by EDC/NHS. Flow cytometric analysis showed that the FA-SF/PPP possessed a higher cellular uptake by MCF-7 tumor cell than SF/PPP nanoparticles. However, MTS assay indicated that *in vitro* anti-tumor activity had no significant difference between PTX-loaded FA-SF/PPP and PTX-loaded SF/PPP nanoparticles. Due to the tumor-targeted delivery, high drug load and controlled drug release property, the PTX-FA-SF/PPP nanoparticles can be utilized as an effective drug delivery system for tumor targeted therapy.

In conclusion, silk fibroin-based nanoparticles drug delivery systems including SF, SF/PPP, and FA-SF/PPP nanoparticles have been developed by supercritical CO₂ technology successfully. These nanostructured drug delivery systems have potential application in the field of biomedical engineering, especially cancer therapy.

PUBLICATIONS ARISING FROM THE THESIS

Refereed journal articles:

- [1] **Zhao Z**, Li Y, Chen AZ, Zheng ZJ, Hu JY, Li JS, Li G. Generation of Silk Fibroin Nanoparticles via Solution-Enhanced Dispersion by Supercritical CO₂. *Industrial & Engineering Chemistry Research* 2013; 52: 3752-3761 (SCI: 2.237).
- [2] **Zhao Z**, Chen AZ, Li Y, Hu JY, Liu X, Li JS, Zhang Y, Li G, Zheng ZJ. Fabrication of Silk Fibroin Nanoparticles for Controlled Drug Delivery. *Journal of Nanoparticle Research* 2012; 14:736-745 (SCI: 3.287).
- [3] **Zhao Z**, Zhang Y, Chen AZ, Li Yi, Liu X, Li JS, Zheng ZJ. Preparation and Characterization of Paclitaxel Loaded PLLA-PEG-PLLA Nanoparticles for Control Release of Anticancer Drugs Using Solution-Enhanced Dispersion in Supercritical CO₂. *Journal of Controlled Release, supplement* 2012 (accepted).
- [4] Chen AZ, **Zhao Z**, Wang SB, Li Y, Zhao C, Liu YG. A Continuous RESS Process to Prepare PLA-PEG-PLA Microparticles. *The Journal of Supercritical Fluids* 2011; 59: 92-97 (SCI: 2.860).
- [5] Chen AZ, Li L, Wang SB, Lin XF, Liu YG, Zhao C, Wang GY, **Zhao Z**. Study of Fe₃O₄-PLLA-PEG-PLLA Magnetic Microspheres Based on Supercritical CO₂: Preparation, Physicochemical Characterization, and Drug Loading Investigation. *The Journal of Supercritical Fluids* 2012; 67: 139-148 (SCI: 2.860).

- [6] Chen AZ, Li L, Wang SB, Zhao C, Liu YG, Wang GY, **Zhao Z**.
Nanonization of Methotrexate by Solution-Enhanced Dispersion by
Supercritical CO₂. The Journal of Supercritical Fluids 2012; 67: 7-13 (SCI:
2.860)

Referred conference papers:

- [1] **Zhao Z**, Chen AZ, Li Y, Hu JY, Liu X, Li JS, Zhang Y, Li G, Zheng ZJ.
Formation of Silk Fibroin Nanoparticles for Controlled Drug Delivery
Using Supercritical CO₂ Technique. 4th International Conference on Drug
Discovery and Therapy. February 12~15, 2012 at Dubai Men's College in
Dubai, UAE.
- [2] **Zhao Z**, Li Yi, Zhang Y, Chen AZ, Li JS, Liu X, Hu JY, Zheng ZJ.
Experimental Investigation on Controlling Size of Silk Fibroin
Nanoparticles in Supercritical CO₂ Process. TBIS 2012 International
Symposium, "Kansei and Bioengineering: Creating New Fiber-Textile
Science and Technology" in August 9-11, 2012 at Shinshu University in
Ueda, Japan.
- [3] **Zhao Z**, Zhang Y, Chen AZ, Li Yi, Liu X, Li JS, Zheng ZJ. Preparation and
Characterization of Paclitaxel Loaded PLLA-PEG-PLLA Nanoparticles for
Control Release of Anticancer Drugs Using Solution-Enhanced Dispersion
in Supercritical CO₂. Symposium on Innovative Polymers for Controlled
Delivery (SIPCD 2012). September 11~14, 2012 at Soochow University in
Suzhou, China.

Patents:

[1] Li Y, **Zhao Z**. Method to fabricate silk fibroin with different morphology.

China invention patents, 20100609121.8

[2] Chen AZ, Wang SB, **Zhao Z**, Li Y, Liu YG. A continuous RESS process to

prepare polymer or drug loaded polymer particles, China invention patents,

201110269946.4.

ACKNOWLEDGMENTS

First of all, I would like to express my most sincere thanks to my chief supervisor, Prof. Yi Li, the Institute of Textiles and Clothing, for giving me the opportunity to do this interesting and promising research. Without his constant guidance, insightful suggestions, encouragement, and patience, this research would not be completed. He taught me research methodology and how to develop the scientific evidence to prove or disprove a hypothesis. His enthusiasm on scientific pursuit and indefatigable dedication on academic research have always been a great inspiration for me.

I am also deeply grateful to my co-supervisors, Dr. Aizheng Chen, College of Chemical Engineering, Huaqiao University, who brought me to this interesting research field and tried his best to help me solve the problem in the research. Dr. Chen has been a friend and mentor. I have learned a lot from his scientific thought and lifestyle. Without his valuable guidance and constructive suggestions, completion of PhD study could not be possible. I would also like to express my sincere thanks to my Co-supervisor, Dr. Zijian Zheng, for his support and kind guidance throughout the research work. His warm encouragement and outstanding scientific achievement brought me great confidence.

I would like to give my sincere thanks to Dr. Yu Zhang for her kind help and suggestions throughout the research work. Especially, she provided me with

excellent technical support and shared many research results, constructive suggestions about biological evaluation of nanoparticles.

Special thanks must also go to Dr. Li Jiashen, Dr. Junyan Hu, Mrs. Yanxia Han, Ms. Xuan Liu, Mr. Xuqing Liu, Ms. Jing Zhang, Mr. Zhi Li, Ms. Yi Teng, Ms. Jiao Jiao, Mr. Long Wu and Mr. Guanxiang Yuan for their kindly help and valuable suggestions on my research, as well as enriching my life.

I would like to thank Hong Kong Innovation and Technology Commission and Hong Kong Research Institute of Textile and Apparel for providing funding support to this research through projects ITP/001/07TP, ITP/031/08TP, the Hong Kong Research Grant Council and the Hong Kong Polytechnic University through projects PolyU5242/09E, G-YX1M, J-BB6Q and GU942. Also, we would like to thank the support of Guangdong Provincial Department of Science and Technology through the Guangdong-Hong Kong International Textile Bioengineering Joint Research Center with project code 2011B050300023, as well as the sponsorship from Hong Kong Jockey Club Sports Medicine and Health Science Center.

Finally, I wish to express my loving thanks to my dear parents. Without their unconditional love, support, sacrifice throughout my life, I could not have gone so far and completed my PhD work.

TABLE OF CONTENTS

ABSTRACT	I
PUBLICATIONS ARISING FROM THE THESIS	IV
ACKNOWLEDGMENTS	VII
TABLE OF CONTENTS	IX
LIST OF FIGURES	XIV
LIST OF TABLES	XXIV
LIST OF ABBREVIATIONS	XXV
Chapter 1 Introduction	1
1.1 Background	1
1.2 Project objectives	4
1.3 Project significance and originality.....	5
1.4 Research methodology	5
1.4.1 Nanoparticle formation technology.....	6
1.4.2 Characterization of nanoparticles.....	6
1.4.3 Drug loading and <i>in vitro</i> release properties	7
1.4.4 Biological evaluation of nanoparticles	7
1.5 Thesis outline	8
Chapter 2 Literature review	11
2.1 Nanoparticle drug delivery system for tumor therapy	11
2.1.1 Tumor therapy	11
2.1.2 Nanoparticle drug delivery system.....	12
2.2 Polymer nanoparticles	16
2.2.1 Silk fibroin (SF) nanoparticles	18
2.2.2 Silk fibroin /PLLA-PEG-PLLA (SF/PPP) nanoparticles	20
2.2.3 Tumor targeted SF/PPP nanoparticles.....	22
2.3 Nanoparticle preparation technology	25
2.3.1 Emulsification/solvent evaporation.....	25
2.3.2 Salting out	26

2.3.3	Nanoprecipitation (or solvent displacement method)	27
2.3.4	Spray drying	27
2.4	Supercritical fluid technology	29
2.4.1	Rapid expansion of supercritical solutions (RESS)	31
2.4.2	Gas-saturated solutions or suspensions (PGSS).....	33
2.4.3	Anti-solvent precipitation.....	35
2.5	Application of the SEDS process in formation of polymer nanoparticle drug delivery systems	41
2.6	Summary of research gaps	46
Chapter 3	Study on formation of silk fibroin nanoparticles by the SEDS process.....	48
3.1	Introduction	48
3.2	Experimental Section	49
3.2.1	Materials.....	49
3.2.2	Preparation of pure silk fibroin (SF) raw material	49
3.2.3	Preparation of silk fibroin nanoparticles by the SEDS process.....	49
3.2.4	Full factorial designs (FFD).....	51
3.2.5	Surface morphology and particle size	52
3.3	Results and discussion.....	53
3.4	Surface morphology, particle size and particle size distribution of silk fibroin nanoparticles	53
3.5	Influence of the process process parameters on particle size and particle size distribution.....	56
3.6	Silk fibroin nanoparticle formation mechanism.....	59
3.6.1	Effect of flow rate of solution	60
3.6.2	Effect of the concentration of solution.....	62
3.6.3	Effect of precipitation pressure	63
3.6.4	Effect of precipitation temperature	65
3.6.5	Silk fibroin nanoparticle formation mechanism.....	66
3.7	Summary	68

Chapter 4	Characterization of silk fibroin nanoparticles and their potential application as drug carrier.....	70
4.1	Introduction.....	70
4.2	Preparation of SF nanoparticles and drug loaded SF nanoparticles by the SEDS process.....	71
4.3	Surface morphology and particle size distribution.....	71
4.4	Chemical and physical properties	73
4.4.1	FTIR analysis	73
4.4.2	XRPD analysis	74
4.4.3	Thermal properties	76
4.5	Biological evaluation of SF nanoparticles	78
4.5.1	Cell culture.....	78
4.5.2	MTS assay.....	78
4.5.3	LDH assay.....	82
4.5.4	Cellular uptake study.....	85
4.6	Drug loading and <i>in vitro</i> release properties	90
4.6.1	UV-Vis/HPLC assay for PTX.....	90
4.6.2	UV-vis spectrophotometer analysis for IDMC	92
4.6.3	Drug load (DL) and encapsulation efficiency (EE)	93
4.6.4	<i>In vitro</i> drug release	96
4.7	Summary	98
Chapter 5	Development of silk fibroin modified PLLA-PEG-PLLA (SF/PPP) nanoparticles in supercritical CO₂	100
5.1	Introduction.....	100
5.2	Preparation of SF/PPP composite nanoparticles by the SEDS process..	101
5.2.1	Method 1: Co-precipitation of SF/PPP from a homogeneous solution ..	101
5.2.2	Method 2: Precipitation of SF/PPP from a suspended solution	102
5.3	Surface morphology and particle size distribution.....	104
5.4	Chemical and physical properties	107
5.4.1	FTIR analysis	107
5.4.2	XRPD analysis	108

5.5	Biological evaluation of SF/PPP nanoparticles.....	110
5.5.1	MTS assay.....	110
5.5.2	LDH assay.....	112
5.5.3	Cellular uptake of SF/PPP nanoparticles	114
5.6	Summary	120
Chapter 6	Preparation, characterization and <i>in vitro</i> anti-tumor activity of PTX-SF/PPP nanoparticles	121
6.1	Introduction.....	121
6.2	Preparation of PTX-SF/PPP nanoparticles by the SEDS process	122
6.3	Surface morphology and structure of PTX-SF/PPP nanoparticles.....	123
6.4	Chemical and physical characterization.....	125
6.4.1	FTIR analysis	125
6.4.2	XRPD analysis	126
6.5	Drug loading and <i>in vitro</i> release properties	127
6.5.1	Drug load (DL) and encapsulation efficiency (EE)	127
6.5.2	<i>In vitro</i> drug release	127
6.6	<i>In vitro</i> cytotoxicity activity.....	129
6.6.1	MTS assay.....	129
6.6.2	Live/dead assay	136
6.7	Summary	140
Chapter 7	Preparation, characterization and <i>in vitro</i> anti-tumor activity of smart PTX-FA-SF/PPP nanoparticles	141
7.1	Introduction.....	141
7.2	Fabrication of PTX-FA-SF/PPP nanoparticles	142
7.3	Surface morphology and particle size distribution.....	144
7.4	Chemical properties	145
7.4.1	FTIR analysis	145
7.4.2	Determination of folic acid content.....	146
7.5	Drug load, encapsulation efficiency, and <i>in vitro</i> drug release property	149
7.5.1	Drug load and encapsulation efficiency	149
7.5.2	<i>In vitro</i> drug release	150

7.6	Tumor targeting analysis.....	151
7.7	<i>In vitro</i> cytotoxicity study	158
7.7.1	<i>In vitro</i> cytotoxicity to MCF-7 cells.....	158
7.7.2	<i>In vitro</i> cytotoxicity to HFF-1 cells.....	162
7.7.3	Comparsion of cytotoxicity to MCF-7 and HFF-1 cells	164
7.8	Summary	167
Chapter 8	Conclusion and suggestions for future work	168
8.1	Conclusion	168
8.2	Suggestions for future research.....	172
References	175

LIST OF FIGURES

Figure 1.1 Schematic research framework and thesis outline.....	8
Figure 2.1 Plasma drug concentration profiles for (a) conventional immediate release formulation (IR) and (b) controlled release formulation (CR).....	15
Figure 2.2 Advantages of using nanoparticles drug delivery system for cancer therapy compared to free drug [41]	16
Figure 2.3 Schematic representation of a pure fluid in the P-T phase diagram [103].....	30
Figure 2.4 Schematic illustration of the RESS technique [114]	32
Figure 2.5 Schematic illustration of the PGSS technique [114]	34
Figure 2.6 Schematic illustration of the batch GAS technique [103]	36
Figure 2.7 Schematic illustration of the ASES techniques [121].....	37
Figure 2.8 Schematic illustration of a typical continuous SAS process [105]	38
Figure 2.9 Schematic illustration of the SEDS process and co-axial nozzle [114]	40
Figure 2.10 Three coaxial-passages nozzle [127]	41
Figure 3.1 Schematic diagram of the apparatus for the SEDS process.....	50
Figure 3.2 FE-SEM photos of silk fibroin nanoparticles prepared by the SEDS process under different concentration of silk fibroin (a) 45 °C-0.5% SF-20 MPa-1 ml min ⁻¹ , (b) 45 °C-0.5% SF-20 MPa-0.5	

ml min ⁻¹ , (c) 35 °C-0.5% SF-20 MPa-0.5 ml min ⁻¹ , (d) 35°C-1% SF-20 MPa-0.5 ml min ⁻¹ , (e) 45 °C-1% SF-10 MPa-1 ml min ⁻¹ , (f) 45 °C-1% SF-20 MPa ⁻¹ ml min ⁻¹ , (g) 45 °C-0.5%SF-10 MPa-1 ml min ⁻¹ and (d) 35 °C-0.5% SF-10 MPa-1 ml min ⁻¹	55
Figure 3.3 Standardized effect of the factors on (a) particle size and (b) main effects plot for particle size	57
Figure 3.4 Standardized effect of the factors on (a) particle size distribution and (b) main effects plot for particle size distribution	58
Figure 3.5 Mechanism for (a) main effects of the flow rate and (b) concentration of solution on the particle size of silk fibroin nanoparticles in the SEDS process.....	61
Figure 3.6 Mechanism for (a) main effects of precipitation pressure and (b) temperature on the particle size of silk fibroin nanoparticles in the SEDS process.....	64
Figure 3.7 Mechanism diagram for silk fibroin particle formation by the SEDS process	68
Figure 4.1 FE-SEM images of SF nanoparticles (a) before ethanol treatment and (b) after ethanol treatment	72
Figure 4.2 Particle size distribution of SF nanoparticles dispersed in ethanol	72
Figure 4.3 FTIR spectras of SF nanoparticles before and after ethanol treatment.....	74

Figure 4.4 XRPD patterns of silk fibroin nanoparticles before and after ethanol treatment.....	76
Figure 4.5 TG-DSC curves of silk fibroin nanoparticles before and after ethanol treatment.....	77
Figure 4.6 Cell proliferation of fibroblasts incubated with SF nanoparticles for 1 day, 3 days and 7 days measured with a MTS cell proliferation assay. The data are expressed as mean \pm standard deviation (SD) of three independent experiments. An OD value of control cells (untreated cells) was taken as 100% viability (0% cytotoxicity). p-values: # < 0.01; * < 0.05.	81
Figure 4.7 Cell proliferation of fibroblasts incubated with SF nanoparticles for 1 day, 3 days and 7 days measured with LDH assay. p-values: # < 0.01; * < 0.05.	84
Figure 4.8 Fluorescence microscopy images of filamentous actin (red) and nucleus (blue) stained fibroblasts incubated with 100 μ g/ml SF nanoparticles (green) for 0.5 hours (a) DAPI Channel, (b) FITC Channel, (c) TRITC Channel, (d) Merged Image	87
Figure 4.9 Fluorescence microscopy images of filamentous actin (red) and nucleus (blue) stained fibroblasts incubated with 10 μ g/ml SF nanoparticles (green) for 24 hours (a) DAPI Channel, (b) FITC Channel, (c) TRITC Channel, (d) Merged Image	88
Figure 4.10 Fluorescence microscopy images of filamentous actin (red) and	

nucleus (blue) stained fibroblasts incubated with 100 $\mu\text{g/ml}$ SF nanoparticles (green) for 24 hours (a) DAPI Channel, (b) FITC Channel, (c) TRITC Channel, (d) Merged Image	89
Figure 4.11 Fluorescence microscopy images of filamentous actin (red) and nucleus (blue) stained fibroblasts incubated with 1000 $\mu\text{g/ml}$ SF nanoparticles (green) for 24 hours (a) DAPI Channel, (b) FITC Channel, (c) TRITC Channel, (d) Merged Image	89
Figure 4.12 Chromatogram for standard solutions of PTX in acetonitrile/water (50:50 v/v).....	91
Figure 4.13 Calibration curve of PTX determined by UV-Vis/HPLC analysis	92
Figure 4.14 Calibration curve of IDMC determined by UV-spectrophotometric analysis	93
Figure 4.15 Drug release curves of IDMC from IDMC-SF nanoparticles obtained by the SEDS process (Each point represents the mean \pm standard deviation obtained from triplicates of the samples).....	98
Figure 5.1 Schematic diagram of the SEDS apparatus for preparation of silk fibroin/PPP composite particle.....	103
Figure 5.2 FE-SEM photographs of samples obtained by method 1 (a) SF/PPP composite samples and (b) PPP nanoparticles	104
Figure 5.3 SEM photographs of samples obtained by method 2 (a) SF nanoparticles, (b) PPP nanoparticles, (c) and (d) SF/PPP nanoparticles	

.....	105
Figure 5.4 Particle size distribution of SF/PPP nanoparticles.....	105
Figure 5.5 TEM photographs of SF/PPP nanoparticles	106
Figure 5.6 FTIR spectras of original PPP, SF nanoaprticles, and SF/PPP nanoparticles in the supercritical process.....	108
Figure 5.7 XRPD pattens of original PPP, SF nanoaprticles, and SF/PPP nanoparticles in the supercritical process.....	109
Figure 5.8 Cell proliferation of fibroblasts incubated with PPP nanoparticles and SF/PPP composite nanoparticles for 1 day, 3 days and 7 days measured with a MTS cell proliferation assay.p-values: # < 0.01; * < 0.05.....	111
Figure 5.9 Cell proliferation of fibroblasts incubated with SF nanoparticles for 1 day, 3 days and 7 days measured with LDH assay. p-values: # < 0.01; * < 0.05	112
Figure 5.10 Fluorescence microscopy images of filamentous actin (red) and nucleus (blue) stained fibroblasts incubated with 100 µg/ml SF/PPP nanoparticles (green) for 30 minutes (a) DAPI Channel, (b) FITC Channel, (c) TRITC Channel, (d) Merged Image	114
Figure 5.11 Fluorescence microscopy images of filamentous actin (red) and nucleus (blue) stained fibroblasts incubated with 100 µg/ml SF/PPP nanoparticles (green) for 24 hours (a) DAPI Channel, (b) FITC Channel, (c) TRITC Channel, (d) Merged Image	115

Figure 5.12 Fluorescence histograms of HFF-1 cells incubated with PPP nanoparticles for 0.5h, 4h and 24h.....	117
Figure 5.13 Fluorescence histograms of HFF-1 cells incubated with SF/PPP nanoparticle for 0.5h, 4h and 24h.....	117
Figure 5.14 Fluorescent intensity measurements normalized by the number of HFF-1 cells incubated with PPP nanoparticles for 0.5h, 4h and 24h	118
Figure 5.15 Fluorescent intensity measurements normalized by the number of HFF-1 cells incubated with SF/PPP nanoparticles for 0.5h, 4h and 24h.....	118
Figure 6.1 FE-SEM photographs of PTX-SF/PPP obtained by the SEDS process (a) 20000 × and (b) 40000 ×.....	123
Figure 6.2 Particle size distribution of PTX-SF/PPP obtained by the SEDS process.....	124
Figure 6.3 FTIR spectras of PTX, SF/PPP nanoparticles, physical mixture of PTX and SF/PPP nanoparticles, and PTX-SF/PPP nanoparticles.....	125
Figure 6.4 XRPD patterns of free PTX, SF/PPP and PTX-SF/PPP prepared by the SEDS process	126
Figure 6.5 <i>In vitro</i> release profile of PTX from PTX-SF/PPP nanoparticles in PBS buffer (pH 6.0 and 7.4).....	128
Figure 6.6 Cell viability of MCF-7 cells incubated with nanoparticles for 1, 2, 3, 5 and 7 days.....	130

Figure 6.7 Optical images of MCF-7 cells incubated with 0.5 $\mu\text{g/ml}$ SF/PPP nanoparticles for (a) 1 day, (b) 2 days and (c) 5 days	132
Figure 6.8 Optical images of MCF-7 cells incubated with 0.5 $\mu\text{g/ml}$ PTX for (a) 1 day, (b) 2 days and (c) 5 days	132
Figure 6.9 Optical images of MCF-7 cells incubated with 0.5 $\mu\text{g/ml}$ PTX-SF/PPP nanoparticles for (a) 1 day, (b) 2 days and (c) 5 days ...	133
Figure 6.10 Cell viability of HePG-2 cells incubated with nanoparticles for 1, 2, 3, 5 and 7 days.....	133
Figure 6.11 Optical images of HePG-2 cells incubated with 0.5 $\mu\text{g/ml}$ SF/PPP nanoparticles for (a) 1 day, (b) 2 days and (c) 5 days	134
Figure 6.12 Optical images of HePG-2 cells incubated with 0.5 $\mu\text{g/ml}$ PTX nanoparticles for (a) 1 day, (b) 2 days and (c) 5 days	135
Figure 6.13 Optical images of HePG-2 cells incubated with 0.5 $\mu\text{g/ml}$ PTX-SF/PPP nanoparticles for (a) 1 day, (b) 2 days and (c) 5 days ...	135
Figure 6.14 Live/Dead images of MCF-7 cells incubated with control (blank) for 24 hours (a) live cell and (b) dead cells.....	138
Figure 6.15 Live/Dead images of MCF-7 cells incubated with free PTX for 24 hours (a) live cell and (b) dead cells	138
Figure 6.16 Live/Dead images of MCF-7 cells incubated with SF/PPP-PTX nanoparticles for 24 hours (a) live cell and (b) dead cells	138
Figure 6.17 Live/Dead images of HePG-2 cells incubated with control (blank) for 24 hours (a) live cell and (b) dead cells.....	139

Figure 6.18 Live/Dead images of HePG-2 cells incubated with free PTX for 24 hours (a) live cell and (b) dead cells	139
Figure 6.19 Live/Dead images of HePG-2 cells incubated with PTX-SF/PPP nanoparticles for 24 hours (a) live cell and (b) dead cells	139
Figure 7.1 Illustration of PTX-FA-SF/PPP nanoparticles	143
Figure 7.2 Schematic diagram of the preparation strategy for the production of PTX-FA-SF/PPP nanoparticles	143
Figure 7.3 FE-SEM photos of PTX-FA-SF/PPP nanoparticles (a) 10000 × and (b) 20000 ×	144
Figure 7.4 Particle size distribution of PTX-FA-SF/PPP nanoparticles.....	144
Figure 7.5 FTIR spectras of folic acid (FA), PTX-SF/PPP nanoparticles, and PTX-FA-SF/PPP nanoparticles	146
Figure 7.6 Calibration curve of folic acid at 365nm	147
Figure 7.7 Calibration curve of folic acid at 280nm	147
Figure 7.8 UV-Vis spectras of folic acid (FA), PTX-SF/PPP nanoparticles, pancreatin hydrolysates of PTX-SF/PPP nanoparticles and PTX-FA-SF/PPP nanoparticles	149
Figure 7.9 <i>In vitro</i> release profile of PTX from PTX-FA-SF/PPP nanoparticles in PBS buffer (pH 6.0 and 7.4)	151
Figure 7.10 Fluorescence histograms of HHF-1 cells incubated with SF/PPP nanoparticles for 0.5h, 4h and 24h	153
Figure 7.11 Fluorescence histograms of MCF-7 cells incubated with SF/PPP	

nanoparticles for 0.5h, 4h and 24h.....	153
Figure 7.12 Cellular uptake of SF/PPP nanoparticles by HFF-1 and MCF-7 cells for 0.5h, 4h and 24h.....	153
Figure 7.13 Fluorescence histograms of HFF-1 cells incubated with FA-SF/PPP nanoparticles for 0.5h, 4h and 24h.....	154
Figure 7.14 Fluorescence histograms of MCF-7 cells incubated with FA-SF/PPP nanoparticles for 0.5h, 4h and 24h.....	154
Figure 7.15 Cellular uptake of FA-SF/PPP nanoparticles by HFF-1 and MCF-7 cells for 0.5h, 4h and 24h.....	155
Figure 7.16 (a) DIC and (b) Fluorescence images of MCF-7 cells after 0.5h of incubation with SF/PPP nanoparticles.....	156
Figure 7.17(a) DIC and (b) Fluorescence images of MCF-7 cells after 0.5 h of incubation with FA-SF/PPP nanoparticles.....	156
Figure 7.18 Cell viability of MCF-7 cells incubated with nanoparticles for 1, 2, 3, 5 and 7 days.....	159
Figure 7.19 Optical images of MCF-7 cells incubated with PTX-FA-SF/PPP nanoparticles for (a) 0 day, (b) 1 day, (c) 2 days, (d) 3 days, (e) 5 days and (f) 7 days.....	160
Figure 7.20 Optical images of MCF-7 cells incubated with PTX-SF/PPP nanoparticles for (a) 0 day, (b) 1 day, (c) 2 days, (d) 3 days, (e) 5 days and (f) 7 days.....	161
Figure 7.21 Live/Dead images of MCF-7 cells incubated with 0.5 μ g/ml	

PTX-SF/PPP for 24 hours (a) live cell and (b) dead cells.....	162
Figure 7.22 Live/Dead images of MCF-7 cells incubated with 0.5 µg/ml PTX-FA-SF/PPP for 24 hours (a) live cell and (b) dead cells	162
Figure 7.23 Cell viability of HFF-1 cells incubated with nanoparticles for 1, 2, 3, 5 and 7 days.....	163
Figure 7.24 Optical images of HFF-1 cells incubated with PTX-FA-SF/PPP nanoparticles for (a) 0 day, (b) 1 day, (c) 2 days, (d) 3 days, (e) 5 days and (f) 7 days.....	164

LIST OF TABLES

Table 2.1 Biodegradable and biocompatible materials used to prepare polymer particles.....	17
Table 2.2 Supercritical fluids combine properties of liquids (high solubility, high density) and gases (low viscosity) [104].....	30
Table 2.3 Polymer nano/microparticles prepared by the SEDS process.....	43
Table 3.1 Experimental factors and levels	52
Table 3.2 Experimental design and results of full factorial design.....	54
Table 4.1 Drug load (DL) and encapsulation efficiency (EE) of PTX-SF and IDMC-SF nanoparticles before and after ethanol treatment.....	95
Table 7.1 The ratio of fluorescence intensity of nanoparticles in MCF-7 cells to that in HFF-1 cells at different incubation time (hours)	157

LIST OF ABBREVIATIONS

SF	Silk fibroin
PLLA	Poly(L-lactic acid)
PEG	Polyethylene glycol
PPP	PLLA-PEG-PLLA
SF/PPP	Silk fibroin/PLLA-PEG-PLLA
FA	Folic acid
FITC	Fluorescein Isothiocyanate
PTX	Paclitaxel
IDMC	Indomethacin
scCO ₂	Supercritical CO ₂
SEDS	Solution-enhanced dispersion by supercritical CO ₂
FFD	Full factorial design
FE-SEM	Field-emission scanning electron microscope
TEM	Transmission electron microscopy
TG	Thermogravimetry
DSC	Differential scanning calorimetry
FTIR	Fourier transform infrared spectroscopy
XRPD	Powder X-ray diffraction
UV-Vis	Ultraviolet-visible
HPLC	High-performance liquid chromatography
EtOH	Ethanol

DCM	Dichloromethane
HFIP	1,1,1,3,3,3-Hexafluoroisopropanol
DL	Drug load
EE	Encapsulation efficiency
LDH	Lactate dehydrogenase
MTS	(3-(4,5-dimethylthiazol-2-yl)-5-(3-carboxymethoxyphenyl)-2-(4-sulfophenyl)-2H-tetrazolium, inner salt)
HFF-1	<i>Human foreskin fibroblasts</i>
MCF-7	<i>Human breast adenocarcinoma cell line</i>
HePG-2	<i>Human liver hepatocellular carcinoma cell line</i>

Chapter 1 Introduction

1.1 Background

Current cytotoxic chemotherapy have many limitation, including severe toxicity, substantial removal from circulation after systemic administration, widespread distribution among all tissues, degradation by chemical and enzymatic hydrolysis, and low cellular uptake efficiency [1-2]. Large efforts are ongoing to fabricate smart polymer nanoparticle drug delivery systems to decrease adverse side effects of drug and enhance therapeutic efficiency. It may protect therapeutic agents from degradation, enhance cell entry, and make it possible for the administration of poorly water-soluble drugs [3-5].

Polymer nanoparticles based on silk fibroin (SF) are very promising because SF is a nonthrombogenic, anti-inflammatory, and highly biocompatible natural polymer. Additional properties of SF contain swelling properties that depend on solution pH, its strong affinity to polysaccharides and improving cell adhesion [6-7]. Also, the silk fibroin molecules possess many functional groups that can be modified by tumor-specific ligands such as folic acid to obtain a tumor-targeted drug delivery [8-12].

However, the difficulties in processing, high natural variability and water solubility of silk fibroin have limited its application as drug delivery matrix [12-14]. Post treatment by ethanol or methanol to induce water-insolubility of SF nanoparticles might result in drug leakage [12].

Biodegradable synthetic polymer poly-L-Lactide (PLLA) and its copolymers with polyethylene glycol (PEG) such as PLLA-PEG-PLLA (PPP) nanoparticles have obtained much attention because of desired features , including outstanding processing properties, flexible structure, stability and controlled drug release property [15,16]. Therefore synthetic polymer can overcome the disadvantage of SF nanoparticles. Especially, the use of PEG could decrease internalization of particle by the mononuclear phagocytic system and prolong circulation times of drugs *in vivo*.

However, the major challenge for these synthetic polymers is undesirable biological responses to cells and/or tissues and are not always suitable for tumor-targeted chemical modification due to lack of bioactive functions such as carboxyl or amine groups. Furthermore, their degradation products are relatively strong acids and cause inflammation [17]. Therefore, improvement of biocompatibility is also important for synthetic polymers.

Combination of natural and synthetic polymer is an effective strategy to overcome their disadvantages [18]. Therefore, it is necessary to fabricate SF/PPP composite nanoparticles, which could exhibit excellent biocompatibility and prolonged the blood circulation times of drugs as well as tumor-targeted drug delivery via conjugation with the tumor-specific ligands such as folic acid.

The conventional methods for the preparation of polymer nanoparticles involve emulsification/solvent evaporation, nanoprecipitation, salting out and spray drying methods [19]. However, the major disadvantage of these methods is

the high residual solvent content that may cause toxicity in the final products. In addition, it is difficult to control particle size of the products. Moreover, high temperatures employed in these methods such as spray drying may induce denaturation of active substances.

Recently, nanoparticle formation techniques using supercritical CO₂, have been utilized as an interesting alternative to the methods mentioned above because of the mild critical conditions (T_c=304.1K, P_c=7.38 MPa), non-toxicity, non-flammability and affordable costs [20-21]. In particular, as a modified supercritical anti-solvent (SAS) process, solution-enhanced dispersion by supercritical CO₂ (SEDS), in which supercritical CO₂ and solution are atomized by a coaxial nozzle to obtain a smaller droplet and intensify mixing to increase mass transfer rates, has been widely used to prepare nanoparticles due to the lower operational temperature and resulting particles, which are smaller in size as well as have more controlled morphology, and less or no solvent residue or impurities.

Based on the analysis above, it is clear that to develop SF-based nanoparticles drug delivery system by supercritical CO₂ technology for tumor therapy involves multidisciplinary knowledge and research in this field, which will be reviewed in Chapter 2, including nanoparticles drug delivery system for tumor therapy, SF-based polymer nanoparticles such as SF, SF/PPP and tumor targeted SF/PPP nanoparticles, nanoparticles formation technology, and supercritical fluid technology.

1.2 Project objectives

In literature review in Chapter 2, many research gaps were identified and summarized. In order to fill those gaps and achieve the goal of developing silk fibroin-based nanoparticles drug delivery system for tumor therapy, paclitaxel (PTX) was chosen as anti-tumor model drug and silk fibroin-based polymer including SF and SF/PPP were chosen as matrix materials to load PTX. The solution enhanced dispersion by supercritical CO₂ (SEDS) process will be investigated to fabricate PTX loaded SF-based nanoparticles delivery system for tumor therapy. Furthermore, functional substances such as folic acid (FA) can be used to modify the surface of SF/PPP nanoparticles to achieve tumor-targeted therapy. Therefore, this study has the following principal objectives:

- (1) To prepare silk fibroin (SF) nanoparticles via solution enhanced dispersion by supercritical CO₂ (SEDS) process, investigate effect of process parameters on particle size and study the formation mechanism;
- (2) To characterize SF nanoparticles prepared by the SEDS process and explore their application in drug delivery system;
- (3) To fabricate SF/PPP nanoparticles as novel drug carrier by the SEDS process.
- (4) To encapsulate PTX using SF/PPP nanoparticles and study the anti-tumor activity of PTX-SF/PPP nanoparticles *in vitro*;
- (5) To develop a smart folic acid grafted PTX-SF/PPP (PTX-FA-SF/PPP) nanoparticles for tumor-targeted therapy.

1.3 Project significance and originality

The significance and originality mainly include the following four points:

(1) The present study will provide a novel technique with many advantages to prepare SF nanoparticles, which can be utilized extensively in textiles, food, the specialized cosmetic industry and biomedical fields.

(2) The current research tries to incorporate natural silk fibroin (SF) into the synthetic polymer (PPP) for the first time by the SEDS process to fabricate novel SF/PPP nanoparticles, which can be used as novel biomaterial, especially drug carrier in biomedical fields.

(3) This project is anticipated to develop a smart folic acid grafted SF/PPP (FA-SF/PPP) nanoparticles drug delivery system, which has potential clinical application in tumor-targeted therapy.

(4) The present research will develop knowledge and theoretical understanding of the physical, chemical and biological characteristics of SF, SF/PPP and FA-SF/PPP nanoparticles, especially biocompatibility, controlled drug release and tumor-targeted properties.

1.4 Research methodology

To achieve the objectives of the project mentioned in this Chapter, the following research methodology was employed:

1.4.1 Nanoparticle formation technology

Solution-enhanced dispersion by supercritical CO₂ (SEDS) was used to fabricate silk fibroin (SF) nanoparticles, SF/PPP composite nanoparticles and drug loaded SF/PPP nanoparticles. The SEDS apparatus is made up of three main parts: a CO₂ supply system, an organic solution (or particle suspension) delivery system and a high pressure vessel with a volume of 1000 ml. An ‘injector’ with two containers separated by a piston was acted as the particle suspension delivery system. Using the SEDS process, when the desired experimental conditions were achieved, the organic solution containing solute was transported into the high pressure vessel via a stainless steel coaxial nozzle by an HPLC pump. The products of nanoparticles can be collected from the high pressure vessel for characterization.

For tumor-targeted modification of nanoparticles, folic acid (FA) was chosen as tumor-specific ligand to be grafted on the surface of the SF/PPP nanoparticles successfully by conjugation of the amino group on the silk fibroin with the carboxylic group of folic acid activated by N-(3-dimethylaminopropyl)-N-ethyl-carbodiimide/N-hydroxysuccinimide (EDC/NHS). After being purified, the FA-SF/PPP nanoparticles powder can be obtained by vacuum-drying overnight for the next experiment.

1.4.2 Characterization of nanoparticles

The morphologies, structures, and physical and chemical properties of the

silk fibroin-based nanoparticles, including silk fibroin nanoparticles, SF/PPP nanoparticles, folate-SF/PPP nanoparticles and drug loaded nanoparticles were characterized and analyzed with the use of advanced techniques such as field emission scanning electron microscopy (FE-SEM), transmission electron microscopy (TEM), Differential Scanning Calorimetry (DSC), Fourier Transform Infrared Spectroscopy (FTIR), Powder X-ray diffraction (XRPD), and UV-Vis Spectroscopy.

1.4.3 Drug loading and *in vitro* release properties

The content of drug was analyzed by an ultraviolet (UV) spectrophotometer or UV-Vis/HPLC measurement. Drug load is the ratio of drug to the gross weight of the drug loaded polymer nanoparticles. Encapsulation efficiency is the ratio of wt. of drug entrapped in nanoparticles to the gross weight drug used in the experiment. The *in vitro* drug release property can be showed by studying the drug release curve determined based on the cumulative release percentage of drug (% w/w) in PBS solution over long periods of time.

1.4.4 Biological evaluation of nanoparticles

The biocompatibility of SF-based nanoparticles can be evaluated by 3-(4,5-dimethylthiazol-2-yl)-5-(3-carboxymethoxyphenyl)-2-(4-sulfophenyl)-2H-tetrazolium (MTS) assay and lactate dehydrogenase (LDH) assay. *In vitro* cytotoxicity activity of drug loaded SF-based nanoparticles can be evaluated by

MTS assay and Live/Dead assay. Cellular uptake studies of nanoparticles were observed using Fluorescent Microscopy (Nikon, Eclipse 80i). Fluorescent intensity was measured using Image J and was normalized to cell number per image. Besides, Flow Cytometry analysis was also used to count the cellular uptake efficiency and confirm the specificity of cellular uptake of folic acid modified SF/PPP nanoparticles to cancer cells by performing coculture experiments with *Human foreskin fibroblasts* (HHF-1) and *Human breast adenocarcinoma cell line* (MCF-7) cell line.

1.5 Thesis outline

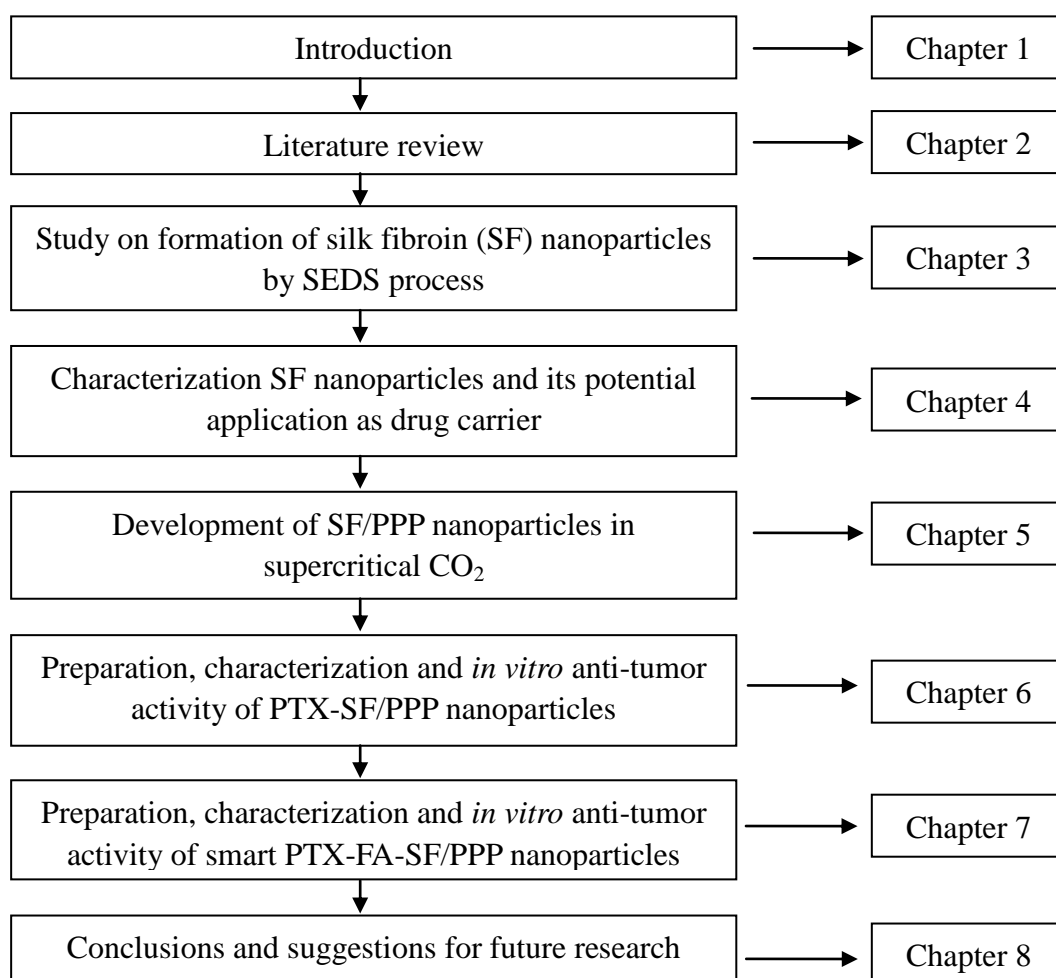


Figure 1.1 Schematic research framework and thesis outline

The thesis consists of eight Chapters as shown in Figure 1.1. Chapter 1 provides an introduction to the significance of developing a smart nanoparticle drug delivery system for anti-tumor therapy. The project objectives, significance and originality, and research methodology are presented as well.

In order to achieve the objectives, Chapter 2 reviews a broad spectrum of research in relation to silk fibroin/PLLA-PEG-PLLA (SF/PPP) nanoparticles for tumor therapy, in which limitations and knowledge gaps are identified. The next Chapters will fill these gaps.

Chapter 3 presents a method to prepare silk fibroin nanoparticles, investigate the effect of process parameters on particle size with Minitab software and study the possible particle formation mechanism.

Chapter 4 focuses on characterization of silk fibroin nanoparticles and exploring their application as drug carrier.

Chapter 5 introduces the preparation and characterization of SF/PPP nanoparticles by the SEDS process.

Chapter 6 presents the application of SF/PPP nanoparticles as a drug carrier. PTX was encapsulated by SF/PPP nanoparticles. The physical and chemical properties, controlled drug release property and *in vitro* anti-tumor activity of PTX-SF/PPP nanoparticles were investigated.

Chapter 7 is an extension of Chapter 6. It describes a smart PTX-SF/PPP folic acid grafted PTX loaded silk fibroin/PPP (PTX-FA-SF/PPP) nanoparticles for tumor-targeted therapy.

Finally, Chapter 8 provides the general conclusions and some suggestions for future work.

Chapter 2 Literature review

2.1 Nanoparticle drug delivery system for tumor therapy

2.1.1 Tumor therapy

Cancer is a leading cause of death around the world, causing approximately 7.6 million deaths (around 13% of all deaths) in 2008. Moreover, cancer deaths will continue to rise to over 11 million in 2030 [22]. It results from the uncontrolled growth and spread of abnormal cells due to inherited or environment-induced mutations. Because most human cancers (>85%) are related to solid tumors, current tumor therapy depends on the type and stage of your cancer, but it often involves chemotherapy, radiation, surgery, or a combination of these treatments to eliminate tumor cells from the human body [23]. In the absence of curative treatment modalities, cytotoxic chemotherapy is the most widely used treatment for cancer in order to improve therapeutic efficiency and prolong the life of cancer patients [24, 25].

Chemotherapy is one of the most common treatments for cancer that uses drugs to destroy cancer cells. Advances in conventional chemotherapy have led to an improvement in patient survival. However, most current anticancer agents are subjected to undesirable biodistribution, systemic toxicity and adverse side effects. They lack selectivity to reach tumor cells, not just killing cancer cells,

but also harming healthy ones [2]. For example, the commonly used anticancer drugs, including paclitaxel (PTX), doxorubicin, fluorouracil (5-Fu), cisplatin and Tamoxifen, are toxic to both tumor and normal cells. Secondly, limited systemic circulation lifetime also reduces the therapeutic efficiency [26]. Moreover, larger dosages are demanded because of the limit of bioavailability of these drugs to tumor tissue, resulting in higher toxicity to normal tissue and an increased incidence of multiple drug resistance. In addition, they may be very expensive due to limited supply [22]. Therefore, there is urgent need to develop advanced smart drug delivery system to reduce the severity of side effects during the administration of chemotherapeutic drugs and to minimize the occurrence of multidrug resistance as a cause of nonresponsive or refractory disease.

2.1.2 Nanoparticle drug delivery system

A drug delivery system (DDS) consists of drug carrier in which the active drug is dissolved, dispersed, or encapsulated, or onto which the active ingredient is adsorbed or attached [27]. Drug carrier materials play a significant role in the delivery of drug. These carriers can be processed into different drug-controlled release systems, such as nanoparticles, microspheres, microcapsules, pills, emulsions and so on.

Among them, nanoparticles have attracted much attention for their ability to be used as an effective carrier in promoting the efficacy of drugs. Nanoparticles as drug carrier were first developed around the 1970s by Birrenbach G. and

Speiser PP [28]. They were initially colloidal particulate systems with sizes ranging from 1~1000 nm, demonstrating unique characteristics because of their “size effect”. As is known, the diameter of the smallest capillaries in the human body is about 4 μm . Therefore, nanoparticles with small diameter allows for access into all sites in the human body by intravenous, intramuscular, or subcutaneous route. Besides, nanoparticle with small diameter could decrease irritant reactions at the injection site. Especially, nanoparticles can enhance therapeutic efficiency of drug by controlled drug release property and selectively deliver anticancer drugs to the tumor site by the Enhanced Permeability and Retention effect (EPR-effect).

Enhanced Permeability and Retention effect (EPR-effect)

Most nanoparticles are inclined to accumulate in tumors because of the pathophysiologic characteristics of tumor blood vessels. In general, Owing to the rapid growth of the tumor cells and insufficient nutrients and oxygen supply, the incomplete tumor vasculature leads to leaky vessels with pore size of 0.1 μm to 2 μm as compared to normal vessel junctions of 5~10 nm, depending on the tumor type [29,30]. These large pores cause high vascular permeability in tumors. Therefore, nanoparticles with small size could get into tumors [31,32]. The compound in tumors will have a retention time higher than that in normal tissues due to the lack of well-defined lymphatic system, which can clear macromolecules [33]. Therefore, the increased permeability of tumor vasculature

coupled with impaired lymphatic system result in “enhanced permeability and retention” (EPR) effect, which was first reported in 1986 by Matsumura and Maeda based on the observations that macromolecules exhibit an enhanced tumor accumulation [34, 35].

Controlled drug release

Nanoparticles can encapsulate various types of drugs and exhibit controlled drug release property. Controlled release formulation (CR) overcomes many of the drawbacks of conventional immediate release formulation (IR). Contrary to conventional IR dosage forms, CR can reduce drug plasma level fluctuations and maintain a steady drug plasma level between the minimum effective concentration and maximum safe concentration over a prolonged time period; thus the adverse side effects of drugs can be decreased as shown in Figure 2.1. So it makes controlled release especially suitable for the drugs that have plasma peak levels associated with side effects and the drugs with a short terminal half-life of elimination. Secondly, controlled release formulation can protect drugs, especially proteins, from being destroyed by human body. Moreover, the reduced side effects and lower frequency of administration of CR also increase patient comfort and compliance, especially in patients who are subject to a chronic disease. Besides, it also reduces healthcare costs because of lower dosages and reduction of side effects [36, 37].

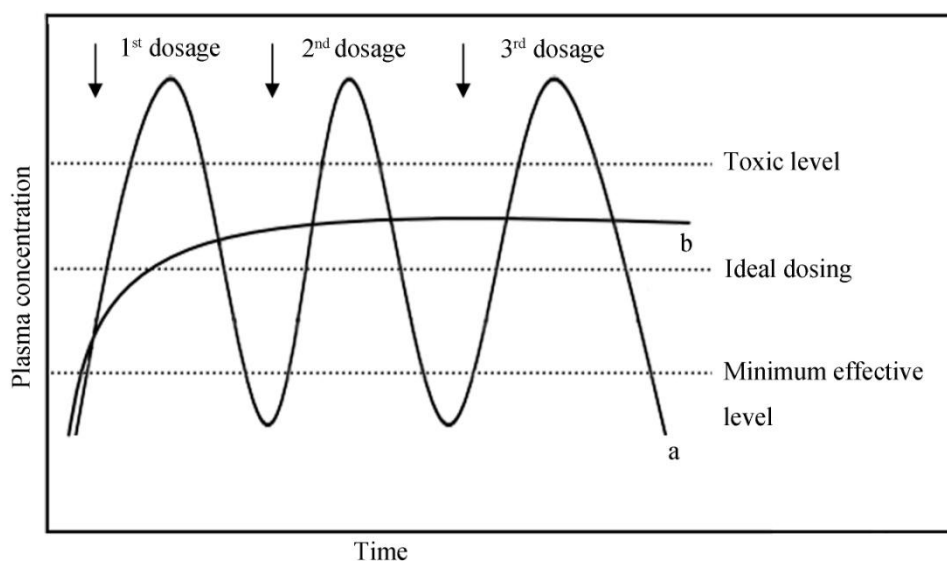


Figure 2.1 Plasma drug concentration profiles for (a) conventional immediate release formulation (IR) and (b) controlled release formulation (CR)

Besides, nanoparticles provide the feasibility of variable routes of drug administration, including injection, transdermal absorption, oral application and inhalation. In some cases, by conjugation with tumor-specific ligands, it can even provide tumor-targeted drug delivery and is very suitable for tumor therapy [38, 39].

In terms of these advantages above, nanoparticle drug delivery systems have attracted much attention and are being applied to overcome several shortcomings of conventional drug delivery systems such as non-selective distribution in the body, low bioavailability, poor solubility in water, and low therapeutic indices [40]. Figure 2.2 shows the advantages of nanoparticles drug delivery system in the treatment of cancer. Therefore, it is very necessary to develop nanoparticle drug delivery systems for tumor therapy.

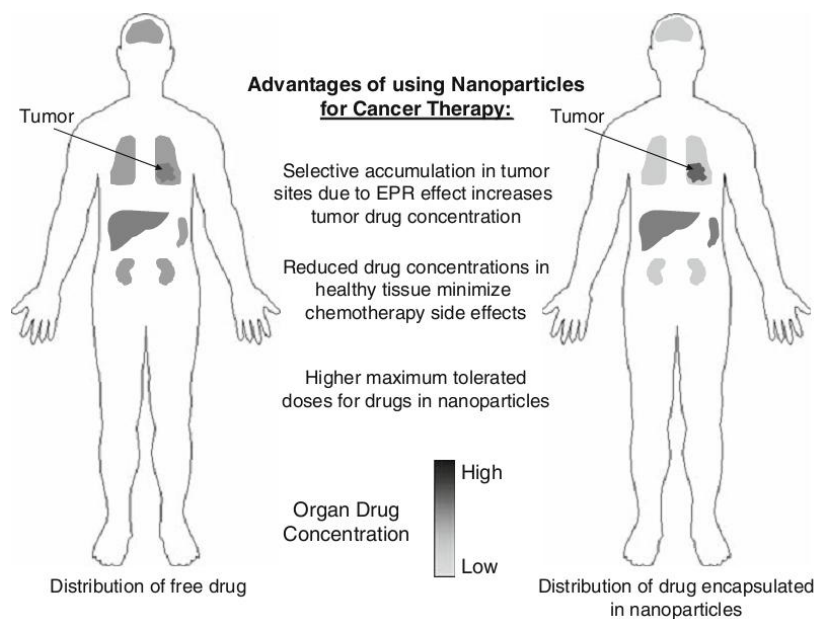


Figure 2.2 Advantages of using nanoparticles drug delivery system for cancer therapy compared to free drug [41]

2.2 Polymer nanoparticles

Over the past few decades, many effective nanoparticles drug delivery systems have been developed. These nanoparticles generally can be prepared using various kinds of materials including liposomes [42-44], metal [45-47], and polymers (polymer nanoparticles, micelles, or dendrimers) [48, 49]. Especially, polymer nanoparticles drug delivery systems have attracted much attention because of their ability to preferentially deliver drugs to cancer cells. They were reported by Kataoka's group in the 1990s through the development of doxorubicin-conjugated PLGA-PEG block copolymer micelles [50].

Polymers used in controlled drug delivery may be classified as either (i) biodegradable and biostable, or (ii) natural and synthetic [51]. Suitable polymer

should not only be biodegradable in response to biological condition but also exhibit excellent biocompatibility in human body. Besides, a polymer applied in biomedical fields should be unchanged during storage, easily processable, and sterilizable [52].

Table 2.1 Biodegradable and biocompatible materials used to prepare polymer particles

	Classification	Polymer
Natural	Polysaccharides	Cellulose, alginate, dextran, starch, chitin /chitosan, and hyaluronic acid derivatives
	Proteins	(e.g., soy, collagen, fibrin, gelatin, albumin)
Synthetic	Polyesters	Poly(lactic acid), poly(glycolic acid), Poly(hydroxyl butyrate), Poly(ϵ -caprolactone), Poly(-malic acid), poly(dioxanones) Polyesters
	Polyanhydrides	Poly(sebacic acid), poly(adipic acid), poly(terphthalic acid) and various copolymers
	Polyamides	Poly(imino carbonates), polyamino acids
	Phosphorous-based polymers	Polyphosphates, polyphosphonates, polyphosphazenes
	Others	Poly(cyano acrylates), polyurethanes, poly-orthoesters, polydihydropyrans, polyacetals

Table 2.1 shows the biodegradable and biocompatible materials used to prepare polymer nanoparticles. Among the available potential biodegradable and biocompatible polymer, protein-based nanoparticles play an important role. Proteins are macromolecules composed of amino acids that have been widely used in biomedical fields due to their unique functionalities. Proteins-based natural polymer materials include collagen, fibrin, gelatin, albumin, *etc.* They are biodegradable, non-antigenic, and possess excellent biocompatibility. Besides, proteins exhibit various functional groups and can trigger a biological response to cells. Especially, the surface of protein nanoparticles can be modified by covalent attachment of drugs and ligands to enhance therapeutic efficiency [53].

Nowadays research is focused on the fabrication of nanoparticles using proteins like collagen, fibrin, gelatin and albumin [53-56]. Recently, a nanoparticle formulation of albumin-bound paclitaxel has been applied in clinics for the treatment of metastatic breast cancer [57]. However, study of using natural nanoparticle drug carriers for tumor therapy is still lacking. Silk fibroin (SF)-based nanoparticles, one kinds of protein nanoparticles delivery system that could solve limitations of synthetic degradable polymer nanoparticles, has attracted much attention.

2.2.1 Silk fibroin (SF) nanoparticles

Silk fibroin (SF), obtained from *Bombyx mori* is a natural fibrous protein composed of 5507 amino acid repeats consisting of repeated motifs

(Gly-Ala-Gly-Ala-Gly-Ser)_n. The biomacromolecule is a heterodimeric protein with a heavy chain (395 kDa) and a light chain (25 kDa) connected by a single disulfide bond. And a glycoprotein, P25 associated with disulfide-linked heavy and light chains by noncovalent interaction [58]. It exhibits little or no immunological reaction and retains many of the desirable features of silk materials [59]. Due to its excellent features of biocompatibility, long-term degradability and improving cell adhesion and proliferation [7], SF can be applied to biomaterials such as the matrix for enzyme immobilization [60], mammalian cell culture [61, 62], drug delivery system [63, 64], artificial skin [65].

Silk fibroin microparticles have been shown to have desired physical and chemical features for controlled drug delivery, including excellent biocompatibility, mechanical stability, excellent drug loading and release properties, mild operating conditions and slow biodegradability [66]. However, the study using silk fibroin nanoparticles as drug delivery system is still lacking.

Yan *et al.* synthesized insulin-silk fibroin nanoparticles derivatives through coupling silk fibroin nanoparticles with insulin molecules successfully [67]. The results suggested that compared to the half-life of native insulin in human serum *in vitro*, the half-life of the insulin in insulin-silk fibroin nanoparticles increased by about 1.5 times. In conclusion, the silk fibroin nanoparticles can be used as protein nanoparticles drug delivery system in the field of biomedical application.

Recently, silk fibroin (SF) nanoparticles have been utilized to load anti-cancer drug paclitaxel (PTX). Chen *et al.* prepared PTX-loaded SF nanoparticles in a range of 270~520 nm successfully [68]. The SF concentration and original paclitaxel-loading volume affect drug load, encapsulation efficiency, and *in vitro* released property of paclitaxel-loaded SF nanoparticles obviously. PTX can be released in a stable way over 9 days and the maximal drug load is about 6.9%. However, when the drug load was decreased to about 3.0%, the release time of PTX-loaded SF nanoparticles can reach 2 weeks.

In a word, owing to excellent biocompatibility, controlled drug release property, it is necessary to developing silk fibroin nanoparticles as drug delivery system used in biomedical field. Moreover, the abundant functional groups of silk fibroin offer sites for chemical modification such as fluorescent attachment and tumor-specific ligands conjugation to provide fluorescent guidance and the tumor targeted drug delivery.

2.2.2 Silk fibroin /PLLA-PEG-PLLA (SF/PPP) nanoparticles

However, the difficulties in processing, high natural variability and water solubility of silk fibroin have limited its application as drug delivery matrix. Especially, post treatment by ethanol and methanol to induce water-insolubility of SF nanoparticles might result in drug leakage.

Synthetic biodegradable polymers with precise chemical composition can

overcome the disadvantages of silk fibrion above and are more easily designed for specific application, such as controlled rates of dissolution, permeability, degradation, and erosion [69]. Therefore, it has been commonly used as drug carrier in biomedical fields. U.S. Food and Drug Administration (FDA)-approved polymers, such as homopolymers of poly(L-lactide) (PLLA) or poly(glycolide) (PGA) and their copolymers poly(lactic-co-glycolic acid) (PLGA), are commonly applied in biomedical devices.

Nowadays, increasing attention is focused on the preparation of block copolymers such as di-block poly(L-lactide)-poly(ethylene glycol) (PLLA-PEG) and tri-block poly(L-lactide)-poly(ethylene glycol)-poly(L-lactide) (PLLA-PEG-PLLA) nanoparticles as drug carriers due to their biocompatibility and excellent drug encapsulation and sustained release property [70, 71]. Polyethylene glycol (PEG) is also FDA-approved polymer. The use of polyethylene glycol (PEG) in the copolymers can inhibit the adhesion of opsonins, thus decrease internalization of nanoparticles by the mononuclear phagocytic system. Besides, the opsonization-inhibiting property of PEG clearly extends *in vivo* circulation times of entrapped drug [72, 73]. Therefore, PEGylation of particles together with the enhanced permeability and retention (EPR) effect of particle with small diameter has been shown to result in an enhanced accumulation of entrapped drugs in the tumor tissue of animal model or cancer patients with increased vascular permeability and impaired lymphatic drainage. Besides, the high hydrophilic nature of PEG enhances

the solubility and bioavailability of water-insoluble drugs.

Therefore, amphiphilic block copolymer nanoparticles can enhance drug bioavailability and reduce the severe side effects and is very suitable for tumor therapy. Further study about developing amphiphilic block copolymers such as PLLA-PEG-PLLA (PPP) nanoparticles drug delivery system to treat tumor is very necessary. However, they also have several obvious weaknesses, such as acidic degradation products which are released continuously *in vivo* and invoke a chronic immune response [74, 75] and undesirable biological response in cells or host tissues due to their strong hydrophobicity, high crystallinity and absence of bioactive groups.

In summary, the combination of a synthetic polymer with natural polymer especially silk fibroin can overcome their disadvantages and thus has attracted much attention. Therefore, there is a strong need to develop silk fibroin/PLLA-PEG-PLLA (SF/PPP) composite nanoparticles. It is an effective strategy to fabricate novel biomaterial with the desired physical and chemical properties, mechanical strength, and biological responses. Most importantly, silk fibroin has many bioactive groups, which can provide sites for conjugating with tumor-specific ligands to achieve tumor-targeted drug delivery.

2.2.3 Tumor targeted SF/PPP nanoparticles

In order to treat tumor effectively, anticancer drugs should be delivered into the desired tumor tissues through many obstacles in the body with minimal

loss of their therapeutic efficiency in the blood circulation. Once arriving in the area of tumor tissue, the anticancer drug can selectively kill targeted tumor cells without impairing normal cells by passive and active targeting [41].

The enhanced permeability and retention (EPR) effect is the most commonly used passive strategy to selectively deliver an effective therapeutic agent to tumor area. Another passive targeting approach is the unique microenvironment surrounding tumor. Average extracellular pH value in tumors is between 6.0 and 7.0. However, the extracellular pH value in normal tissues is about 7.4. Moreover, healthy tissues and tumors have a similar intracellular pH value [5, 7, 76]. pH responsive polymers were designed to stabilize biomedical devices under normal physiological pH condition and release therapeutic agent in the unique tumor microenvironment [77,78].

Nevertheless, passive targeting also suffers from several drawbacks. Firstly, the enhanced permeability and retention (EPR) effect is not very effective in all tumors because the level of tumor vascularization and angiogenesis depends on the tumor types and anatomical sites. Besides, the high interstitial fluid pressure in the centre of tumors could hinder effective drug delivery to tumor cells [5]. Thirdly, PEGylated surfaces of polymer such as PLLA-PEG-PLLA can not only prevent clearance by the mononuclear phagocyte system, but also decrease interactions between drug carrier and cell surfaces. The difficulty in targeted delivery of anti-cancer drugs may result in drug expulsion and induction of multiple drug resistance (MDR), which inevitably impairs and decreases

therapeutic effects [30].

To overcome these disadvantages associated with passive targeting, another type of drug delivery strategy called “active targeting” has been developed. Active targeting is also called ligand based targeting. Commonly used targeting ligands contain folic acid, monoclonal antibodies, peptides, aptamers, transferrin, and hyaluronic acid [15]. Folic acid (FA) is a commonly used tumor-specific ligand for targeted delivery of anti-cancer drug in that it is inexpensive, nonimmunogenic, nontoxic, easy to be conjugated to a carrier via its γ -carboxyl group, maintain high binding affinity toward its receptor, and are environmentally stable [79-81]. In addition, recycling of folate receptors in target cells can lead to the transport of more FA conjugates. The folate receptor, a 38kDa glycoprotein, exhibits limited expression on healthy cells but are often present in large numbers on human epithelial cancer cells [82, 83]. So far, many studies about tumor-targeted drug delivery have been reported by direct conjugation of folate to drug carriers such as polymeric micelles [84], macromolecules [85], nanoparticles [86], and liposomes [87].

Although there has been much progress using targeted nanoparticle drug delivery systems to enhance the efficacy of separately administered chemotherapeutics and gene/protein therapy, clinical application of targeted cancer drugs is still lacking. Therefore, tumor targeted silk fibroin/PLLA-PEG-PLLA nanoparticles that combine PEG modification and folate-mediated drug delivery remain to be developed.

2.3 Nanoparticle preparation technology

Nanoparticles can be directly fabricated either by polymerization of monomers using classical polymerization-based methods or from preformed polymers. They exhibit many disadvantages such as inadequate biodegradability of the product and the presence of toxic residues. To avoid these problems and obtain particle systems with excellent biocompatibility, many methods have been developed based on utilizing biomacromolecules or preformed synthetic polymers [88].

For PLLA and PEG copolymer, methods utilized for formulating polymeric nanoparticles from preformed polymers mainly include emulsification/solvent evaporation, nanoprecipitation, salting out, spray drying methods and supercritical fluid technology. Many scientists have also studied the preparation of silk fibroin particles. The methods used to produce silk fibroin particles contain emulsification, salting out, spray drying mainly [89-91]. Besides, some novel techniques such as laminar jet breakup [12], lipid templating [92], two-phase microfluidic flow-focusing device [93] have been developed. Here, the most commonly used methods to fabricate polymer nanoparticles will be introduced as follows:

2.3.1 Emulsification/solvent evaporation

Emulsification-solvent evaporation is the most widely used method for the production of polymer nanoparticles due to its simple procedure and broad drug

applicability [94]. In this method, the drug is dissolved or dispersed into a polymer solution in an organic solvent such as dichloromethane, chloroform or ethyl acetate. Then the mixture is emulsified into an aqueous solution to make an oil/water (O/W) emulsion by using a surfactant such as poly(vinyl alcohol) (PVA), poloxamer-188, etc. Afterwards, solidified nanoparticles can be obtained by evaporating organic solvent [95]. The double emulsion solvent evaporation method (W/O/W) is a modified emulsification-solvent evaporation technique and can be employed to entrap small hydrophilic drugs and proteins. An aqueous drug solution is emulsified into an organic polymer solution. In these two kinds of methods, high-speed homogenization or sonication usually was employed to form emulsion [57].

2.3.2 Salting out

Bindschaedler *et al.* first reported a modified emulsion technique, which involved a salting-out process and could avoid using surfactants and chlorinated solvents [96, 97]. In the salting-out technique, polymer are initially dissolved in a water-miscible solvent (acetone, ethanol and N –methyl-2-pyrrolidone) together with drug. Then the solvent is emulsified into an aqueous gel containing the salting-out agent and a colloidal stabilizer to form an oil/water emulsion. Then sufficient amount of aqueous solution is added into the emulsion to improve the diffusion of acetone into the aqueous phase followed by the precipitation of polymer nanoparticles. Finally, using cross-flow filtration, the solvent and the

salting-out agent can be removed [98].

2.3.3 Nanoprecipitation (or solvent displacement method)

The application of emulsification techniques is greatly limited by disadvantages such as working with toxic solvents (dichloromethane, chloroform) and the requirement of high energy apparatus (ultrasound probe or homogenizer). In contrast, nanoprecipitation does not involve the input of external energy and needs less toxic organic solvents.

The nanoprecipitation method (also known as solvent displacement method) was disclosed by Fessi *et al.* for the production of polymer nanoparticles [99]. An organic solvent (acetone, methanol and ethanol) that is completely miscible with the aqueous solution was used in this process. Then organic solution of the hydrophobic polymer and drug is added dropwise into an aqueous solution containing stabilizer under stirring. Interfacial tension between the aqueous phases and organic phase will be reduced by rapid solvent diffusion into the aqueous phase. Then the formation of polymer nanoparticles will be induced. Finally, the solvent will be eliminated under vacuum [100].

2.3.4 Spray drying

In the emulsion methods, the process parameters need be controlled precisely to get desirable encapsulation efficiency. It is also difficult to remove large amounts of the organic solvent from polymer nanoparticles. Therefore,

large-scale production has been limited. Spray drying is one of the most commonly used industrial process. It has fast drying speed, few process parameters and is very suited for continuous production [94]. In this process, polymer and drug are dissolved in an organic solvent and sprayed through a fine nozzle. Spherical particles form with the immediate evaporation of the solvent. The major drawback of spray drying technique is the adhesion of the product to the inner walls of the spray-dryer. High temperatures are generally employed in this process, which can create problems, particularly in the encapsulation of peptides, and proteins that are easily denatured. Spray drying produces particles that are inclined to be in the micrometer size range and hence will not be considered further here. The spray drying technique is very suitable for processing thermo-labile materials due to absence of mechanical high energy input in this process.

In a word, emulsion solvent extraction/evaporation does not require high temperatures. The particle size of resulting particles can be controlled in a range from the nano-scale to the macro-scale. However, experimental conditions need be selected carefully to achieve products with desirable particle size and low residual solvents. The disadvantages of salting out are that only lipophilic drugs can be performed. Besides, it involves the extensive nanoparticles washing steps. Nanoprecipitation is limited to hydrophobic drugs highly soluble in organic solvents, but slightly soluble in water. All these three methods are difficult to eliminate residual solvent and may cause toxic problem. Spray drying is

expensive to operate due to high equipment and energy costs. Besides, spray drying requires high temperatures and can produce the particle with big size [101].

Therefore, there is a strong need to develop environmentally friendly cleaning methods in mild operating conditions to produce polymer nanoparticles of high purity without residual solvents. Recently, very attractive new supercritical fluid (SCF) technologies have been established as useful alternatives to conventional methods for preparation of particle, avoiding the disadvantages of the conventional techniques. These techniques have the same basic approach as conventional preparation methods: the formation of droplets and precipitation of polymer and drug after the solvent is evaporated [102].

2.4 Supercritical fluid technology

Supercritical fluids (SCFs) are substances at temperature and pressure conditions above their respective critical values (P_c ; T_c). Figure 2.3 shows the Schematic representation of a pure fluid in the P-T phase diagram [103]. The densities of the SCFs are very close to those of liquids. However, the solubility of solids in SCFs can be 3~10 orders of magnitude higher than in those of liquids. Besides, a small change about temperature and pressure will cause a significant changes about viscosity and diffusivity of the SCFs. Table 2.2 shows that SCFs combine properties of liquids (high solubility, high density) and gases (low viscosity) [104]. In another word, the SCFs can diffuse into solid materials more

effectively than liquid solution. Therefore, it could enhance mass transfer, leading to faster extraction [105]. Hence, SCFs have unique thermo-physical properties and can penetrate substances like a gas and dissolve substances like a liquid.

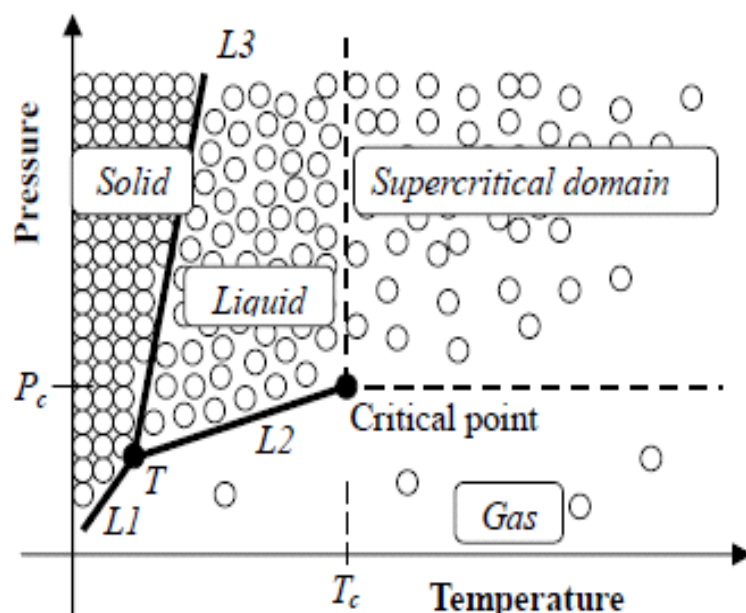


Figure 2.3 Schematic representation of a pure fluid in the P-T phase diagram [103]

Table 2.2 Supercritical fluids combine properties of liquids (high solubility, high density) and gases (low viscosity) [104]

Fluid state	Density, g/cm ³	Viscosity, g/(cm s)	Diffusion coefficient, cm ² /s
Gas	$(0.6-2) \times 10^{-3}$	$(1-3) \times 10^{-4}$	0.1-0.4
SCF	0.2-0.9	$(1-3) \times 10^{-4}$	$(2-7) \times 10^{-4}$
Liquid	0.6-1.6	$(1-3) \times 10^{-2}$	$(0.2-2) \times 10^{-5}$

Among all the possible SCFs, supercritical CO₂ (scCO₂) is the most widely used and has been shown to have great potential in the field of micronization of materials because of its favorable critical conditions ($T_c = 31.1 \text{ }^\circ\text{C}$, $P_c = 7.38 \text{ MPa}$), non-toxicity, non-flammability, and low costs [109, 110] from the

viewpoint of pharmaceutical, nutraceutical and food applications. The first industrial applications of SCFs in the early 1980s is Supercritical Fluid Extraction, which took the advantages of supercritical CO₂ and utilized it as the solvent to extract high value compounds from solid and liquid materials. Besides, the operating conditions of low temperature and pressure make SCFs attractive for pharmaceutical research.

Supercritical CO₂ technology used for the preparation of nanoparticles with controlled particle size and distribution is attracting widespread attention and has exhibited a great perspective application in electronics, ceramics, materials, pharmaceuticals, etc [108]. So far, the most common techniques for particle formation using scCO₂ include the rapid expansion of supercritical solutions (RESS), particles from gas-saturated solutions or suspensions (PGSS), and Gas or Supercritical Fluid AntiSolvent (GAS or SAS) [109-111]. In particular, solution-enhanced dispersion by supercritical fluids (SEDS), a modified SAS process, has been widely used to prepare micro or nanoparticles.

2.4.1 Rapid expansion of supercritical solutions (RESS)

The principle of particle formation in the RESS process is schematically shown in Figure 2.4. In the RESS process, the substance to be precipitated is first dissolved in a supercritical fluid. Then the resulting solution will be delivered into a low-pressure vessel via a heated nozzle. The depressurization will induce rapid precipitation of particles, which can be collected from the gaseous stream

and are free of a residual solvent. The physical morphology of the resulting particle products can be affected by the physical and chemical properties of the material and on the process parameters such as temperature, pressure, flow rate of solution, concentration of solution, *etc* [112]. The generation of particles with small size can be obtained by a rapaid release of the solute in the gaseous phase. In the RESS process, the high supersaturation ratios and a fast propagation of pressure perturbation are two kinds of distinctive features [113].

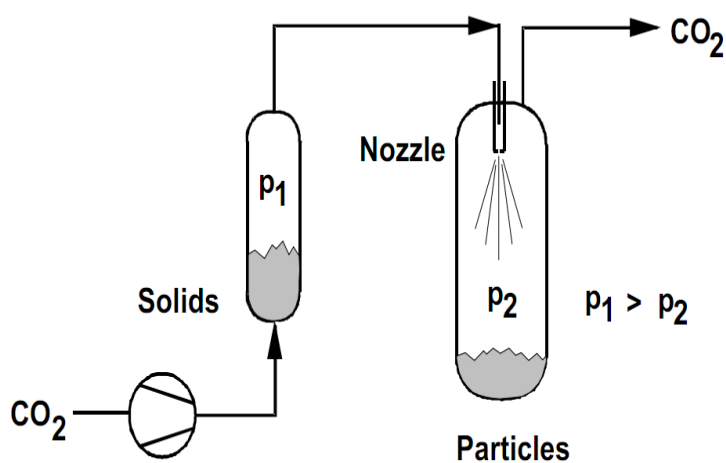


Figure 2.4 Schematic illustration of the RESS technique [114]

As is known, the RESS process is an effective method to fabricate polymer nanoparticles drug delivery systems. However, the limitation of this technique is that most of FDA approved polymers and therapeutic agents have low solubility in scCO₂. Therefore, co-solvents that can dissolve solute and scCO₂ have been used to improve the solubility of solute in scCO₂ and avoid the disadvantage of the RESS process [108]. In general, the scCO₂ has no polarity. Moreover, many materials including FDA approved polymers and therapeutic agents are polar or high molecular weight compounds. Therefore, it is very difficult to dissolve these

materials in the scCO_2 . Gas-saturated solutions or suspensions (PGSS) and Gas or Supercritical fluid anti-solvent (GAS or SAS) can be used as an alternative to solve this problem.

2.4.2 Gas-saturated solutions or suspensions (PGSS)

In the PGSS process, the materials that cannot be dissolved in supercritical fluid can be precipitated. However, the limitation of this process is that the products can absorb much gas, leading to materials swelling or a decrease in the melting point (This effects is important for spraying temperature sensitive substances) [115]. At the same time, the viscosity of the materials to be powdered is considerable decreased [116]. As solubility of gases in materials is much higher than that of materials in the gas phase, the process involves the dissolution of supercritical fluid such as scCO_2 in melted or liquid-suspended substances, resulting in the dominated gas-saturated solution or suspension [117]. When depressurizing the solution or suspension via an adequate nozzle rapidly, due to its high vapor pressure, the solution or suspension will be cooled. At the same time high supersaturation occurs and fine particles are formed. This process has been shown to be very useful for the encapsulation of therapeutic agents into polymer nanoparticles [118].

A schematic illustration of the PGSS techniques is displayed in Figure 2.5. The expansion of the gas-saturated solution results in a rapid increase in degree of supersaturation as well as the RESS process. The morphology, physical and

chemical properties of particles depends on the process parameters, including precipitation temperature, precipitation pressure, concentration of solution, flow rate of solution and composition of the solute [107].

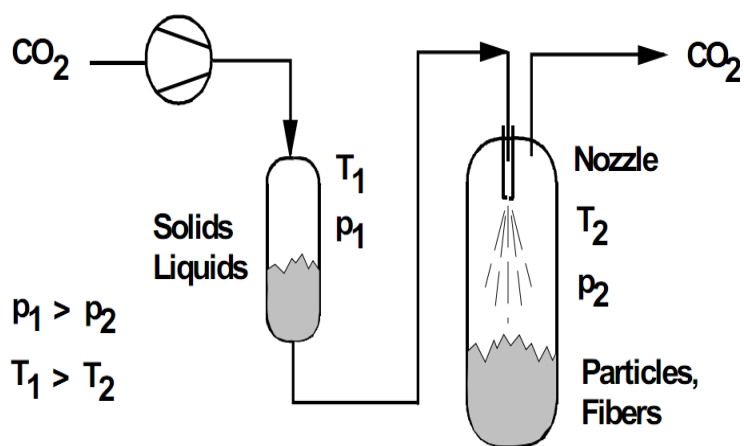


Figure 2.5 Schematic illustration of the PGSS technique [114]

Contrary to the RESS process, the material has to be melted before the spraying process starts. Based on the fact, that the PGSS process sprays the substance from the liquid phase and the RESS process from the supercritical state, the solvent consumption is much lower with the PGSS process. Therefore the advantage of the PGSS process is low pressure and lack of solvents in the whole process compared to that of the RESS process, and the lower consumption of gas due to the lower ratios of gas/liquid than in the RESS process. However, a major difficulty in the PGSS process is to prepare drug loaded polymer particles from a highly viscous liquefied polymer and with a rapid polymer solidification rate on depressurization. In addition, residual CO₂ may result in agglomeration of the resulting particles [116].

2.4.3 Anti-solvent precipitation

In general, the use of scCO₂ in the RESS or PGSS process as an environmentally friendly alternative solvent is limited to the large-scale preparation of micronized particles due to its relatively low solubility for most polymers and therapeutic agents. The anti-solvent precipitation was developed to solve this disadvantage. In this process, dense gas such as CO₂ is utilized as anti-solvent or non-solvent, which can be absorbed by an organic solvent. Then liquid phase is expanded, reducing the solvent power and inducing the precipitation of the solute. The anti-solvent precipitation can be classified in many categories, including gas anti-solvent process (GAS), supercritical antisolvent process (SAS), aerosol solvent extraction systems (ASES) and solution enhanced dispersion by supercritical CO₂ (SEDS) processes.

Gas anti-solvent process (GAS)

Figure 2.6 displays a schematic illustration of the batch GAS techniques. In the GAS process, the gas is delivered into the solution in a closed vessel and the super-saturation of the solution occurs with the increase of the concentration of the gas in the solution. Meanwhile nucleation and growth will result in the formation of particles of the solute. Finally, the residual solvent of the resulting particles can be removed by the anti-solvent. In this process, the gas acted as antisolvent doesn't need be kept at supercritical condition [107]. The principle of the GAS process is based on a sharp decrease in the solvent power of the organic

phase induced by adding a second fluid as anti-solvent [112]. The initial study was explored by Gallagher *et al.* [119].

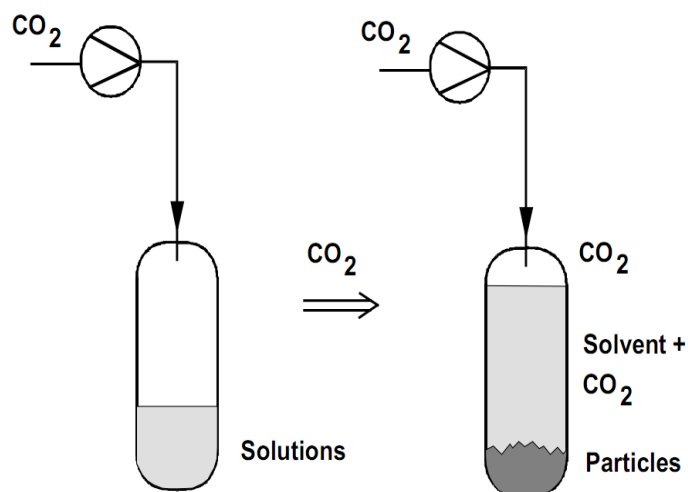


Figure 2.6 Schematic illustration of the batch GAS technique [103]

However, the main drawbacks of this method contain high residual solvents and poor control over the surface morphology and particle size distribution because of a batch discontinuous process.

In the batch GAS operation, an additional processing step is needed to obtain a dry product because the liquid phase can not be completely eliminated. In order to overcome this disadvantage, many continuous GAS techniques have been developed, such as aerosol solvent extraction systems (ASES) and supercritical antisolvent (SAS) process. In these processes, a liquid solution and a supercritical fluid are delivered continuously to a precipitator.

Aerosol solvent extraction system (ASES)

Supercritical CO₂ has been commonly used for the extraction and purification of organic substances in the food and pharmaceutical industries.

Figure 2.7 shows that in the ASES process, CO₂ is first delivered into a high pressure vessel until the system conditions reach the required level. Then the organic solvent dissolving active substances is pumped via a nozzle into the high pressure vessel containing scCO₂ and precipitation occurs by rapid extraction of organic solvent with scCO₂ and followed by a washing process to remove the organic solvent with a constant CO₂ stream. After washing, the vessel was depressurized and the resulting particles are collected as products. This technique possesses many advantages including mild operational condition and resulting particles free of solvent residues or impurities. Therefore, the ASES process has been widely used in the field of particle engineering [120].

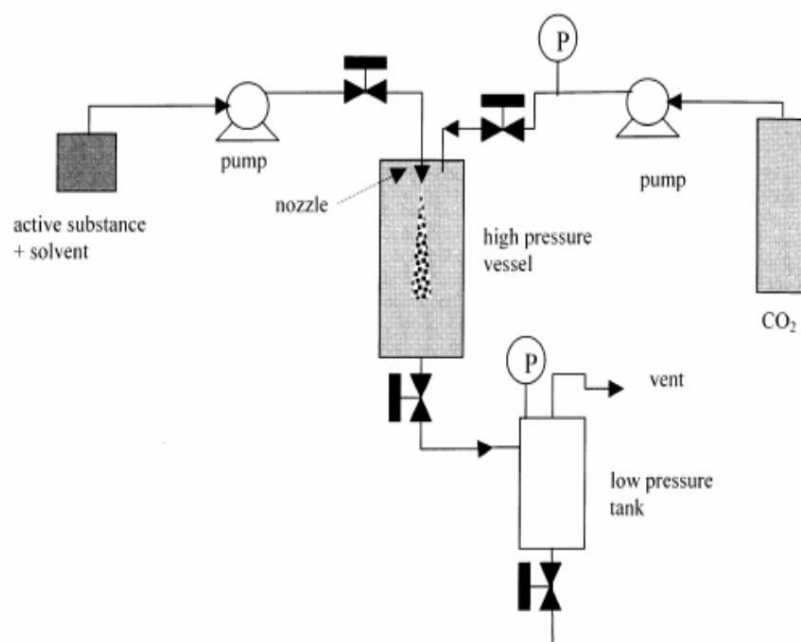


Figure 2.7 Schematic illustration of the ASES techniques [121]

Supercritical Anti-solvent (SAS) process

The traditional liquid antisolvent process produces micro/nanoparticles by

the addition of an antisolvent into a liquid solution containing desirable solutes. The antisolvent should be a liquid miscible with the primary solvent. This process has limitations in controlling particle size and particle size distribution of the products and eliminating organic solvent residues [121]. Recently, the SAS process has been developed to overcome the disadvantages of the traditional liquid antisolvent precipitation. The schematic diagram of the SAS process apparatus is illustrated in Figure 2.8. In the SAS process, an organic solution containing solute is sprayed via a nozzle to a high pressure vessel with $scCO_2$, resulting in completely mixture of the organic solution and the $scCO_2$. Continued feeding of $scCO_2$ induces supersaturation of solute such as polymer and active substances. Finally, particles can be precipitated in the vessel [122]. The SAS process has been widely used in the field of particle engineering.

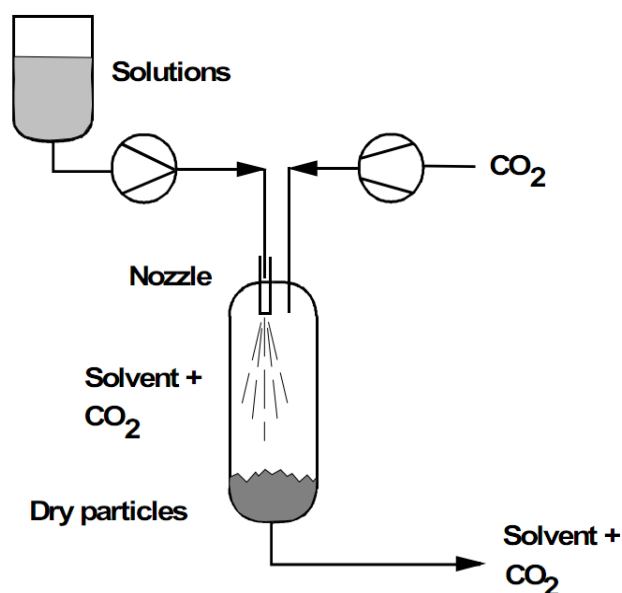


Figure 2.8 Schematic illustration of a typical continuous SAS process [105]

Solution enhanced dispersion by supercritical CO₂, SEDS

Solution enhanced dispersion by supercritical CO₂ (SEDS) process is a modified SAS process. In this process, the solution containing solute and supercritical CO₂ (scCO₂) are atomized via a specially designed coaxial nozzle to obtain droplets with small size and enhance mixing to increase mass transfer rates. This process was originally named by Hanna and York [123]. The schematic illustration of the SEDS technique and coaxial nozzle is shown in Figure 2.9. In this process, a nozzle with two coaxial passages allows the introduction of scCO₂ and a solution into the high pressure vessel where pressure and temperature are controlled [124]. When the solution contacts the scCO₂, the high velocity of the scCO₂ breaks up the solution into very small droplets and enhances mass transfer and mutual diffusion between SCFs and the droplets instantaneously, resulting in phase separation and supersaturation of the polymer solution, thus leading to nucleation and precipitation of the polymer particle [125]. In the SEDS process, the supercritical CO₂ (scCO₂) is acted as anti-solvent. In addition, scCO₂ is used as a ‘dispersing agent’ to improve mass transfer between SCFs and the droplets. Therefore, very small particles can be produced. Besides, the particle size distribution and morphology of the polymer can be controlled by adjusting the parameters of the SEDS process, including the concentration of solute, flow rate of solution, temperature, and pressure of supercritical CO₂.

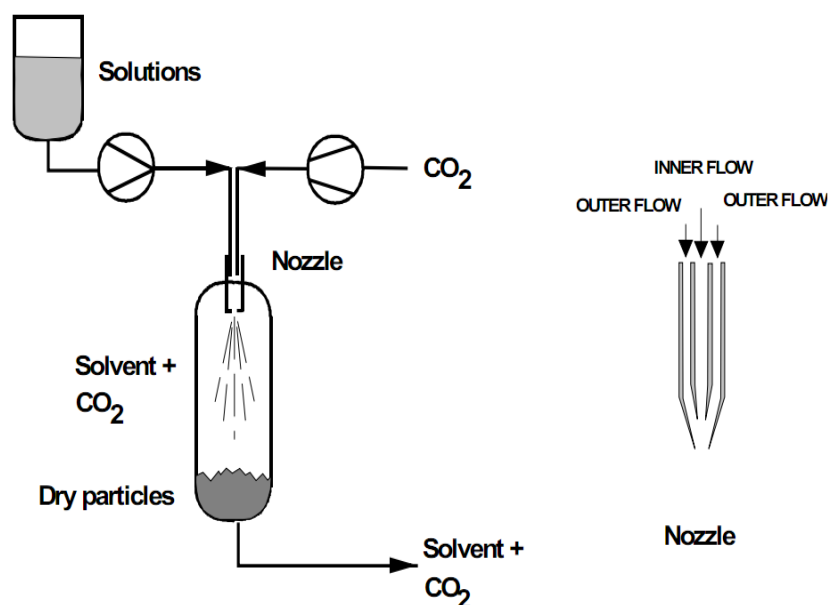


Figure 2.9 Schematic illustration of the SEDS process and co-axial nozzle [114]

In the SEDS process, a SCF such as scCO_2 plays the role of an antisolvent. Besides, it can act as a dispersant via a specially designed coaxial nozzle to enhance the mass transfer between the scCO_2 and solution. Thirdly, the scCO_2 can take away the solvent from the organic solution effectively. This method has also been modified to treat water-soluble active substances through three-coaxial-passages nozzle exhibited in Figure 2.10 to introduce an organic antisolvent, scCO_2 and aqueous solution of active substance separately into high pressure vessel. In order to develop a more effective process involving aqueous solution, the SEDS process is modified through introducing homogeneous liquid antisolvent/ scCO_2 mixtures into a two-fluid nozzle together with an aqueous solution of active substance. The SEDS process can process various kinds of substances and fabricate particles with very small diameter, controlled particle size and less or no solvent residue. Therefore the SEDS process has been widely used for preparing nanoparticle [125,126].

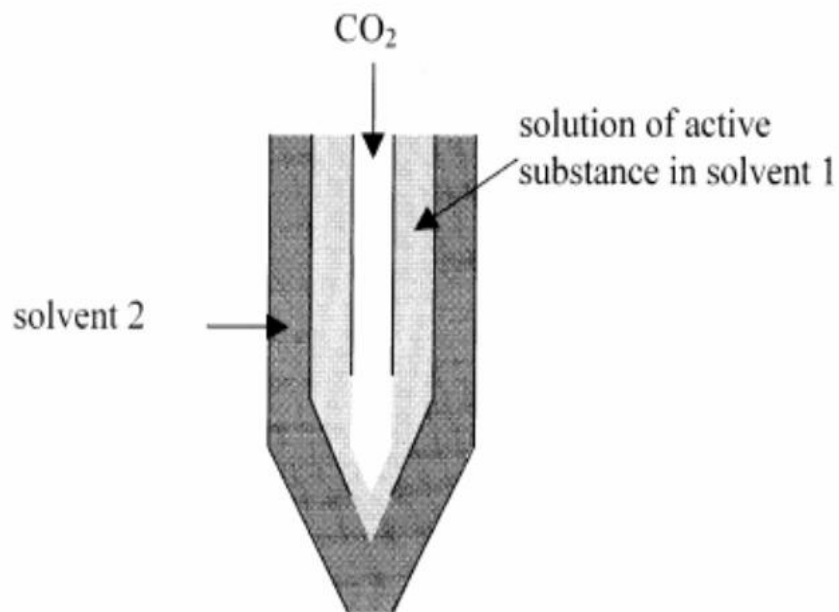


Figure 2.10 Three coaxial-passages nozzle [127]

2.5 Application of the SEDS process in formation of polymer nanoparticle drug delivery systems

In recent years, the SEDS process has been exploited to prepare the polymer nanoparticles including polymer, drug, drug loaded polymer and biofunctional composite polymer particles and so on. Table 2.3 shows polymer nano/microparticles prepared by the SEDS process.

Most studies focus on the formation of polymer particles. Chen *et al.* prepared PLLA microparticles using the SEDS process and investigated the effects of process parameters, including temperature (T), pressure (P), concentration of the solution (C), and flow rate of the solution (F). The results suggested that concentration of the solution is the most important process parameters to affect the particle size of the resulting particles, and the order of

importance of the parameters on particle size is $C > F > T > P$. PLLA microparticles with different mean size ranges between 0.64 and 6.64 μm was produced under different experimental conditions for different purposes [129]. Kang *et al.* manufactured PLLA/PLGA microparticles with mean sizes ranges between 1.76 and 2.15 μm using the SEDS process that and resulted in a decrease in the crystalline of PLLA/PLGA polymer. This method can overcome the shortcoming of low degradation of PLLA polymer caused by high crystallinity and the disadvantage of the difficulty in preparing PLGA microparticles due to low crystallinity. Moreover, the degradation of PLLA/PLGA microparticles can be controlled by adjusting the ratio of PLLA to PLGA [125].

The SEDS process was also used as a technique for drug micronization to enhance solubility and bioavailability of the poorly soluble drugs. For example, Chen *et al.* prepared puerarin fine particles and 5-Fu microparticle by the SEDS process [106, 132]. The results indicated that after micronization, the saturated concentration of 5-Fu in ethanol at 25 °C rised to 6.43 mg/mL and the solubility of puerarin fine particles in water also increased slightly. Also, adding dichloromethane into the puerarin solution can lead to a higher degree of saturation in initial solution, thus resulting in puerarin particles with small size and narrower size distribution. Moreover, the particle became more spherical in shape. And Kang *et al.* prepared the paclitaxel microparticles by the SEDS process [133]. Besides, Toropainen *et al.* also prepared

budesonide/gamma-cyclodextrin complexes by the SEDS process. The complexes improve the solubility of drug effectively [137].

Table 2.3 Polymer nano/microparticles prepared by the SEDS process

Solute	Solvent	Supercritical fluid	Particle size	Reference
PLLA	DCM	CO ₂	0.5-5µm	[128,129]
Polystyrene	Toluene	CO ₂	0.5 µm	[130]
PLLA+PLGA	DCM	CO ₂	1.76~2.15 µm	[107],[125]
Insulin	DMSO	CO ₂	1 ~ 5 µm	[131]
5-Fu	Ethanol	CO ₂	<500 nm	[106]
Puerarin fine particles	Ethanol/ DCM	CO ₂	0.19 µm	[132]
Paclitaxel microparticle	DCM	CO ₂	940 nm	[133]
Amoxicillin+PLLA	DCM	CO ₂	<1 µm	[134]
Indomethacin-loaded PLLA/PLGA microparticles	DCM	CO ₂	2.35 µm	[107]
5-Fu+ PLLA	DCM	CO ₂	0.5 µm	[106]
Hydrocortisone+DL-PLG	DCM	Supercritical N ₂ and CO ₂	<10 µm	[135]
Paclitaxel+ PLLA	DCM	CO ₂	1.64 µm	[133]
Fe ₃ O ₄ -PLLA magnetic microparticles	DCM	CO ₂	~ 803nm	[136]

Recently, the fabrication of drug loaded polymer composite particles for controlled drug delivery systems by the SEDS process has become more and more interesting. Kalogiannis *et al.* prepared amoxicillin-loaded PLLA microparticles via the SEDS process by suspending amoxicillin microparticles in PLLA solution in dichloromethane (DCM). The results indicated that the potential application of the SEDS process for the encapsulation of active substances in polymer matrixes and the microencapsulation process has higher encapsulation efficiency than the co-precipitation process [134]. Chen *et al.* encapsulated 5-Fu into PLLA microparticles [106]. Sub-micron particles with a mean size of 980 nm were fabricated with very low residual content of organic solvent. The drug load (DL) and encapsulation efficiency (EE) is 3.05% and 17.8%, respectively. No burst effect had been found and drug was released in a controlled way. The accumulative release of drug reached 89.5% in the first 36 h. Kang *et al.* fabricated PTX-PLLA microparticles by the SEDS process. The results suggested that PTX-PLLA microparticles possessed a spherical shape with small particle sizes and residual organic solvent in the resulting particles is very few. Moreover, the SEDS process has decreased the crystallinity of PTX significantly. The drug load (DL) and encapsulation efficiency (EE) of PTX-PLLA microparticles were 14.33% and 62.68%, respectively. And compared to the free PTX, the PTX-PLLA formulation showed higher anticancer activity [133]. It indicated that the SEDS process can be utilized to prepare drug loaded microparticles delivery system for tumor therapy. Whitaker *et al.*

fabricated protein-loaded poly(DL-lactic acid) microparticles via the SEDS process [138]. The results indicated that the mean size of the resulting microparticles was ranged between 10~300 μm . Ribonuclease A and lysozyme can be loaded in polymer microparticles with no obvious loss of enzymatic activity. Biological assays of insulin and calcitonin also suggested that supercritical process does not damage protein function.

Besides, Fe_3O_4 -PLLA microparticles were fabricated successfully by solution-enhanced dispersion by supercritical CO_2 (SEDS) [136]. The *in vitro* cytotoxicity assay indicated that they had no obvious cytotoxicity and possessed excellent biocompatibility. The results suggested that Fe_3O_4 -PLLA microparticles have potential application in biomedical fields.

As mentioned above, particle formation using solution-enhanced dispersion by supercritical CO_2 (SEDS) technique can be applied in biomedical fields, especially polymer nanoparticles drug delivery systems. On one hand, the bioavailability of drugs could be improved due to micronization by the SEDS process. On the other hand, the SEDS process can be used to fabricate drug loaded polymer to control drug release rate.

So far, study on generation of silk fibroin nanoparticles by supercritical CO_2 technology has not been reported. Moreover, nanoparticle formation mechanisms by the SEDS process is still not clear because the SEDS process is influenced by many factors including temperature (T), pressure (P), concentration of the solution (C), and flow rate of the solution (F). Thirdly,

studies utilizing the SEDS process to fabricate polymers, especially natural/synthetic composite polymer nanoparticles drug delivery systems are insufficient. Therefore, there is a strong need to employ supercritical CO₂ technique, especially the SEDS process to fabricate silk fibroin-based nanoparticles drug delivery system, which would be very promising in biomedical application, especially tumor therapy.

2.6 Summary of research gaps

Based on the literature review above, the knowledge gaps concerning silk fibroin-based nanoparticles drug delivery system by supercritical CO₂ technology can be identified mainly as follows:

- (1) The conventional methods of fabrication for polymer nanoparticles may result in particles with toxic problem and large particle size. Studies concerning the fabrication of silk fibroin nanoparticles based on supercritical CO₂ technology have not been reported. Besides, the nanoparticle formation mechanism in supercritical CO₂ technology including the SEDS process is still not clear.
- (2) Studies about utilizing silk fibroin nanoparticles prepared by the SEDS process as drug carrier are lacking. Particularly, there is no related research to use SEDS process to prepare drug loaded silk fibroin nanoparticles.
- (3) Most studies about drug carriers focus on the synthetic biodegradable polymers, so studies about silk fibroin/ PLLA-PEG-PLLA copolymer as

SF/PPP nanoparticles drug carriers are still lacking due to limitation of the technology.

(4) Poor water solubility and adverse effects of many important anticancer agents including paclitaxel (PTX) has limited its therapeutic efficiency. Clinically approved nanoparticle drug delivery system such as PTX-SF/PPP for cancer is very few.

(5) The studies about smart folic acid grafted SF/PPP nanoparticles (FA-SF/PPP) for tumor targeted drug delivery are insufficient and need to be developed to reduce side effects of drugs and enhance therapeutic efficiency.

In order to overcome the research gaps above and achieve the goal of developing effective silk fibroin-based nanoparticle drug release systems for tumor therapy, five objectives were generated and presented in Section 1.2 of Chapter 1.

Chapter 3 Study on formation of silk fibroin nanoparticles by the SEDS process

3.1 Introduction

Based on the extensive literature review in Chapter 2, it was found that the major disadvantages of traditional methods to prepare silk fibroin nanoparticle include toxicity problem, particle with big size and particle size distribution, high temperatures condition, *etc.* Chapter 3 aims to overcome these problems and achieve the objective 1 described in Section 1.2 of Chapter 1.

In this Chapter, solution-enhanced dispersion by supercritical CO₂ (SEDS) was used to prepare the silk fibroin nanoparticles. It is a modified SAS process, in which the silk fibroin dissolved in organic solvent and scCO₂ are atomized through a coaxial nozzle into higher pressure vessel. A full factorial experiment was designed to perform a systematic investigation of the actual effects of the process parameters, including the flow rate of silk fibroin solution, precipitation pressure, concentration of silk fibroin solution and precipitation temperature, on the particle size (PS) and particle size distribution (PSD). Furthermore, experimental and theoretical investigations of the nanoparticle formation mechanism were presented.

3.2 Experimental Section

3.2.1 Materials

Cocoons of *Bombyx mori* were purchased from the Jiangsu Wujing China Eastern Silk Market Co. Ltd. CO₂ with a purity of 99.9% was purchased from the Hong Kong Specialty Gases Co. Ltd.. The solvent, 1,1,1,3,3,3-Hexafluoroisopropanol (HFIP, 99%), was purchased from Dupont.

3.2.2 Preparation of pure silk fibroin (SF) raw material

Cocoons of *Bombyx mori* were degummed three times to eliminate sericin on the surface of silk fiber in a water bath at 120 °C for 60 min. Afterwards, the deionized water was used to wash the fibroin fibers and then dry it at room temperature. Degummed SF fibers were dissolved in a calcium chloride-ethanol system (molar ratio of CaCl₂: water: ethanol=1:8:2) for 6 h at 70 °C to obtain the SF solution. Then the solution was purified by dialyzing in the deionized water for 72 hours to eliminate the impurities with acellulose dialysis membrane (MWCO 12,000-14,000) and obtain the pure silk fibroin solution. Subsequently, dry samples of pure silk fibroin were obtained by lyophilizing with a freeze dryer.

3.2.3 Preparation of silk fibroin nanoparticles by the SEDS process

The SEDS apparatus used for the preparation of nanoparticles is made up

of three major sections: a CO₂ supply system, an organic solution delivery system, and a high pressure vessel [139]. The schematic diagram of the SEDS process is shown in Figure 3.1. In the SEDS process, the CO₂ cylinder vented a large amount of CO₂, which was cooled down to about 0 °C by a cooler to avoid cavitations and maintain the liquefaction of the gas before it entered the pump. Then liquefied CO₂ was pumped into the high pressure vessel by a high pressure pump. The precipitation temperature was kept at a constant level by placing the high pressure vessel in a gas bath. The desired precipitation temperature can be achieved by heating the liquefied CO₂ via a heat exchanger and keeping the gas bath at desired temperature.

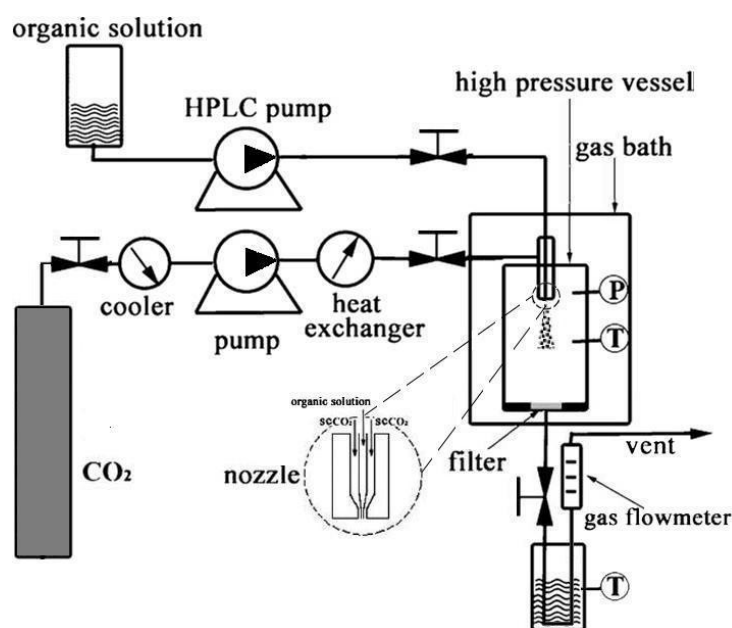


Figure 3.1 Schematic diagram of the apparatus for the SEDS process

When the desired pressure and temperature that kept the CO₂ in a supercritical state were obtained, the flow rate of carbon dioxide was fixed, and the precipitation pressure could be adjusted by controlling a downstream valve

and monitored by a pressure gauge to keep the pressure constant. The silk fibroin solution dissolved in 1,1,1,3,3,3-Hexafluoroisopropanol (HFIP) was then injected into the high-pressure vessel via a specially designed nozzle simultaneously with the supercritical CO₂ using an HPLC pump and precipitation took place. The silk fibroin solution and supercritical CO₂ was delivered via the inner part of and the external passage of the nozzle, respectively. The mixing between the solution and supercritical CO₂ can be enhanced by specially designed nozzle. After all the solution was delivered into high pressure vessel, fresh CO₂ was pumped to wash precipitated particles for about 30 min to eliminate the residual organic solvent. In the washing process, the precipitation temperature and pressure were kept as described above. After the washing process, the CO₂ flow was stopped and the pressure of CO₂ in the high pressure vessel was slowly depressurized to atmospheric pressure. The silk fibroin nanoparticles were then collected on the filter at the bottom of the high pressure vessel for characterization.

3.2.4 Full factorial designs (FFD)

In this study, the four main process parameters of the SEDS process were identified as follows: the flow rate of silk fibroin solution, precipitation pressure, concentration of silk fibroin solution and precipitation temperature. To study the effect and significance of the four process parameters in SEDS process on the morphology, particle size and particle size distribution of silk fibroin nanoparticles respectively, a 2⁴ full factorial experiment was performed.

Experimental factors and levels are shown in Table 3.1. According to factorial designs there are 16 experiments (shown in Table 3.2). Analysis of variances was performed based on the experimental data by statistical/quantitative method.

Table 3.1 Experimental factors and levels

Symbols	Factors	Coded level	
		-1	+1
A	Flow rate of SF solution (ml min ⁻¹)	0.5	1
B	Precipitation pressure (MPa)	10	20
C	The concentration of SF solution (mg ml ⁻¹)	0.5	1
D	Precipitation temperature (°C)	35	45

3.2.5 Surface morphology and particle size

The surface morphology of silk fibroin nanoparticles was visualized by a field emission scanning electron microscopy (FE-SEM, JEOL, JSM-6490, Japan). Before analysis, silk fibroin nanoparticles were attached onto a carbon paint and then placed on an aluminum sample holder. Silk fibroin nanoparticles were made conductive by sputtering a thin layer of gold onto their surface. The particle size (PS) and particle size distribution (PSD) of silk fibroin nanoparticles dispersed in ethanol by sonication were measured by a laser diffraction particle size analyzer with a liquid module (LS 13320, Beckman Coulter, USA).

3.3 Results and discussion

3.4 Surface morphology, particle size and particle size distribution of silk fibroin nanoparticles

Figure 3.2 shows FE-SEM photos of the silk fibroin nanoparticles fabricated by the SEDS process in different runs shown in Table 3.2. It can be noted that some of the silk fibroin nanoparticles had a tendency to aggregate together. This may be caused by the small particle size and surface activity of the high reunion [140].

However, these aggregates can be separated when the powder is suspended in ethanol and dispersed by sonication. Table 3.2 shows the experimental design and results of 2^4 full factorial design. Particle size (PS) and particle size distribution (PSD) defined as $(D90-D10)/D50$ varied markedly under the conditions tested. From Figure 3.2 and Table 3.2, it can be seen that the silk fibroin nanoparticles possess an irregular spherical morphology with a mean particle size from about 52.5 nm to 102.3 nm and particle size distribution (span) from 0.32 to 0.66. Various morphologies indicated that the process parameters in the SEDS process have a significant effect on the surface morphology, PS and PSD. Furthermore, by adjusting the different process parameters, silk fibroin nanoparticles with a controlled particle size and size distribution can be obtained.

Table 3.2 Experimental design and results of full factorial design

Run	A	B	C	D	Particle size and particle size distribution					
					Mean size	SD	D10	D50	D90	Span
					(nm)		(nm)	(nm)	(nm)	(D90– D10)/D50
1	-1	-1	-1	-1	64.9	0.5	55.9	62.4	79.7	0.38
2	1	-1	-1	-1	76.0	1	57.5	74.8	92.7	0.47
3	-1	1	-1	-1	52.5	0.9	52.7	50.6	68.9	0.32
4	1	1	-1	-1	70.2	0.8	64.4	68.5	91.8	0.40
5	-1	-1	1	-1	78.5	2.5	56.9	78.2	98.4	0.53
6	1	-1	1	-1	90.4	1	75.9	88.9	132.8	0.64
7	-1	1	1	-1	76.1	0.9	64.6	74.2	102.5	0.51
8	1	1	1	-1	81.6	0.6	64.8	81.2	108.6	0.54
9	-1	-1	-1	1	66.5	0.5	53.8	65.8	79.5	0.39
10	1	-1	-1	1	80.5	0.5	68.9	80.5	109.2	0.50
11	-1	1	-1	1	54.8	0.4	52.1	54.3	71.6	0.36
12	1	1	-1	1	72.6	1	68.7	72.5	98.4	0.41
13	-1	-1	1	1	81.4	1.5	61.2	80.8	109.7	0.60
14	1	-1	1	1	102.3	2	71.1	100.5	137.4	0.66
15	-1	1	1	1	77.8	0.8	46.5	76.9	94.2	0.62
16	1	1	1	1	87.5	1.4	63.3	86.7	114.5	0.59

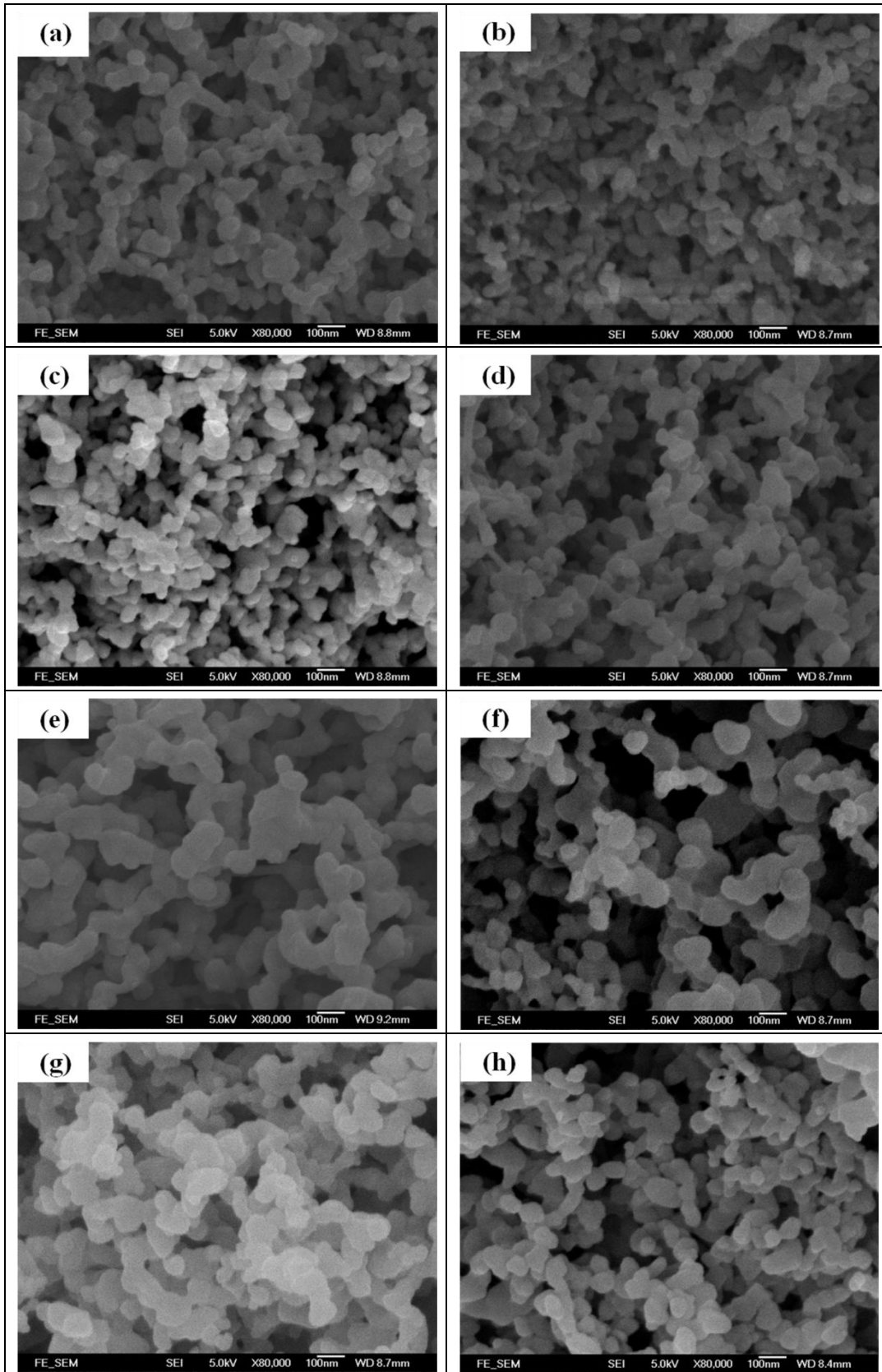


Figure 3.2 FE-SEM photos of silk fibroin nanoparticles prepared by the SEDS process under different concentration of silk fibroin (a) 45 °C-0.5% SF-20 MPa-1

ml min⁻¹, (b) 45 °C-0.5% SF-20 MPa-0.5 ml min⁻¹, (c) 35 °C-0.5% SF-20 MPa-0.5 ml min⁻¹, (d) 35°C-1% SF-20 MPa-0.5 ml min⁻¹, (e) 45 °C-1% SF-10 MPa-1 ml min⁻¹, (f) 45 °C-1% SF-20 MPa⁻¹ ml min⁻¹, (g) 45 °C-0.5%SF-10 MPa-1 ml min⁻¹ and (d) 35 °C-0.5% SF-10 MPa-1 ml min⁻¹

3.5 Influence of the process process parameters on particle size and particle size distribution

The full factorial design can cover the main effects of the parameters including flow rate of SF solution (A), precipitation pressure (B), The concentration of SF solution (C) and precipitation temperature (D) on PS and PSD of SF nanoparticles within the whole range of those selected. The results of quantitative analysis about the results of full factorial design has been shown in Table 3.3. Figure 3.3 shows the standardized effect of the factors on particle size (a) and main effects plot for particle size (b).

Table 3.3 Estimated Effects and Coefficients for Particle size (nm) (coded units)

Term	Effect	Coef	SE Coef	T	P
Constant		75.884	0.2824	268.74	0.000
A	13.556	6.778	0.2824	24	0.000
B	-8.481	-4.241	0.2824	-15.02	0.000
C	17.306	8.653	0.2824	30.64	0.000
D	4.206	2.103	0.2824	7.45	0.000

Table 3.4 Estimated Effects and Coefficients for Span (coded units)

Term	Effect	Coef	SE Coef	T	P
Constant		0.49250	0.001976	249.19	0.000
A	0.06375	0.03188	0.001976	16.13	0.000
B	-0.05125	-0.02562	0.001976	-12.97	0.000
C	0.18375	0.09188	0.001976	46.49	0.000
D	0.03000	0.01500	0.001976	11.07	0.000

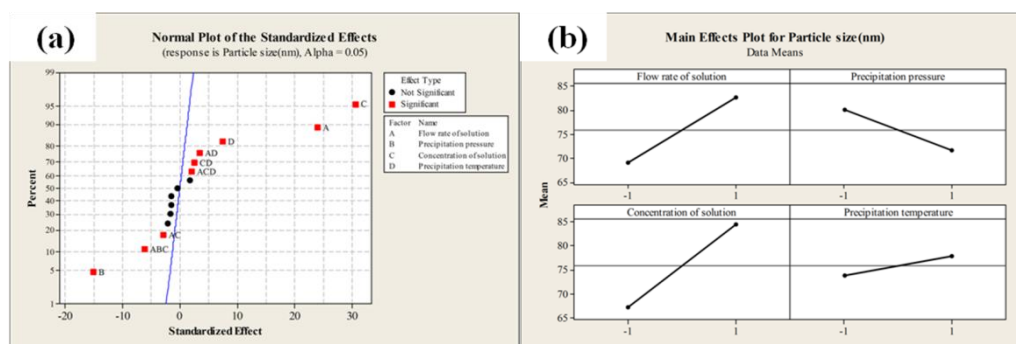


Figure 3.3 Standardized effect of the factors on (a) particle size and (b) main effects plot for particle size

As shown in Figure 3.3 (a) and Table 3.3, A, B, C, and D ($P < 0.001$) significantly affect the particle size (PS) and the importance of the parameters for PS could be arranged in the following order: $C > A > B > D$. This result was also demonstrated by the slopes of the lines shown in Figure 3.3 (b). Within the range of parameters selected, the PS increased with increasing concentration or flow rate of the solution, and decreasing precipitation pressure. The effect of

precipitation temperature alone on the particle size was not obvious, and decreasing the temperature reduced the particle size of silk fibrion nanoparticles slightly.

Similar analysis using a full factorial design was performed for the particle size distribution (PSD). A smaller span indicated a narrower PSD. Figure 3.4 indicates the standardized effect of the factors on particle size distribution (a) and main effects plot for particle size distribution (b). As shown in Figure 3.4 (a) and Table 3.4, A, B, C, and D ($P < 0.001$) significantly affect PSD. From the relative slope shown in Figure 3.4 (b) and Table 3.4, it has been shown that the concentration of the solution has the the most significant effect. The flow rate of the solution and precipitation pressure exhibit comparatively negligible effect. In addition, the precipitation temperature had a slight effect. Furthermore, the concentration, flow rate of solution and the precipitation temperature had positive effect on PSD. In contrast, the precipitation pressure had a negative effect.

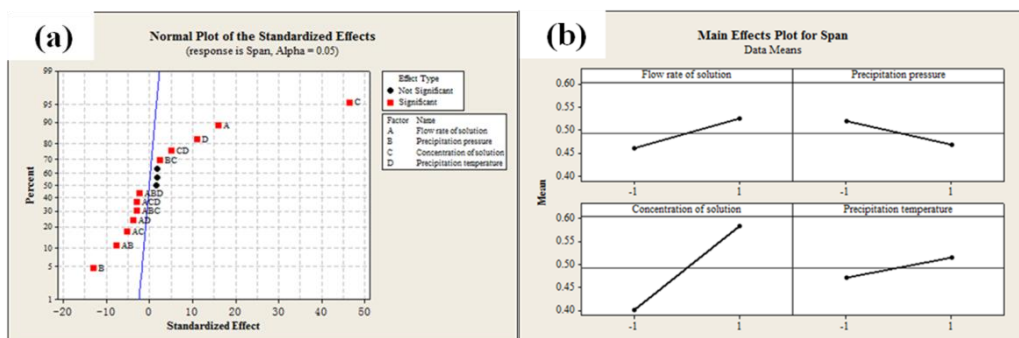


Figure 3.4 Standardized effect of the factors on (a) particle size distribution and (b)

main effects plot for particle size distribution

3.6 Silk fibroin nanoparticle formation mechanism

The SAS process involves fluid dynamics, surface tension variations, mass transfer, vapor liquid equilibria (VLEs), nucleation and growth mechanisms, which are complementary and when taken together, can give a comprehensive description of the SAS process. However, the nanoparticle formation mechanism is still not readily understood. 2^4 full factorial design experiments can investigate the effect of key process parameters systematically, including concentration, flow rate of solution, precipitation temperature and precipitation pressure on PS and PSD. Thus, 2^4 full factorial design will be very useful to study the nanoparticle formation mechanism.

Figure 3.2 shows the FE-SEM photos of silk fibroin nanoparticles fabricated using the SEDS process. As shown in these images, all silk fibroin nanoparticles possessed irregular spherical shape. Therefore, it can be concluded that the resulting nanoparticles were generated from a gaseous miscible phase, not by droplet drying directly. Otherwise, the surface tension of the droplets will confer them a perfectly spherical shape [141]. Therefore, the nucleation and growth mechanism can be used to explain the generation of silk fibroin nanoparticles. However, when the solution was pumped into the higher pressure vessel, the solution and the scCO₂ in the vessel were not in equilibrium in a very short period of time. The initial droplets will be induced by a liquid-liquid phase split. Therefore, the mutual mass transfer between scCO₂ and the solution will occur until the completely miscible mixture of scCO₂ and the

solution was obtained [142].

3.6.1 Effect of flow rate of solution

In the SAS process, an increase in solution flow rate may cause competing effects [143]. On one hand, mixing energy between solution and scCO₂ can be improved. Obviously, supersaturation can be increased. Thus, particle size of the products will be decreased. On the other hand, it also could reduce the CO₂ mole fraction in the precipitator and decrease the mass transfer rate of solution out of the droplets, consequently inhibiting the particle formation.

In this study, an increase in the flow rate of silk fibroin solution resulted in larger PS and PSD, supported by the surface morphologies of silk fibroin nanoparticles shown in Figure 3.2 (a) and (b). The lower flow rate of the solution (0.5 ml/min of Run 11 in Table 3.2) yielded smaller particles of 54.8 nm with a PSD of 0.36, and the higher flow rate (1 ml/min of Run 12 in Table 3.3) generated larger particles of 72.6 nm with a PSD of 0.41. Therefore, in the experimental system, enhancement of mass transfer between scCO₂ and the solution with a decreasing flow rate was observed as a dominant factor in relation to the flow rate effect.

This result can be explained by the nucleation and growth mechanism induced by supersaturation, which is determined by the mass transfer between scCO₂ and the solution. As shown in

Figure 3.5 (a), a higher flow rate of the solution could generate much

solution in the precipitator within the same time, which led to the increase of the liquid film thickness [144], and reduced the anti-solvent effect of scCO₂ and the mass transfer rates between scCO₂ and the droplets, therefore decreasing the achievable supersaturation ratio. Lower super-saturation ratios resulted in fewer nuclei, which in turn yielded larger particles. And the micronization process will shift towards the growth process and larger particle with a broad particle size distribution are formed [144]. Therefore, in the condition of higher flow rate of the solution, lower mass transfer between scCO₂ and solution induced abatement of supersaturation and cause the final particles to become larger and non-uniform. Similar experimental results have been observed by other authors [145, 146]. Obviously, it can demonstrate that the mass transfer between scCO₂ and solution play a crucial role in silk fibroin nanoparticle formation.

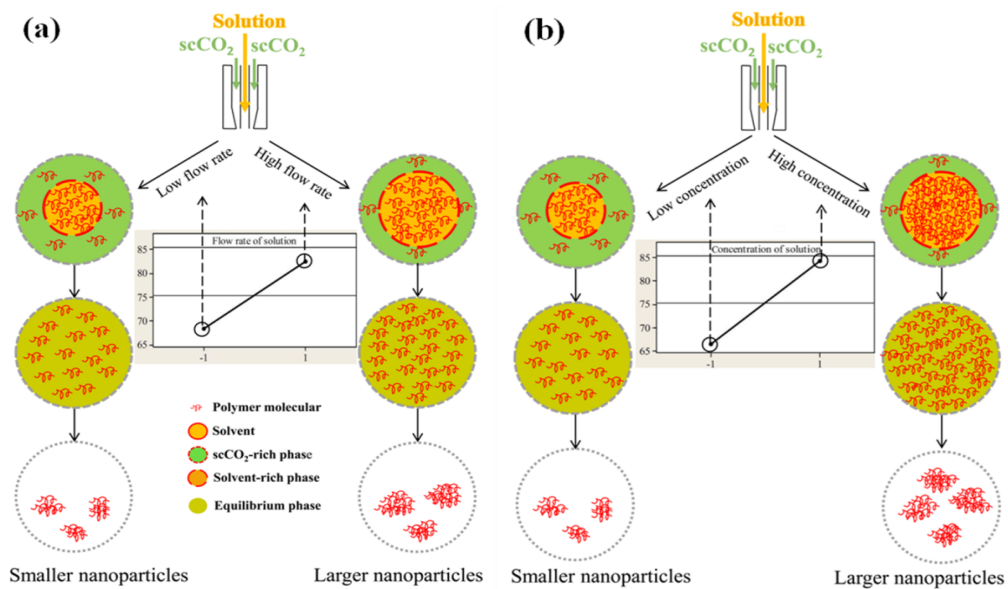


Figure 3.5 Mechanism for (a) main effects of the flow rate and (b) concentration of solution on the particle size of silk fibroin nanoparticles in the

3.6.2 Effect of the concentration of solution

The concentration of solution could possess two opposite effects on the PS and PSD [160]. According to the classical nucleation and growth theory, bigger concentration can induce higher supersaturation, which will incline to decrease the PS and PSD. However, as shown in

Figure 3.5 (b), a lower concentration with less molecular number of silk fibroin would reduce the viscosity and surface tension of the liquid solution at the moment the solution was delivered via the nozzle into the high pressure vessel [147], and therefore, produce smaller initial droplet, which could enhance mass transfer between scCO₂ and solution. Thus the supersaturation would occur more rapidly. It obviously favored the formation of smaller homogeneous nuclei and size distribution. Therefore, nucleation was the prevailing mechanism, resulting in smaller particles.

In the present study, Figure 3.3 and Figure 3.4 show that the concentration of solution has the greatest significant effect on PS and PSD. The higher the concentration of the solution, the large the particles and wider the particle size distribution. When concentration was raised from 0.5% to 1% as indicated in Figure 3.2 (c) and (d), the PS and PSD of silk fibroin nanoparticles increased from 52.5 nm and 0.32 of Run 3 to 76.1 nm and 0.51 of Run 7 shown in Table 3.2 respectively. The similar positive effect of the concentration on PS

and PSD has been reported by many researchers [148,149]. Therefore, this result indicated mechanism shown in

Figure 3.5 (b) is a main mechanism to form the silk fibroin nanoparticles. Therefore, mass transfer between scCO₂ and solution superimposed on the supersaturation and that it was also the single most important process parameter affecting the nanoparticle formation. Otherwise, the higher supersaturation induced by higher concentration will result in smaller PS and PSD. The analysis thus demonstrated the effect of the flow rate of solution.

3.6.3 Effect of precipitation pressure

The precipitation pressure also influences the formation of silk fibroin nanoparticles in the SEDS process. The results shown in Fig. 3b and 4b indicate that the PS and PSD was reduced by increasing the precipitation pressure. Runs 14 and 16 in Table 3.2 show that increasing the pressure from 10 MPa to 20 MPa can lead to a decrease in the PS and PSD of silk fibroin nanoparticles from 102.3 nm and 0.66 to 87.5 nm and 0.59, respectively. This trend was also observed in surface morphology of silk fibroin nanoparticles as shown in Figure 3.2 (e) and (f). Jin *et al.* [150] also reported similar results.

An increase in pressure led to an increase in the CO₂ density and mole fraction, thus enhancing the anti-solvent effect of the CO₂ and mass transfer rate between scCO₂ and solution. Therefore, supersaturation within the liquid phase was reached more quickly and it prevented the crystals from growing and

induced particle formation with smaller size and narrower size distribution [150]. However, reducing precipitation pressure also could decrease the solubility, which is inclined to generate higher maximum supersaturation, and resulting in smaller particles with a narrow PSD [151]. Within the processing conditions used in the present study, the first effect proved to be predominant owing to positive effect of precipitation pressure on PS and PSD. Therefore, the mechanism shown in Figure 3.6 (a) is a possible mechanism to effect the formation of silk fibroin nanoparticles. Furthermore, mass transfer between scCO₂ and solution possessed more significant effect on the PS and PSD of silk fibroin nanoparticles in the SEDS process. These results are consistent with that of analysis about the effects of the flow rate of the solution and the concentration of the solution on the PS.

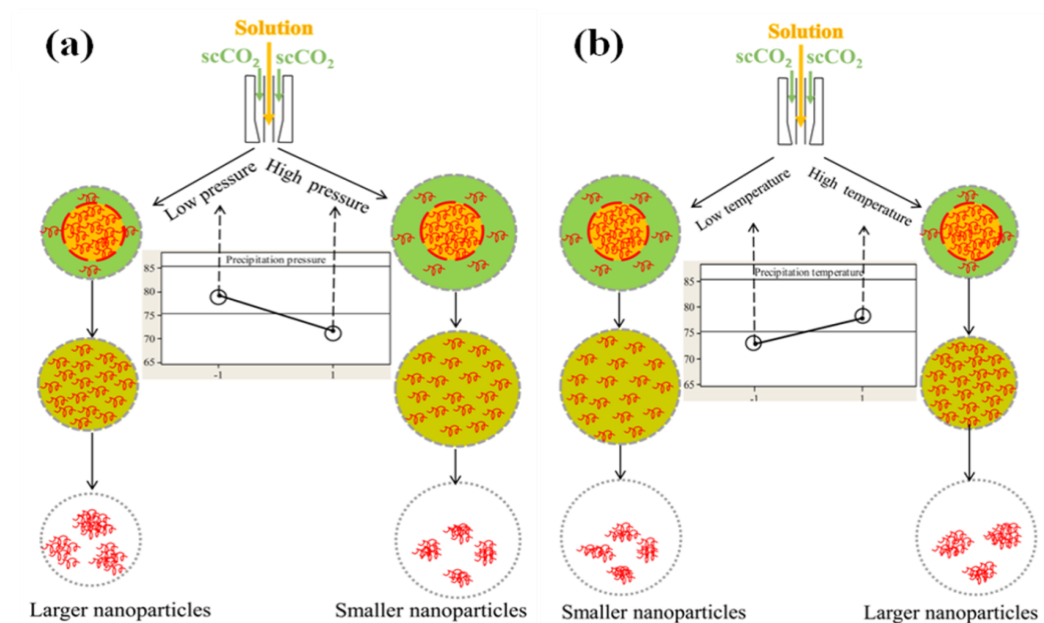


Figure 3.6 Mechanism for (a) main effects of precipitation pressure and (b) temperature on the particle size of silk fibroin nanoparticles in the SEDS process

3.6.4 Effect of precipitation temperature

The precipitation temperature, like the precipitation pressure, can affect the density of scCO₂ and thus mass transfer between scCO₂ and solution in the SEDS process. Especially near the critical point, a minor change in temperature of fluid will result in a significant change in the density of fluid [151]. Figure 3.3 and Figure 3.4 suggest that temperature exerts a comparatively negligible influence on the PS and PSD, and decreasing the temperature can reduce the PS and PSD of silk fibroin nanoparticles. Run 2 and Run 10 in Table 3.2 show that increasing the temperature from 35 °C to 45 °C can result in a slight increase in PS and PSD of silk fibroin nanoparticles from 76 nm and 0.47 to 80.5 nm and 0.50 respectively. The morphologies shown in Figure 3.2 (g) and (h) demonstrate this trend.

As shown in Figure 3.6 (b), the density of scCO₂ depended on temperature and pressure of scCO₂, an increase in temperature caused a decrease in density of CO₂, resulting in reducing mass transfer rate between scCO₂ and solution and thus slowing achievement of supersaturation. Therefore, a larger particle with wider particle size distribution will form. Lee *et al.* [152] also indicated a similar phenomenon. However, increasing the temperature could reduce the solubility and thus enhance the maximum supersaturation, so that particle size of the product will be decreased. In the present study, the slight increase in PS and PSD with increasing temperature indicated that effect of mass transfer between CO₂ and solvent superimposed on that of solubility, which also is driven by the former.

Therefore, the nanoparticle formation mechanism shown in Figure 3.6 (b) can explain the effect of pressure on the PS and PSD.

3.6.5 Silk fibroin nanoparticle formation mechanism

In summary, the non-perfect spherical morphology of silk fibroin nanoparticles prepared under the operating conditions by the SEDS process indicate that nanoparticles formed due to nucleation and growth in the gaseous miscible phase evolved from initial droplets. The analysis of the main influences of the operating factors on PS and PSD suggested that mutual mass transfer between scCO₂ and the solution was superimposed on the supersaturation and is the most important process parameter affecting nanoparticle formation. Lower concentration and flow rate of the solution, lower temperature and higher pressure enhance the mass transfer rate between scCO₂ and the solution and generate a higher degree of supersaturation. Therefore, a large number of smaller nuclei form. Meanwhile the ratio of nucleation to growth process will become higher, which will result in a lower degree of growth process and thus a smaller particle size distribution.

Based on the analysis above, a possible silk fibroin nanoparticle formation mechanism for the SEDS process can be proposed. Figure 3.7 shows a schematic diagram of this possible mechanism. In the SEDS process, at the moment that the solution is atomized into the high pressure vessel, the solution and scCO₂ in the vessel are not in equilibrium. So within a very short period of time, initial

droplets will be induced by a liquid-liquid phase split. Then the droplets will expanded rapidly due to the mutual mass transfer between the solution and scCO₂, leading to a significant decrease in the strength of the solvent. Thus, the solvent-rich phase and CO₂-rich phase is formed. In the process of adding the solution into scCO₂, a little amount of silk fibroin will be dissolved in the mixture of scCO₂ and the solvent until the mixture containing silk fibroin reached saturation point. Then the completely miscible mixture of silk fibroin, organic solvent and scCO₂ forms. Continued feeding of the solution into scCO₂ will cause crossing over the equilibrium boundary and supersaturation of silk fibroin in the mixture of scCO₂ and the solvent. Subsequently, a phase transition takes place in the solvent-rich phase, resulting in the formation of polymer nuclei and a polymer-rich phase. Because of the continued mass transfer between the solvent and scCO₂, the nuclei formed in the supersaturated polymer solution quickly grow to larger polymer nanoparticles. Finally, the residual organic solvent can be eliminated from the resulting nanoparticles by fresh scCO₂ to obtain pure polymer nanoparticles.

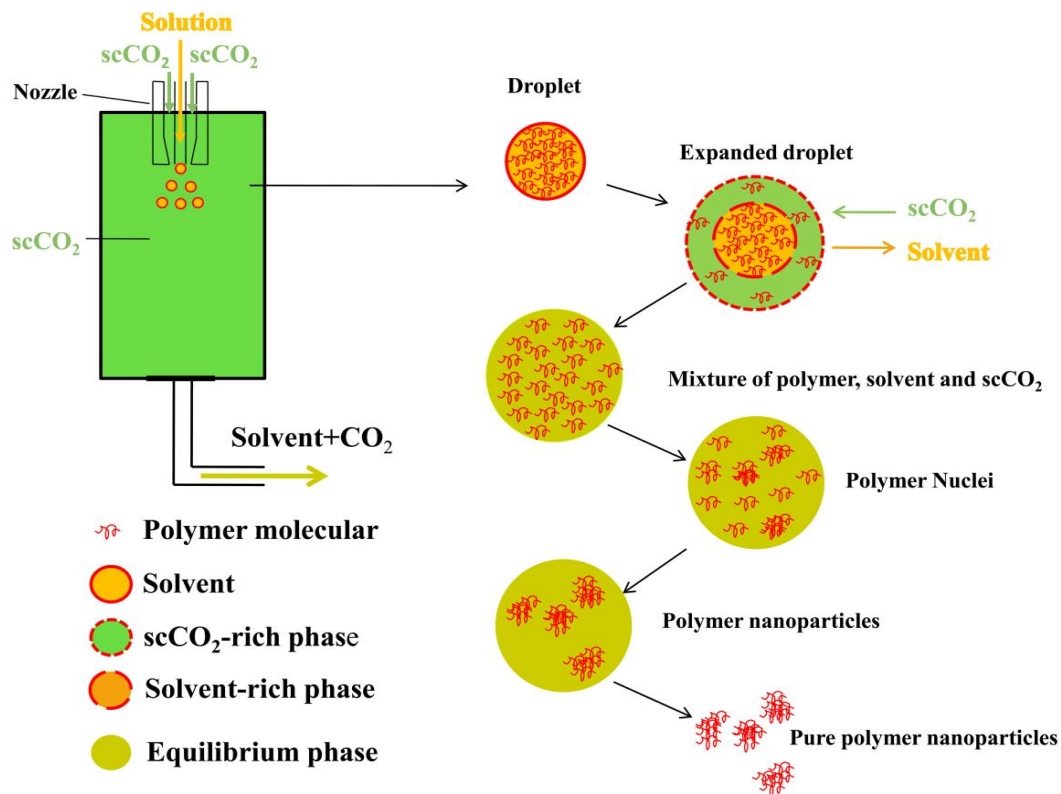


Figure 3.7 Mechanism diagram for silk fibroin particle formation by the SEDS process

3.7 Summary

In this Chapter, silk fibroin (SF) nanoparticles with particle size from 52.5 nm to 102.3 nm and particle size distribution (span) from 0.32 to 0.66 were fabricated using solution-enhanced dispersion by supercritical CO₂ (SEDS) successfully. The investigation using 2⁴ full factorial design indicated that increasing the concentration and the flow rate of silk fibroin solution and precipitation temperature raised the PS and PSD of silk fibroin nanoparticles, while reducing the precipitation pressure decreased the PS and PSD. The nanoparticle formation mechanism could be elucidated with formation and

growth of silk fibroin nuclei in gaseous miscible phase evolved from initial droplet generated by liquid-liquid phase split. The mutual mass transfer between supercritical CO₂ (scCO₂) and solution superimposed on the supersaturation and was the most important process parameter to affect nanoparticle formation. Considering the representative characteristic of silk fibroin, the SEDS process could be a promising technique to prepare silk fibroin nanoparticles applied in textiles, cosmetic and biomedical fields.

Chapter 4 Characterization of silk fibroin nanoparticles and their potential application as drug carrier

4.1 Introduction

Silk fibroin nanoparticles were fabricated by the SEDS process successfully in Chapter 3. Moreover, the SEDS process has been optimized by investigating the effect of parameters process on particles size and particle size distribution of silk fibroin nanoparticles. In particular, a possible mechanism has been proposed to explain the formation of silk fibroin nanoparticles by the SEDS process. In the Chapter 4, study will focus on exploring the application of silk fibroin nanoparticles in order to achieve objective 2 of this project described in Section 1.2 of Chapter 1.

In this Chapter, in order to utilize the silk fibroin nanoparticles prepared by the SEDS process as drug carrier, silk fibroin nanoparticles were treated with ethanol to induce β -sheet formation and thus water insolubility firstly. Then the morphology and physicochemical properties of silk fibroin nanoparticles before and after ethanol treatment were investigated. Furthermore, biological evaluation about the biocompatibility and cellular uptake behavior of SF nanoparticles were conducted. Finally, paclitaxel (PTX) and indomethacin (IDMC) were chosen as model drug to be loaded into the SF nanoparticles to study drug loading and release properties of the SF nanoparticles.

4.2 Preparation of SF nanoparticles and drug loaded SF nanoparticles by the SEDS process

Silk fibroin (SF) nanoparticles can be prepared by using the method described in Section 3.2.2 of Chapter 3. The operating conditions were described as follows (P: 20MPa, T: 35 °C; concentration of solution: 0.5%; flow rates of scCO₂: 0.5 ml min⁻¹, respectively). For the preparation of Indomethacin loaded silk fibroin (IDMC-SF) or paclitaxel loaded silk fibroin (PTX-SF) nanoparticles, Indomethacin (99% EP/USP/BP, Advanced Technology & Industrial Co. Ltd. Hong Kong) or paclitaxel (Meilian Pharmaceutical Co. Ltd. Chongqing, China) with four times the weight of the SF was completely dissolved with the SF in HFIP solvent. The concentration of IDMC-SF or PTX-SF in solvent was 0.5% (w/v). The experiments were conducted under the conditions described as above (P: 20 MPa, T: 35 °C, concentration of solution: 0.5%, flow rates of scCO₂: 0.5 ml min⁻¹, respectively)

4.3 Surface morphology and particle size distribution

Field emission scanning electron microscopy (FE-SEM) described in Section 3.2.5 of Chapter 3 was used to identify the surface morphology of the samples. By combining the FE-SEM images and the findings on the size of silk SF nanoparticles, measured by a light scattering particle analyzer, the PS and PSD of the SF nanoparticles can be determined [12]. Figure 4.1 (a) and (b) show the FE-SEM photos of SF nanoparticles fabricated by the SEDS process before

and after ethanol treatment, respectively. Figure 4.2 shows the PSD of the SF nanoparticles dispersed in ethanol. The SF nanoparticles showed a spherical shape, a narrow PSD, and a mean PS of about 50 nm. After ethanol treatment, the surface morphology of the SF nanoparticles had no obvious change. However, the SF nanoparticles were inclined to aggregate partially and some agglomeration took place.

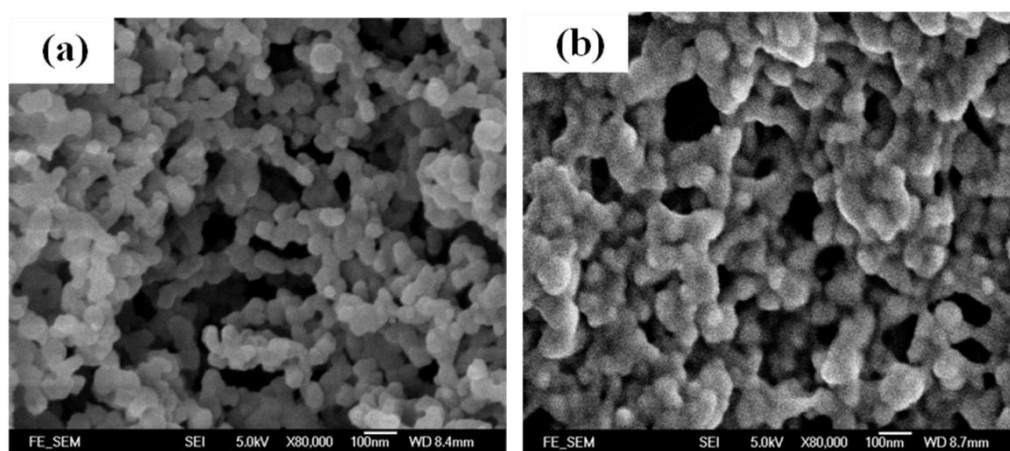


Figure 4.1 FE-SEM images of SF nanoparticles (a) before ethanol treatment and (b) after ethanol treatment



Figure 4.2 Particle size distribution of SF nanoparticles dispersed in ethanol

4.4 Chemical and physical properties

4.4.1 FTIR analysis

Method

The samples were combination with potassium bromide. Then the mixtures of the samples and potassium bromide were pressed into a transparent tablet. The FTIR spectras for the samples were recorded on an FTIR Perkin Elmer 1720 (Perkin Elmer, USA) in the transmission mode with the wave number ranging from 4,000 to 400 cm^{-1} .

Results and discussion

Fourier Transform Infrared Spectroscopy (FTIR) is an effective technique to analyze the chemical structure of a molecule by producing an infrared absorption spectrum [11]. Figure 4.3 shows the FTIR spectras of SF nanoparticles prepared by the SEDS process and WISF (SF nanoparticles after ethanol treatment); their corresponding characteristic peaks are marked on the Figure 4.3. It can be seen that the main characteristic peaks of amide I at 1658 cm^{-1} and amide II at 1541 cm^{-1} indicate that the silk fibroin nanoparticles obtained by the SEDS process is in mainly an amorphous form (random coil). After ethanol treatment, the main peaks at 1658 cm^{-1} and 1541 cm^{-1} shift to 1627 cm^{-1} and 1521 cm^{-1} , respectively. Therefore, the WISF nanoparticles possessed β -sheet structure predominantly and is water-insoluble. This result

indicates that the secondary structure of silk fibroin nanoparticles changed from random coil to β -sheet after exposure to ethanol [90]. The chemical shifts were similar to those of SF after methanol treatment [11].

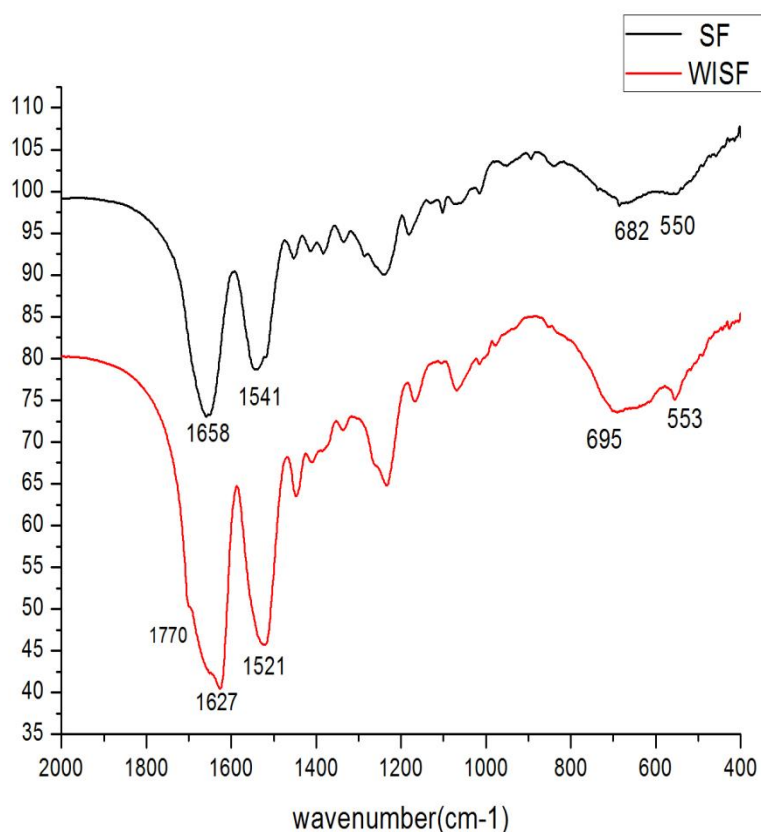


Figure 4.3 FTIR spectras of SF nanoparticles before and after ethanol treatment

4.4.2 XRPD analysis

Method

Powder X-ray diffraction (XRPD) was performed by an X-ray diffractometer with a Cu K α ($\lambda=1.5405 \text{ \AA}$) radiation (D8 Advance, Bruker AXS, Germany). The measurement was carried out in a 2θ range of $5\sim 45^\circ$ with a 0.02° step size and $10^\circ \text{ min}^{-1}$ scan speed with a 2D detector at 40 kV and 40 mA.

Results and discussion

To study the crystalline changes of nanoparticles after the SEDS process, XRPD analysis was carried out. Bombyx mori silk fibroin has a crystalline state (includes silk I, silk II, and silk III) and an amorphous state (random coil) in different conditions [58, 154]. Silk I is the glandular state prior to crystallization. Silk II and silk III are in β -sheet and α -helical conformation, respectively. Figure 4.4 shows the XRPD curves of SF nanoparticles prepared by the SEDS process and WISF (SF nanoparticles after ethanol treatment). On the XRPD curves, the characteristic peaks of silk I are found at $2\theta = 12.2^\circ$, while those of silk II are found at $2\theta = 9.6^\circ$ and 20.4° . A broad peak at 20.4° (random coil) and minor peaks at 9.6° and 12.2° suggest that SF before ethanol treatment is composed of both the random coil and the β -sheet forms with predominantly random coil conformation and the amorphous state. However, after ethanol treatment, the broad peak at 20.4° became sharp and the peaks at 12.2° also decreased. This result shows that a molecular rearrangement from random coil to β -sheet happened and SF nanoparticles became water-insoluble when they were treated with ethanol [89, 153].

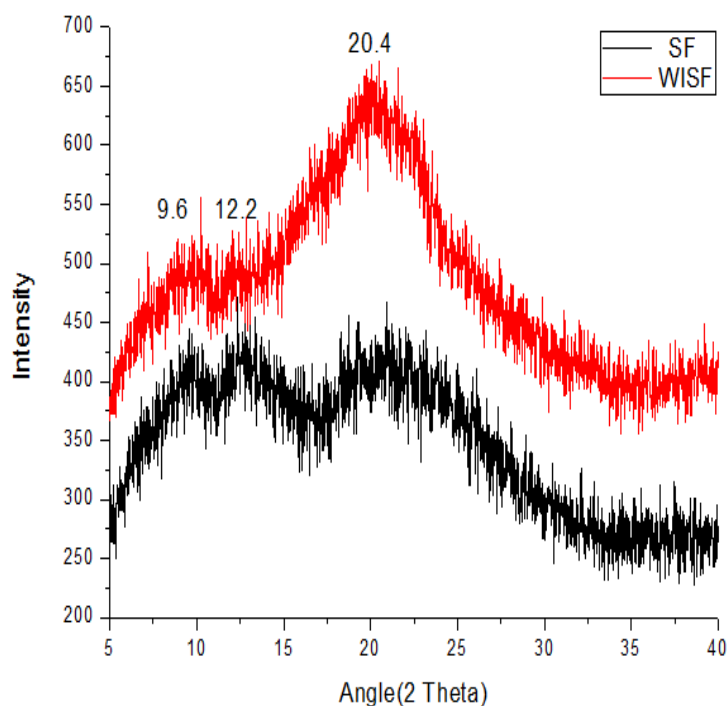


Figure 4.4 XRPD patterns of silk fibroin nanoparticles before and after ethanol treatment

4.4.3 Thermal properties

Method

The thermal properties of samples were analyzed by TG-DSC (Netzsch STA 449C, Burlington, Germany) at a heating rate of $10\text{ }^{\circ}\text{C min}^{-1}$ over a temperature range of 30 to $400\text{ }^{\circ}\text{C}$ in an N_2 atmosphere.

Results and discussion:

The Thermo Gravimetry-Differential Scanning Calorimeter (TG-DSC) is an effective tool to study the thermal behavior of particles under the influence of different atmospheres. Figure 4.5 reveals the TG-DSC curves of SF nanoparticles

prepared by the SEDS process and WISF (SF nanoparticles after ethanol treatment). Obviously, there is no significant difference about mass change between the SF nanoparticles and WISF. An endothermic peak at low temperatures below 100°C was contributed to the evaporation of water. With the increase of temperature, SF nanoparticles exhibited a broad endothermic peak at 191.6 °C, which was due to the glass transition. A subsequent obvious exothermic peak at 220.4 °C was resulted from crystallization into a β -sheet structure from a random coil conformation. The narrow endothermic peak at 290.1 °C was assigned to thermal melting/decomposition of β -sheet of silk fibroin. After ethanol treatment, the endothermic peak at 191.6 °C disappears owing to β -sheet structure of WISF induced by ethanol. Furthermore, a higher narrow endothermic peak at about 298.2 °C suggests that the increase of the thermal stability of silk fibroin is caused by the β -sheet arrangement of the silk fibroin molecules after ethanol treatment [89]. This result is consistent with the FTIR and XRPD results.

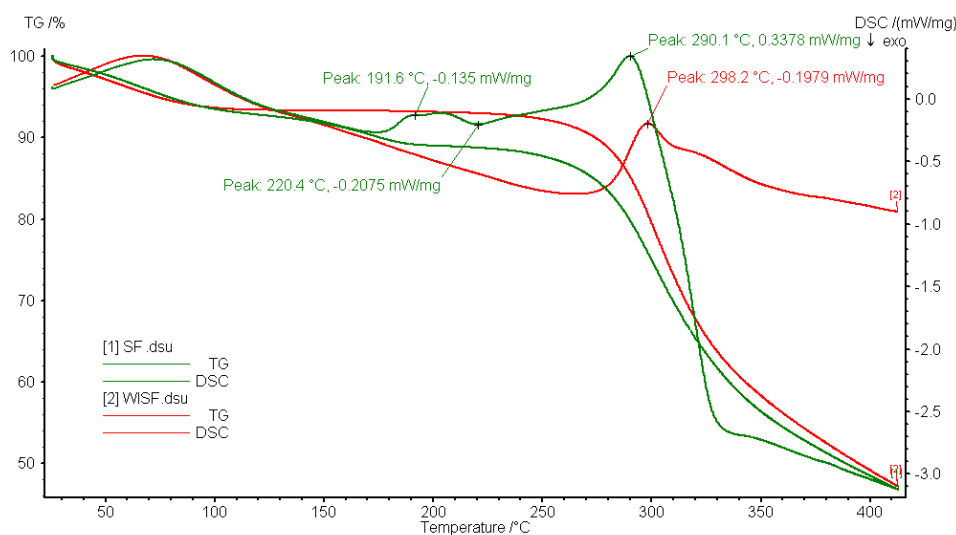


Figure 4.5 TG-DSC curves of silk fibroin nanoparticles before and after ethanol treatment

4.5 Biological evaluation of SF nanoparticles

The most important requirement for biomaterial to be applied in medical field such as drug delivery system is its compatibility not only in terms of physical and chemical properties, but also in terms of their biological response to body. Therefore, it is necessary to study biological evaluation of SF nanoparticles, including the biocompatibility and cellular uptake behaviors, *etc.* Here, MTS assay and LDH assay were used to evaluate the biocompatibility. And cellular uptake behavior was measured by fluorescence microscopy.

4.5.1 Cell culture

Human foreskin fibroblasts (HFF-1) were obtained from American Type Culture Collection (ATCC). Fibroblasts were grown in Dulbecco's modified Eagle's medium (DMEM) (Invitrogen), supplemented with 10% fetal bovine serum (Invitrogen), 1% penicillin (Invitrogen) and 1% streptomycin (Invitrogen). Cells were cultured in a humidified cell incubator at 37°C and 5% CO₂ atmosphere for confluence before experiments.

4.5.2 MTS assay

Method

The cytotoxicity of the silk fibroin (SF) nanoparticles was measured by MTS assay using the CellTiter 96® Aqueous One Solution Cell Proliferation Assay kit (Promega). MTS assay uses cell metabolic activity to reduce the MTS

tetrazolium compound to a colored water soluble formazan product. Briefly, water insoluble silk fibroin nanoparticles (WISF) obtained by 100% ethanol treatment were suspended in 70% ethanol for the sterilization process. After 24 h, the sample was centrifuged and the solvent was changed to 1×PBS (Sigma) as the stock solution. HFF-1 fibroblasts were pre-cultivated in the 24-well plates (NUNC) (2×10^4 cells /well) and allowed to adhere to the plate overnight. The next day the cell culture medium was replaced by the suspensions of WISF nanoparticles in completed DMEM (Dulbecco's modified Eagle's medium) at different concentration (10 µg/ml, 100 µg/ml, 1000 µg/ml). After 1 day, 3 days and 7 days of incubation in a humidified incubator with 5% CO₂ and at 37 °C, the culture medium was aspirated and cells were washed with 1×PBS for three times; 200 µl of the MTS solution mixed with 1ml fresh serum free medium was then added to each well and incubated with cells for another 4h. The reagents after cell incubation were then transferred to transparent 96-well plate (200 µl/well) for measurement. The absorbance values were measured using a Microplate Reader (infinite F200, TECAN) at 490 nm. The normalized cell metabolism activity of the fibroblasts exposed to WISF nanoparticles was expressed as the percentage of the untreated cells. All the experiments were performed in triplicate.

Results and discussion

One convenient method for assessing cell cytotoxicity is

3-(4,5-dimethylthiazol-2-yl)-5-(3-carboxymethoxyphenyl)-2-(4-sulfophenyl)-2H-tetrazolium(MTS) assay that measures mitochondrial enzymatic activity using a colorimetric reaction that occurs only in viable, proliferating cells. MTS assay measures the ability of viable cells to convert a soluble tetrazolium salt to a formazan product. The cell metabolic activity is directly related with cell viability and the number of live cells in the culture [156, 157]. Figure 4.6 shows the cell proliferation of fibroblasts after incubated with water-insoluble silk fibroin (WISF) nanoparticles after 1 day, 3 days and 7 days.

After 1 day of incubation, fibroblasts exposed to silk fibroin nanoparticles showed better cell viability compared to the untreated cells. And the corresponding cell viability of fibroblast is $100 \pm 1.5\%$, $102.3 \pm 4.9\%$, $108.3 \pm 4.2\%$ and $114 \pm 2.1\%$ when the concentration is 0, 10, 100 and 1000 $\mu\text{g/ml}$, respectively. Therefore, the SF nanoparticles at 100 and 1000 $\mu\text{g/ml}$ improved cell viability significantly.

When the incubation time was increased to three days, the cell viability slightly increased for fibroblasts incubated with the SF nanoparticles. However, no significant difference was found. After one week of incubation, the cell viability of fibroblasts incubated with the SF nanoparticles at a concentration of 10 $\mu\text{g/ml}$ is comparable to the control and increase significantly at concentration of 100 $\mu\text{g/ml}$. However, when the concentration was increased to 1000 $\mu\text{g/ml}$, the cell viability of fibroblasts decreased by about 20%. The present study showed that the SF nanoparticles only showed toxicity after long time incubation (7 days) and at

very high concentration (1000 $\mu\text{g/ml}$). Normally, nearly anything can be toxic at a high enough concentration [158]. Kundu *et al* reported that fibroblast cells incubated with silk fibroin nanoparticles prepared by a desolvation method at a concentration of 100 $\mu\text{g/ml}$ remained almost 100% viable relative to the control and the cell viability began to decrease at a concentration of 200 $\mu\text{g/ml}$ [58]. Compared with Kundu's work, the SF nanoparticles in the present study showed better biocompatibility.

Based on the cytotoxicity data obtained, it can be concluded that silk fibroin nanoparticles in the present study appear to be biocompatible and suitable for future studies *in vivo*.

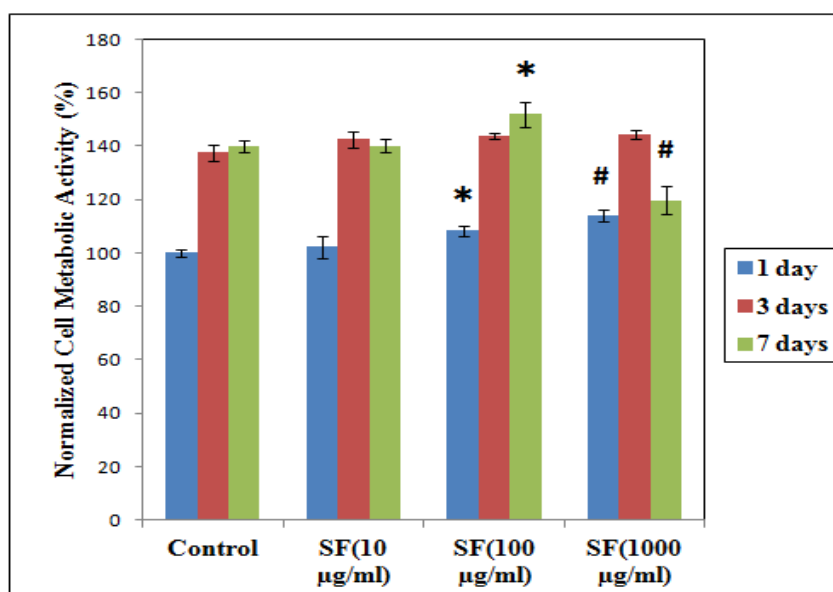


Figure 4.6 Cell proliferation of fibroblasts incubated with SF nanoparticles for 1 day, 3 days and 7 days measured with a MTS cell proliferation assay. The data are expressed as mean \pm standard deviation (SD) of three independent experiments.

An OD value of control cells (untreated cells) was taken as 100% viability (0%

cytotoxicity). p-values: # < 0.01; * < 0.05.

4.5.3 LDH assay

Method

Lactate dehydrogenase (LDH) activity assay is a colorimetric assay allows quantitatively measurement of LDH, a stable cytosolic enzyme released from damaged cells. The amount of released LDH can be determined by converting a tetrazolium salt (INT) into a red formazan product. The fibroblasts were seeded into 24 well plates at a density of 2×10^4 cells/well and incubated for 24 hours to allow cell attachment. SF nanoparticles at different concentration (10 $\mu\text{g/ml}$, 100 $\mu\text{g/ml}$, 1000 $\mu\text{g/ml}$) were added to each well and incubated for 1 day, 3 days and 7 days respectively. LDH assay was performed with Cytotoxicity Detection Kit (LDH) from Roche Diagnostic, Switzerland according to the manufacturer's instructions. Briefly, 25 μL cell free culture supernatant and 25 μL reaction mixture were added to each well of a 96 well plate. The reaction was incubated for 30 minutes in dark at room temperature. 25 μL stop solution per well was used to terminate the reaction. The OD values were subsequently read via the microplate reader (infinite F200, TECAN) at the wavelength of 490 nm using 750 nm as the reference. The relative cell cytotoxicity was determined by plotting the absorbance values normalized by the untreated cells. All the experiments were conducted in triplicate.

Results and discussion

Cytotoxicity can also be monitored by assessing cell membrane integrity based on lactate dehydrogenase (LDH) assay. LDH is one kind of soluble cytosolic enzyme present in most eukaryotic cells stably and can be released into the surrounding medium only after membrane damage. So, LDH activity is an effective indicator of cell membrane integrity and can be used to evaluate cytotoxicity [159, 160]. Absorbance at 490 nm is proportional to LDH release.

As shown in Figure 4.7, compared with fibroblasts without silk fibroin nanoparticle incubation, the viability of fibroblasts is almost 100 % and has no significant change after one day of incubation with 10, 100 and 1000 $\mu\text{g/ml}$ silk fibroin nanoparticles. With the increase of incubation time, a significant increase of LDH release was observed for fibroblasts incubated with 1000 $\mu\text{g/ml}$ PPP nanoparticles after 3 days, but there are no significant change for fibroblasts incubated with 10 $\mu\text{g/ml}$ and 100 $\mu\text{g/ml}$ SF nanoparticles. After 7 days of incubation, the LDH release of fibroblasts was significantly decreased for fibroblasts incubated with 10 $\mu\text{g/ml}$ and 100 $\mu\text{g/ml}$ SF nanoparticles by 15.6% and 13.1%, and the LDH release only increased for fibroblasts incubated with 1000 $\mu\text{g/ml}$ SF nanoparticles. Overall, SF nanoparticles at concentration (10 $\mu\text{g/ml}$ and 100 $\mu\text{g/ml}$) exhibited excellent biocompatibility. Even for long term cell incubation (7 days), SF nanoparticles at 10 and 100 $\mu\text{g/ml}$ can improve significantly cell viability. However, when exposing the fibroblasts to a high concentration of SF nanoparticles (1000 $\mu\text{g/ml}$) for 3 days and 7 days, cell

viability decreased obviously. In a word, the results of LDH assay supported that of MTS assay. Silk fibroin nanoparticles at a concentration of 10 and 100 $\mu\text{g/ml}$ can improve cell viability obviously and only show toxicity at a very high concentration after at least 3 days of incubation.

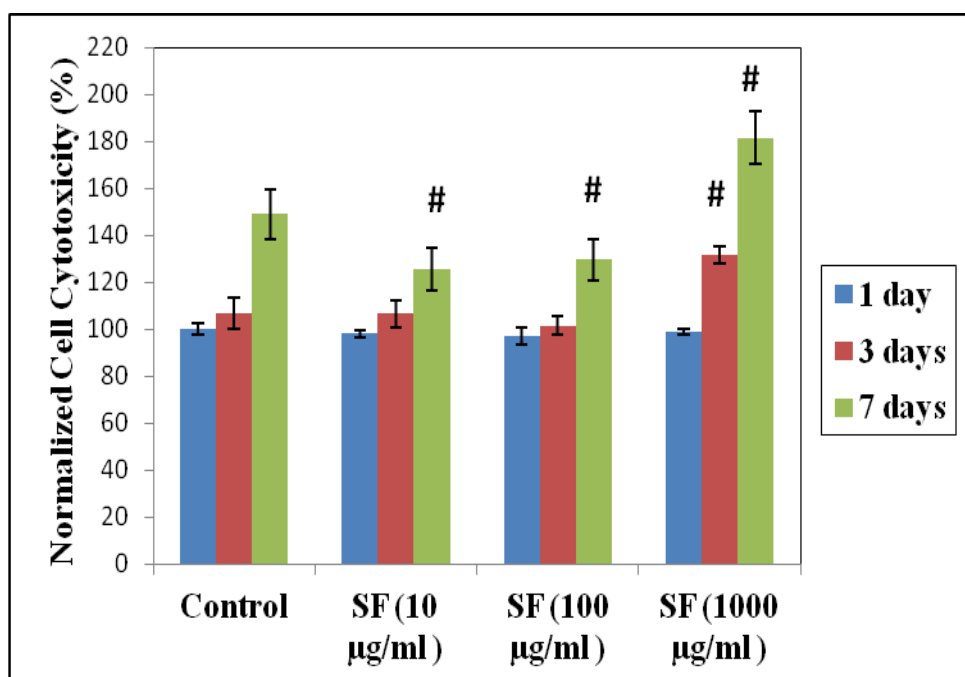


Figure 4.7 Cell proliferation of fibroblasts incubated with SF nanoparticles for 1 day, 3 days and 7 days measured with LDH assay. p-values: # < 0.01; * < 0.05.

It should be noted that silk fibroin nanoparticles at a high concentration (1000 $\mu\text{g/ml}$) reduced cell viability obviously when incubating with fibroblasts over 3 days. This phenomenon indicated that biological cells have an intrinsic limit in relation to the amount of degradable polymer nanoparticles they can incorporate without any alterations occurring. In the case of the systemic administration, nanoparticles could be endocytosed by the reticuloendothelial system (RES). Even though the mechanism concerning toxicity induced by

nanoparticles is still not completely clear, many studies showed that a nanoparticle-induced reactive oxygen species (ROS) and oxidant stress response may be the main mechanism that induces various biological effects. Low ROS level play a critical roles in maintaing normal physiological functions. However, high levels of.ROS might cause cell injury.[161-164].

4.5.4 Cellular uptake study

Fluorescence attachment

Amine-reactive derivatives of fluorescein dye, Fluorescein isothiocyanate (FITC), was used to attach a fluorescent label to nanoparticles via amine group of silk fibroin. FITC was dissolved in absolute ethanol at 1 mg/ml, added dropwise into nanoparticles solution and incubated overnight in dark. The unbound FITC was separated using centrifugation for three times (12000 rpm for 10 minutes). Nanoparticles were redispersed in 70% ethanol for sterilization overnight, then washed with 1×PBS using centrifugation for three times and finally dispersed in 1×PBS at stock concentration.

Fluorescence imaging

Method: Fibroblasts were cultured into 4-well chamber slides (IWAKI, Japan). After incubated with 100µg/ml FTIC attached SF nanoparticles for 30 minutes and 24 hours, cells were washed three times with 1×PBS and fixed with 1% formaldehyde for 0.5 hour. For filamentous actin and nucleus staining,

fibroblasts were rinsed with 1×PBS buffer, permeablized with 0.1% TritonX-100 for 15 minutes, stained with Phalloidin-TRITC (Sigma Aldrich P1951, red) and DAPI (Invitrogen D1306, blue) respectively. Fibroblasts were finally mounted onto glass slides (Shur/Mount™ - Water Based mounting media, Electron Microscopy Sciences) after the media chamber and gasket were removed. Stained fibroblasts were then observed using Fluorescent Microscope (Nikon, Eclipse 80i) with a Nikon 20×0.5 NA Plan Fluor objective.

Results and discussion: In general, the cellular uptake property of nanoparticles as a drug carrier influences its therapeutic efficiency. To investigate the cellular uptake property, SF nanoparticles, were labeled by green fluorescent fluorescein isothiocyanate (FITC). The cellular uptake of SF nanoparticles after incubated with HFF-1 fibroblasts was examined by fluorescence microscopy. The results showed that large amounts of nanoparticles attached onto the cell membranes and were internalized into the HFF-1 fibroblasts.

The incubation time is one of the factors that affect the accumulation of nanoparticles into a cell. Figure 4.8 shows the fluorescent images of HFF-1 fibroblasts incubated with 100 µg/ml FITC attached SF nanoparticles for 30 minutes. As shown in Figure 4.8, many SF nanoparticels were observed to adhere to the fibroblasts in a very short time. When incubation time increased to 24 hours, the fluorescent intensity shown in Figure 4.10 was enhanced. Therefore, the cellular uptake of silk fibrin nanoparticles by fibroblasts can be improved

with increase of incubation time from 30 minutes to 24 hours.

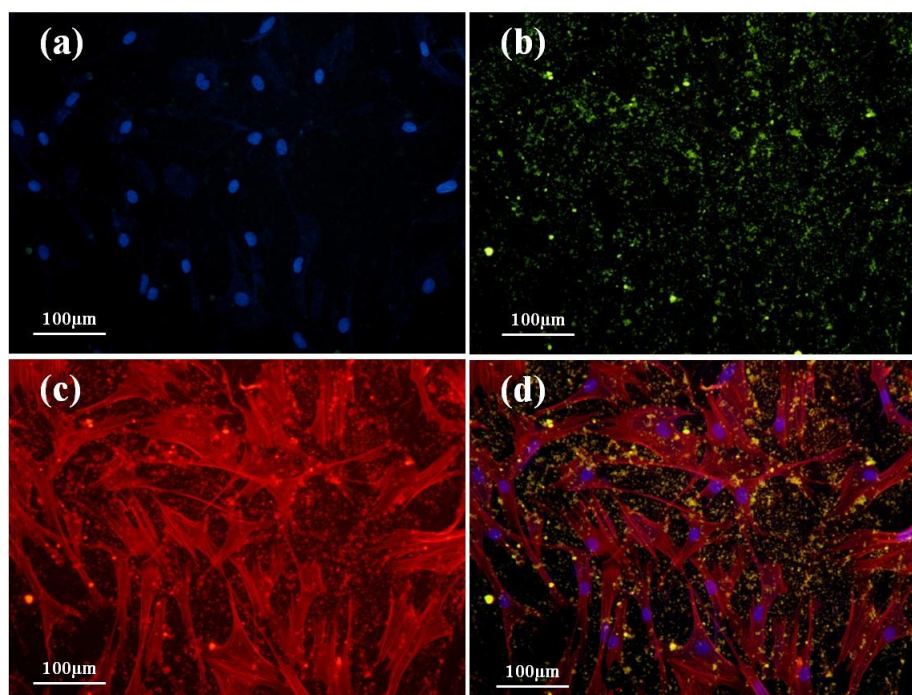


Figure 4.8 Fluorescence microscopy images of filamentous actin (red) and nucleus (blue) stained fibroblasts incubated with 100 µg/ml SF nanoparticles (green) for 0.5 hours (a) DAPI Channel, (b) FITC Channel, (c) TRITC Channel, (d) Merged Image

Figure 4.9, Figure 4.10 and Figure 4.11 shows the fluorescence images of cell endocytosis for silk fibroin nanoparticles at 10, 100 and 1000 µg/ml after 24 hours of incubation, respectively. Obviously, the cellular uptake of silk fibroin nanoparticles increased significantly with increase in concentration. Many SF nanoparticle clusters were observed for fibroblasts after incubation with 100 and 1000 µg/ml SF nanoparticles, especially for fibroblasts incubated with 1000 µg/ml SF nanoparticles, almost all the fibroblasts were fully covered by SF nanoparticles, this might result in inhibition of cell viability of fibroblasts.

In conclusion, the silk fibroin nanoparticles exhibited time-dependent and

concentration-dependent cellular uptake behaviors. With increase of incubation time and concentration, the cellular uptake of silk fibrin nanoparticles could be enhanced obviously. The efficient cellular uptake of silk fibroin nanoparticles indicated that it can be used as a potential drug carrier to deliver drugs to cells by cellular internalization.

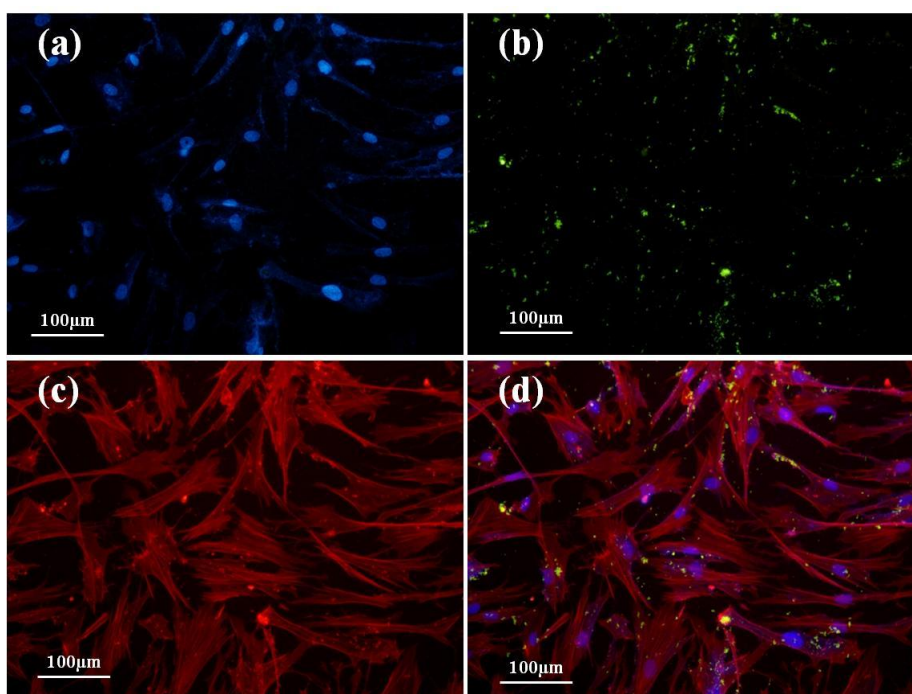


Figure 4.9 Fluorescence microscopy images of filamentous actin (red) and nucleus (blue) stained fibroblasts incubated with 10 µg/ml SF nanoparticles (green) for 24 hours (a) DAPI Channel, (b) FITC Channel, (c) TRITC Channel, (d) Merged Image

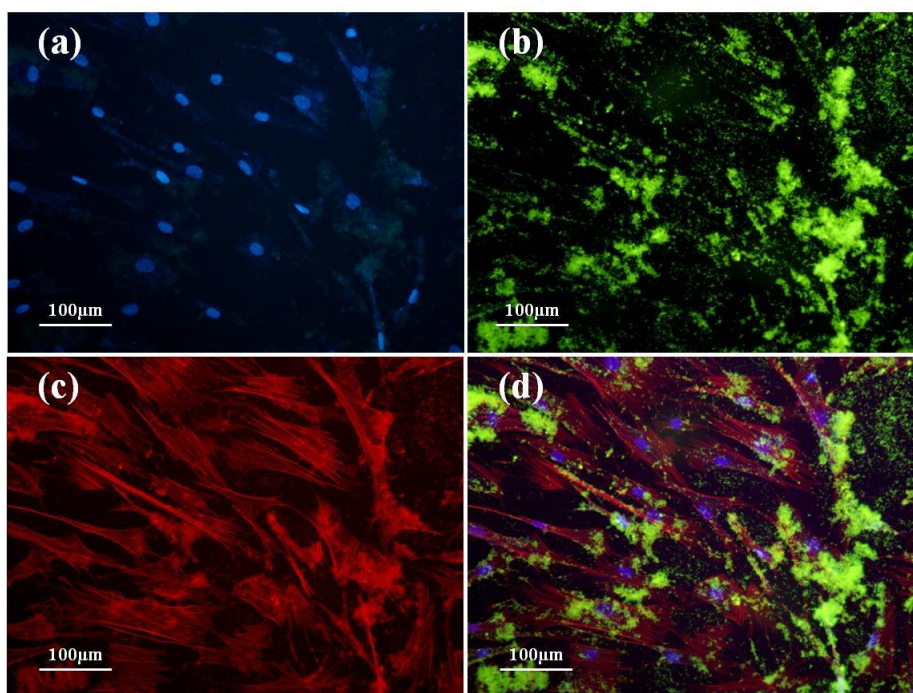


Figure 4.10 Fluorescence microscopy images of filamentous actin (red) and nucleus (blue) stained fibroblasts incubated with 100 µg/ml SF nanoparticles (green) for 24 hours (a) DAPI Channel, (b) FITC Channel, (c) TRITC Channel, (d) Merged Image

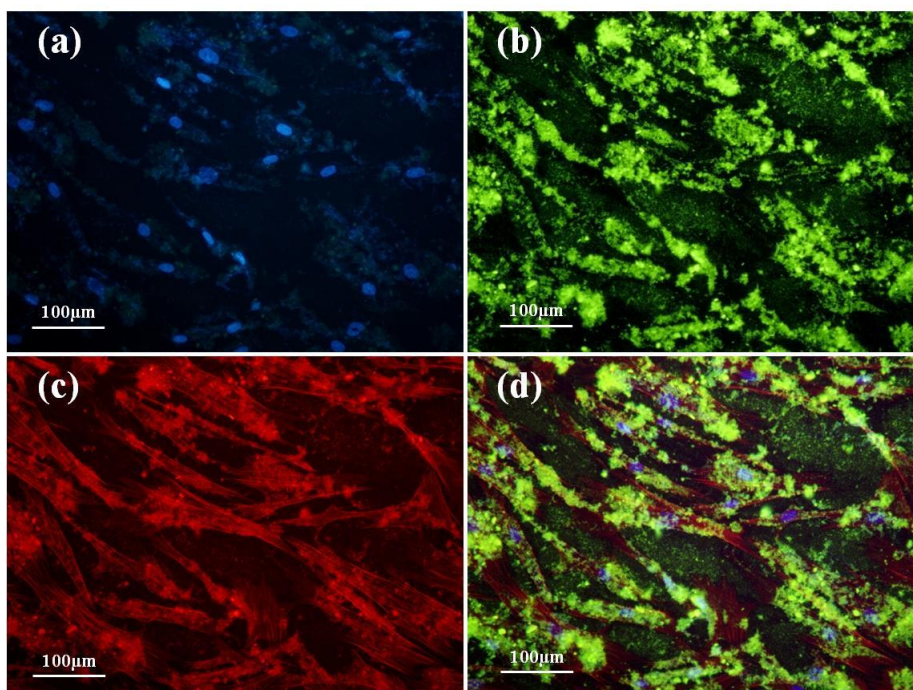


Figure 4.11 Fluorescence microscopy images of filamentous actin (red) and

nucleus (blue) stained fibroblasts incubated with 1000 µg/ml SF nanoparticles (green) for 24 hours (a) DAPI Channel, (b) FITC Channel, (c) TRITC Channel, (d) Merged Image

4.6 Drug loading and *in vitro* release properties

4.6.1 UV-Vis/HPLC assay for PTX

Method

The DL and EE of PTX-SF nanoparticles were analyzed by UV-Vis/HPLC (Waters 1100) system with the following conditions: stationary phase: reverse-phase column (4.6 mm × (Aligent Eclipse XDB-C18, 4.6 mm × 250 mm internal diameter, pore size 5 µm) ; mobile phase: mixture of acetonitrile and water (50:50 v/v) ; elution flow rate: 1 mL/min; detection wavelength: 227 nm. All the solvent and distilled water used for aqueous solutions and buffer should be filtered via a 0.22 µm membrane filter before use. The content of PTX in the samples was measured based on the peak area at the retention time. A calibration curve of standard PTX dissolving in mixture of acetonitrile and water (50:50 v/v) was utilized to calculate the content of PTX in the samples. All the samples were conducted in triplicate.

Results and discussion

Figure 4.12 suggests that the chromatogram for standard solutions of PTX in the mixture of acetonitrile and water (50:50 v/v). Obviously, the retention time of PTX under the operating conditions and mobile phase is about 13.3 minutes. Figure 4.13 shows calibration curve of PTX by HPLC analysis. According to this figure, the standard curves were linear over a concentration range of 16~100000 ng/ml, with a correlation coefficient of $R^2=0.999978$. The equation can be expressed as: $Y=4.13e+004x-5.02e+003$

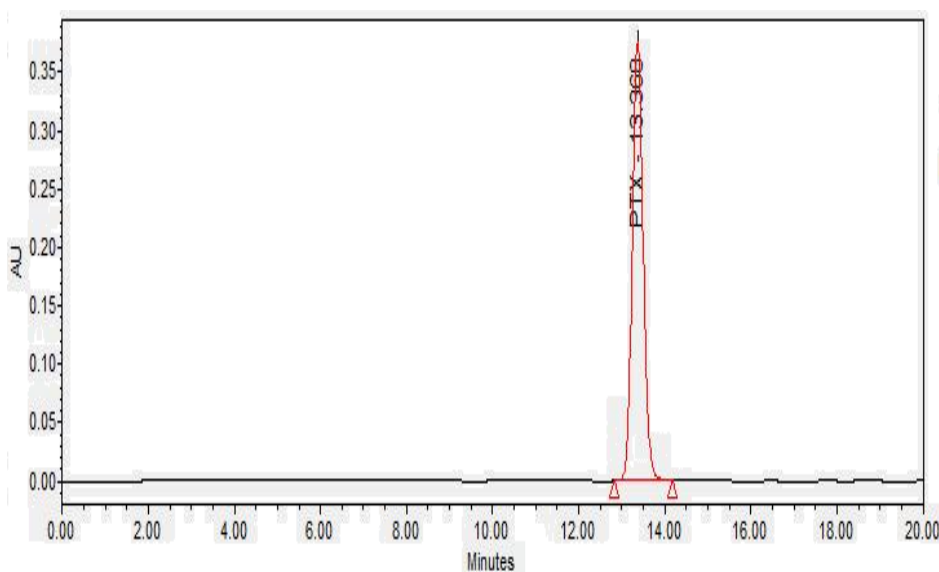


Figure 4.12 Chromatogram for standard solutions of PTX in acetonitrile/water
(50:50 v/v)

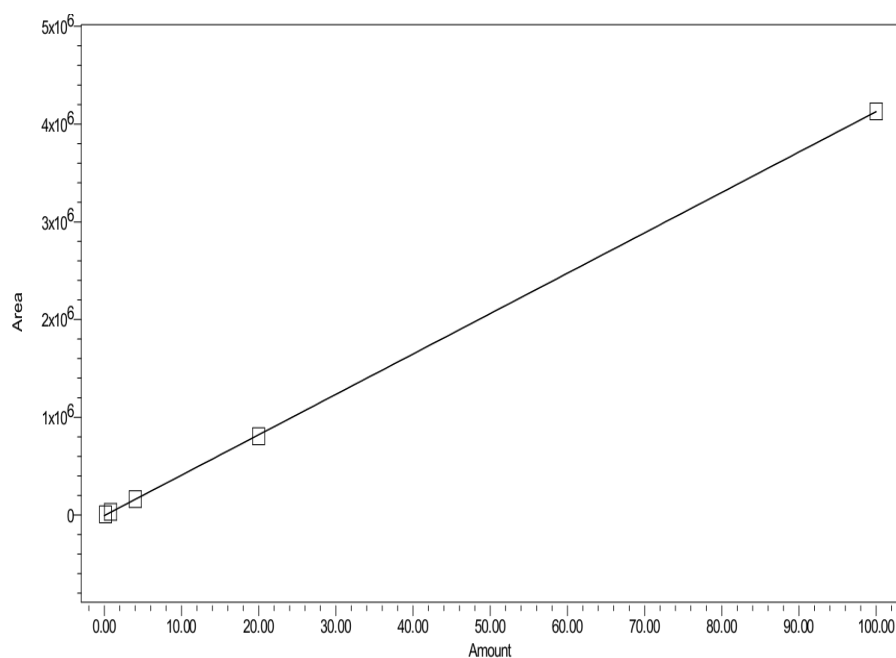


Figure 4.13 Calibration curve of PTX determined by UV-Vis/HPLC analysis

4.6.2 UV-vis spectrophotometer analysis for IDMC

Method

The amount of indomethacin (IDMC) was measured by UV spectrophotometer (Lambda 18 spectrometer of Perkin Elmer, USA) at 321 nm, according to the standard curve of indomethacin.

Results and discussion

By UV-spectrophotometric analysis at 321nm, the calibration curve of IDMC shown in Figure 4.14 has been obtained. According to this figure, the standard curves were linear over a concentration range of 5~35 µg/ml, with a correlation coefficient of $R^2=0.99979$. The equation can be expressed as: $Y=52.77106x-0.15786$.

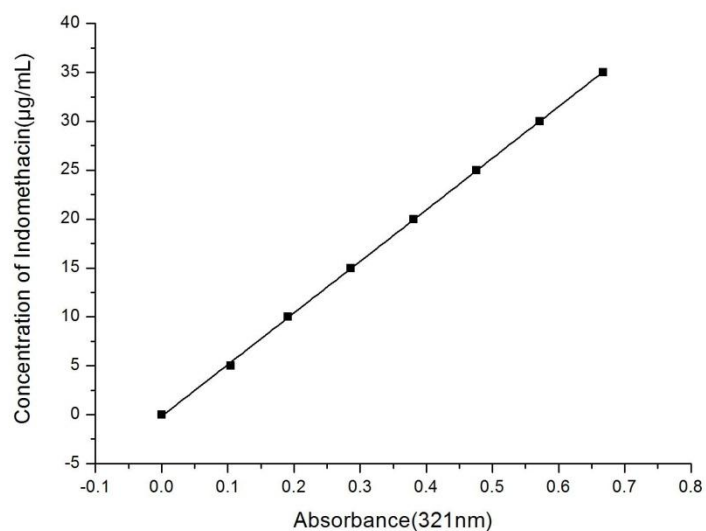


Figure 4.14 Calibration curve of IDMC determined by UV-spectrophotometric analysis

4.6.3 Drug load (DL) and encapsulation efficiency (EE)

Method

The actual content of paclitaxel (PTX) in PTX-SF nanoparticles can be determined by dissolving untreated PTX loaded SF nanoparticles (3.0 mg accurately weighed) in 1 mL of ddH₂O, and then adding 1 mL of an acetonitrile to form the mixture of acetonitrile/water (50:50 v/v). After being completely mixed, the solution was put into a vial for UV-Vis/HPLC assay according to calibration curve. The actual content of the PTX encapsulated in PTX-SF nanoparticles after ethanol treatment was calculated by subtracting the content of drug that leaked into the supernatant from that of untreated PTX-SF nanoparticles. The content of the PTX was measured by UV-Vis/HPLC assay.

The actual content of indomethacin (IDMC) encapsulated in the IDMC-SF nanoparticles was measured by dissolving 10 mg of the IDMC-SF nanoparticles in 100 ml of PBS of pH 7.4. The actual content of the IDMC encapsulated in the IDMC-SF nanoparticles after ethanol treatment nanoparticles was calculated by subtracting the content of drug that leaked into the supernatant from that of untreated IDMC-SF nanoparticles. The content of the IDMC was measured by UV spectrophotometer at 321 nm.

The theoretical drug content, the actual drug load, and encapsulation efficiency were calculated by equations (1), (2), and (3), respectively.

$$\text{Theoretical drug load} = W1/W3 * 100 \% \quad (1)$$

$$\text{Actual drug load} = W2/W3 * 100 \% \quad (2)$$

$$\text{Encapsulation efficiency} = W2/W4 * 100\% \quad (3)$$

W1 is the weight of theoretical IDMC or PTX in the IDMC-SF or PTX-SF nanoparticles; W2 is the weight of the actual IDMC or PTX encapsulated in the IDMC-SF or PTX-SF nanoparticles; W3 is the gross weight of the IDMC-SF or PTX-SF nanoparticles; and W4 is the weight of IDMC or PTX used in the procedure. According to the standard curves of PTX and IDMC, DL and EE can be obtained.

Results and discussion

DL and EE are two kinds of effective parameters to determine the drug

loading property of drug carrier. In order to investigate the suitability of SF nanoparticles as a drug carrier, paclitaxel (PTX), a commonly used anti-cancer drug, has been chosen as drug model. PTX-loaded SF nanoparticles were prepared by co-precipitation of PTX and SF using the SEDS process. HPLC analysis indicated that for almost all the PTX has been loaded in the SF nanoparticles and the drug load and encapsulation efficiency (EE) of PTX-SF nanoparticles is about 19.86% and 99.32% (shown in Table 4.1), which is similar to the theoretical drug load of 20% and EE of 100%. However, after water insolubility induction via ethanol treatment, almost all PTX have been lost. The corresponding DL and EE has increased to 0.62% and 3.14% respectively after ethanol treatment. The results may be caused by high solubility of PTX in ethanol. And the sonication in the process of ethanol treatment can also accelerate the drug leakage.

Table 4.1 Drug load (DL) and encapsulation efficiency (EE) of PTX-SF and IDMC-SF nanoparticles before and after ethanol treatment

	DL and EE	Drug	
		Paclitaxel (PTX)	Indomethacin (IDMC)
Before ethanol treatment	DL	19.86%	6.11%
	EE	99.32%	30.52%
After ethanol treatment	DL	0.62%	2.05%
	EE	3.14%	10.23%

In terms of almost all PTX loss in the induction of water insolubility of silk fibroin nanoparticles, indomethacin (IDMC), a non-steroidal anti-inflammatory drug, was chosen as another model drug to study the drug loading and *in vitro* drug release property of SF nanoparticles. The results indicated that IDMC-SF nanoparticles with a theoretical drug load of 20%, actual drug load of 6.11%, and encapsulation efficiency (EE) of 30.52% are obtained successfully (shown in Table 4.1). These figures are higher than the 2.8% actual drug load and 14% encapsulation efficiency reported by Kang *et al* in a study of indomethacin-loaded PLLA/PLGA microparticles fabricated by a supercritical CO₂ technology [125]. After ethanol treatment, drug loss also occurred and the actual drug load and encapsulation efficiency decreased to 2.05% and 10.23%, respectively. A similar phenomenon in which methanol treatment result in a significant loss of salicylic acid from silk fibroin particles through leaching has been reported by Wenk *et al* [12]. The higher actual DL and EE in this study indicate that IDMC has a better compatibility with silk fibroin than with the PLLA/PLGA polymer, and that the SEDS process is an effective method to prepare IDMC-SF nanoparticles as a drug delivery system.

4.6.4 *In vitro* drug release

Method

Approximately 2 mg of IDMC-SF nanoparticles was put into the pretreated dialysis bag, then the bag was placed into a bottle with 100 ml of PBS

(pH 7.4) and incubated in a water-bath shaker at 37 °C and 60 rpm. Ten milliliters of solution was periodically removed and replaced by fresh PBS (pH 7.4). The released drug was analyzed using a UV spectrophotometer at 321 nm. As a control, an *in vitro* drug release experiment using free drug (of equivalent weight to that in the drug loaded nanoparticles) was performed in similar conditions. The *in vitro* drug release curves were drawn based on the cumulative release percentage of indomethacin (% , w/w) in PBS solution over long periods of time.

Results and discussion

IDMC is a poorly water-soluble drug, and its solubility in 0.1 M PBS (pH 7.4) is above 0.75 mg/ml at 37 °C [165, 166]. The experimental conditions ensured that all of the IDMC could be dissolved in 100 ml of PBS. Figure 4.15 shows the *in vitro* release profile of IDMC from IDMC-SF nanoparticles obtained by the SEDS process in PBS at pH 7.4. It can be seen that nearly all of the free IDMC (94.4%) was released in 6 h. After encapsulation by SF, the accumulative release of IDMC from IDMC-SF nanoparticles decreased to 61.15% in 6 h and reached 87% in 24 h. The release of IDMC then reached a plateau. In the next 24 h, about 5% of the drug was released. Obviously, IDMC-SF nanoparticles exhibited a controlled IDMC release property. Normally, Controlled drug release of polymer nanoparticles may be attributed to polymer erosion and drug diffusion [103]. Due to the slow degradability of the silk fibroin

protein in the body and small molecular weight of IDMC, the drug release may be mainly controlled by drug diffusion from IDMC-SF nanoparticles. Furthermore, the strong hydrophobic interaction between the IDMC molecules and the water-insoluble SF nanoparticles may also sustain the IDMC release. It is demonstrated that silk fibroin can be used effectively as a drug carrier and that the SEDS process is a feasible way to prepare the controlled-release nanoparticles.

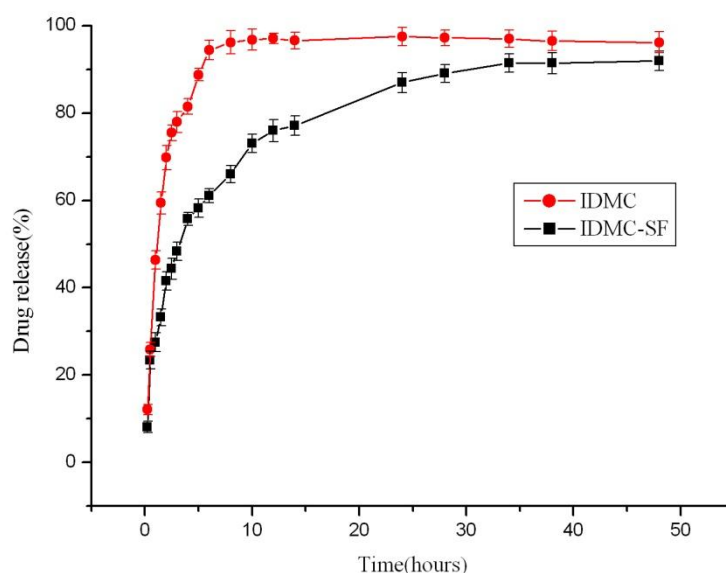


Figure 4.15 Drug release curves of IDMC from IDMC-SF nanoparticles obtained by the SEDS process (Each point represents the mean \pm standard deviation obtained from triplicates of the samples)

4.7 Summary

In this Chapter, silk fibroin nanoparticles, around 50 nm in a mean particle size, were successfully fabricated using the SEDS process. Ethanol was

found to be useful for induction of the water insolubility of SF nanoparticles by the conformation shift of the SF nanoparticles from random coil to β -sheet structure shown by the XRPD, TG-DSC, and FTIR analysis of the nanoparticles. Moreover, the relative non-toxicity of SF nanoparticles shown by MTS and LDH assay indicated excellent biocompatibility. Cellular uptake studies using fluorescence microscopy observation indicated that the silk fibroin nanoparticles possessed time and concentration-dependent cellular uptake ability and could be internalized into HFF-1 fibroblast effectively. PTX can be loaded to silk fibroin nanoparticles. However, induction of water insolubility by ethanol resulted in all PTX loss. The silk fibroin nanoparticles containing indomethacin showed a sustained release *in vitro* over two days without a burst effect. Furthermore, owing to possessing many active amino groups, the silk fibroin could be modified by active substances to obtain desirable characteristics [38]. In summary, this study suggests that the silk fibroin nanoparticles prepared using the SEDS process could be utilized as a biocompatible carrier to deliver drugs. Also, the SEDS process is an effective method to fabricate drug-loaded polymer nanoparticles delivery systems for controlled drug release.

Chapter 5 Development of silk fibroin modified PLLA-PEG-PLLA (SF/PPP) nanoparticles in supercritical CO₂

5.1 Introduction

In the previous Chapter 3 and 4, silk fibroin nanoparticles have been described as being fabricated by the SEDS process successfully. Moreover, the results of characterization of the physical and chemical properties show that silk fibroin nanoparticles by the SEDS process possess a spherical shape with small particle size, suitable chemical property and excellent biocompatibility. However, the application of silk fibroin nanoparticles as drug carrier could be limited by drug loss resulting from water-insolubility treatment for silk fibroin nanoparticles. In order to overcome the disadvantages of silk fibroin nanoparticles as drug carrier, Chapter 5 aims to prepare silk fibroin/PLLA-PEG-PLLA (SF/PPP) nanoparticles in order to achieve the objective 4 shown in Section 1.2 of Chapter 1 by supercritical CO₂ technology.

In this Chapter, in order to fabricate the SF/PPP nanoparticles successfully, two kinds of SEDS process had been employed in the Chapter, The resulting SF/PPP nanoparticles were characterized by scanning electron microscopy (SEM), TEM, Laser diffraction particle size analyzer, thermogravimeter-differential scanning calorimeter (TG-DSC) and FTIR analysis. Besides, the biocompatibility of SF/PPP nanoparticles were performed by *in vitro* cytotoxicity studies such as

MTS assay and LDH assay. Finally, fluorescence observation and flow cytometric analysis were also used to investigate the cellular uptake behaviors.

5.2 Preparation of SF/PPP composite nanoparticles by the SEDS process

5.2.1 Method 1: Co-precipitation of SF/PPP from a homogeneous solution

Briefly, the silk fibroin and PLLA-PEG-PLLA (MW 100kDa, PEG 10%, Department of Medical Polymer Shandong Institute, Jinan, China) were dissolved in HFIP solution, and the concentration of SF/PPP in HFIP solution was 0.5 % (w/v), then the resulting solution was sprayed into high pressure vessel via a coaxial nozzle. The SEDS process has been given in Section 3.2.3 of Chapter 3. The experimental conditions can be described as follows: (P: 20 MPa, T: 35 °C; the flow rates of scCO₂ and solution were 25NL · h⁻¹ and 0.5 ml min⁻¹, respectively).

In order to study the effect of the SEDS process on micronization of different materials, PPP nanoparticles were prepared by the SEDS process under the same operating conditions. Shortly, 0.5 % (w/v) PPP was dissolved in HFIP solution, and then the resulting PPP solution was delivered into the high pressure vessel.

5.2.2 Method 2: Precipitation of SF/PPP from a suspended solution

Silk fibroin (SF) nanoparticles can be prepared according to the method given in Section 3.2.3 of Chapter 3. For the preparation of SF/PPP nanoparticles, a modified SEDS process has been employed by introducing a particle suspension delivery system. Briefly, the silk fibroin nanoparticles prepared by the SEDS process were firstly immersed into ethanol to induce water insolubility and then the resulting water insoluble silk fibroin nanoparticles were dispersed into PPP solution in dichloromethane (DCM, Advanced Technology & Industrial Co. Ltd. Hong Kong) using ultrasonic method for further experiment. The ratio of SF nanoparticles to PPP was 1:4 and the final concentration of SF/PPP solution was 0.5% (w/v).

Figure 5.1 shows a schematic diagram of the modified SEDS instrument for preparation of silk fibroin/PPP composite nanoparticles, which is made up of three main parts: a CO₂ supply system, a particle suspension delivery system and a high pressure vessel with a volume of 1000 ml. An ‘injector’ with two containers separated by a piston was acted as the particle suspension delivery system [167]. Using the SEDS process, when the desired experimental conditions were reached, the PPP solution containing silk fibroin nanoparticles was atomized via a stainless steel coaxial nozzle (inner diameter (ID) 0.80 mm, and the nozzle of suspension with ID 0.33 mm and length 12.35 mm) into the high pressure vessel. The experimental conditions can be described as follows:

(P: 20 MPa, T: 35 °C; the flow rates of scCO₂ and solution were 25NL · h⁻¹ and 0.5 ml min⁻¹, respectively).

In order to study the effect of the SEDS process involving in particle suspension delivery system on micronization of different materials, PPP nanoparticles were prepared by the SEDS process under the same operating conditions above. In short, 0.5% (w/v) PPP was dissolved in DCM solution, and then the resulting PPP solution was delivered into the high pressure vessel. The operating conditions were described above.

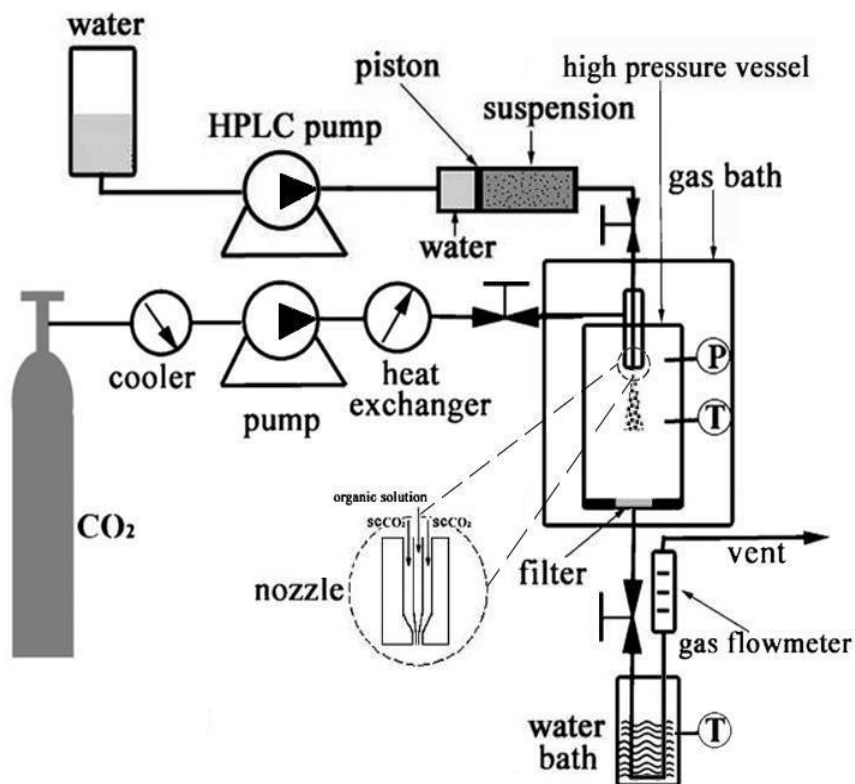


Figure 5.1 Schematic diagram of the SEDS apparatus for preparation of silk fibroin/PPP composite particle

5.3 Surface morphology and particle size distribution

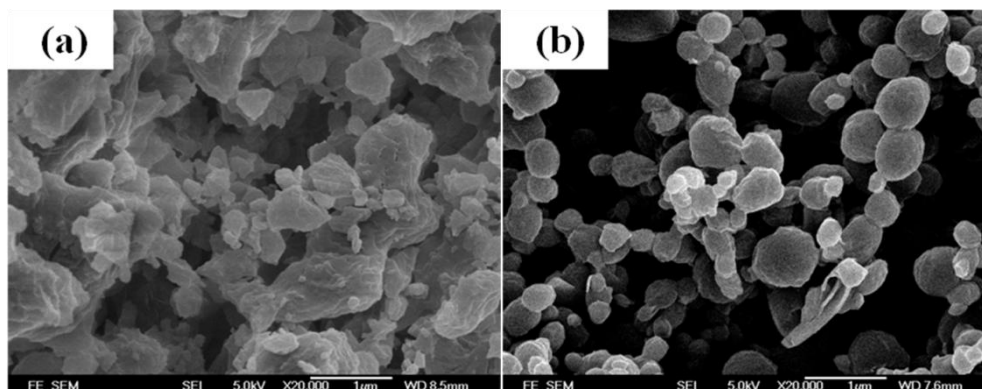


Figure 5.2 FE-SEM photographs of samples obtained by method 1 (a) SF/PPP composite samples and (b) PPP nanoparticles

The methods about characterizing surface morphology and particle size distribution have been described in Section 3.2.5. Figure 5.2 (a) and (b) show the surface morphology of silk fibroin/PPP composite samples and PPP nanoparticles obtained by **Method 1** under similar experimental conditions. From Figure 5.2 (b), it can be seen that PPP nanoparticles exhibit a good spherical shape, a smooth surface, and a narrow particle size distribution. However, after combining with silk fibroin, the resulting SF/PPP hybrids obtained by the SEDS process exhibit an irregular shape. Nearly no spherical particles formed. The size of SF/PPP hybrids is also bigger than the PPP nanoparticles obviously. The irregular products of SF/PPP hybrids may result from the different precipitation kinetics of the SF and PPP polymer in the coprecipitation process.

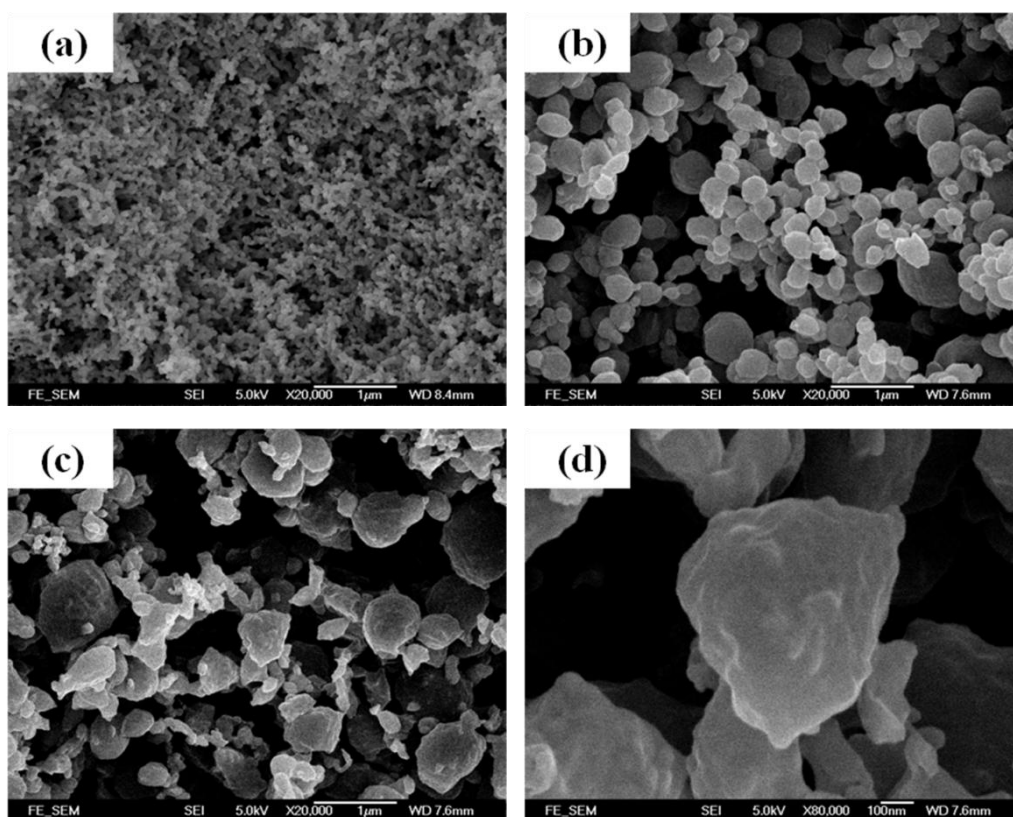


Figure 5.3 SEM photographs of samples obtained by method 2 (a) SF nanoparticles, (b) PPP nanoparticles, (c) and (d) SF/PPP nanoparticles

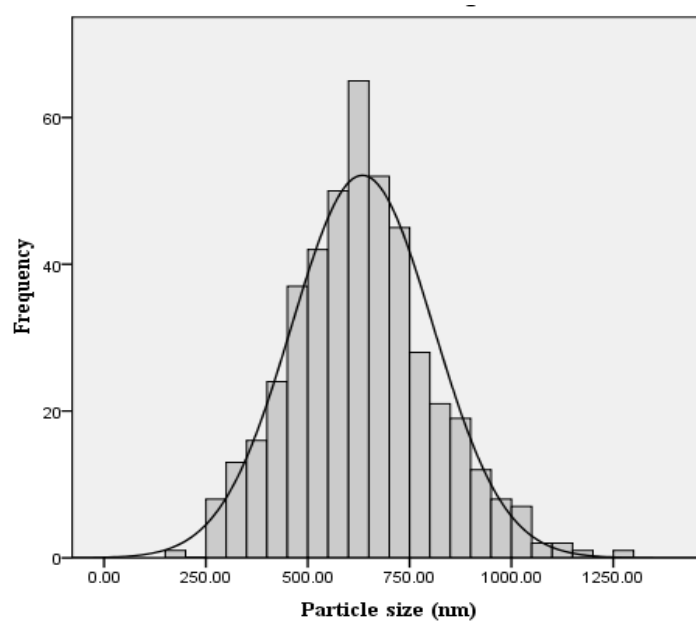


Figure 5.4 Particle size distribution of SF/PPP nanoparticles

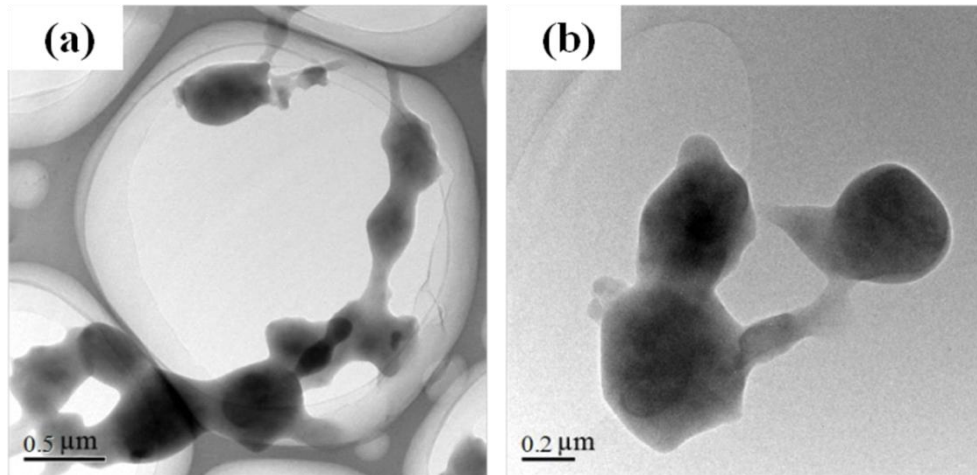


Figure 5.5 TEM photographs of SF/PPP nanoparticles

Figure 5.3 (a), (b), (c) and (d) show the surface morphology of the silk fibroin nanoparticle, PPP microparticles and SF/PPP composite nanoparticles prepared by method 2 respectively. Obviously, SF/PPP composite nanoparticles were successfully fabricated. Compared to SF/PPP hybrids prepared by method 1, SF/PPP composite nanoparticles fabricated by method 2 possess a good spherical shape. It can be concluded that method 2 is an effective way to prepare the silk fibroin/PPP composite nanoparticles. However, the SF/PPP composite nanoparticles possess a rough surface. Figure 5.4 shows the particle size distribution of SF/PPP nanoparticles prepared by the SEDS process. From this figure, it can be seen that the mean particle size is about 634.1 ± 173.7 nm and particle size distribution is 0.713.

In terms of smooth surface of PPP nanoparticles obtained by similar experimental conditions, it can be concluded that the rough surface of SF/PPP composite nanoparticles results from adding silk fibroin nanoparticles. The similar size of rough part to that of silk fibroin nanoparticles used in the

experiment indicated that the rough parts may be silk fibroin nanoparticles. This result has been improved by TEM photos of SF/PPP nanoparticles (shown in Figure 5.3), which show that silk fibroin nanoparticles have been dispersed in the PPP microparticles. Therefore, the SF/PPP composite microparticles possess a core-shell structure with silk fibroin nanoparticles dispersed on the PPP nanoparticles.

Considering the successful fabrication of silk fibroin/PPP composite nanoparticles **Method 2** will be used to prepare the silk fibroin/PPP composite nanoparticles for further characterization.

5.4 Chemical and physical properties

FTIR and XRPD analysis have been used to characterize the chemical and physical properties of SF, PPP and SF/PPP nanoparticles. Their corresponding methods have been described in Section 4.4 of Chapter 4.

5.4.1 FTIR analysis

Fourier Transform Infrared Spectroscopy (FTIR) is one of the most widely used methods to identify the chemical structure of a molecule by producing an infrared absorption spectrum, especially that of silk fibroin molecule [38]. Figure 5.6 shows the FTIR spectras of original PPP, SF nanoparticles, and SF/PPP nanoparticles. The characteristic peak of amide I at 1627 cm^{-1} and amide II at 1521 cm^{-1} is assigned to the β -sheet of silk fibroin. And the characteristic peaks

at 1092 cm^{-1} correspond to $\nu\text{C-O-C}$ of the PLLA-PEG-PLLA polymer. As shown in the spectra of SF/PLLA-PEG-PLLA, the characteristic peak of amide II at 1627 cm^{-1} of silk fibroin has shifted to 1658 cm^{-1} , which is attributed to α -helix or random coil conformation. The results suggest that a minor transformation from β -sheet conformation to α -helix or random coil conformation of silk fibroin occurs. Maybe the blending of silk fibroin and PLLA-PEG-PLLA affects the secondary structure of silk fibroin. However, the major characteristic peaks including characteristic peaks at 1520 cm^{-1} and 1092 cm^{-1} had no obvious change.

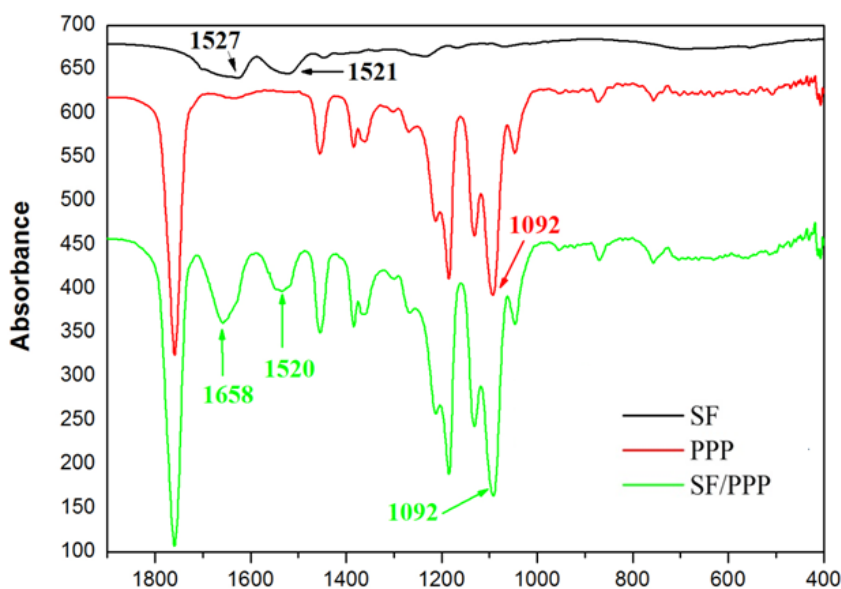


Figure 5.6 FTIR spectras of original PPP, SF nanoparticles, and SF/PPP nanoparticles in the supercritical process

5.4.2 XRPD analysis

X-ray powder diffractometry (XRPD) is an important technique to investigate the crystal phase of samples. Figure 5.7 shows the diffraction patterns

of crystalline PPP, SF nanoparticles, and SF/PPP nanoparticles, respectively. On the XRPD curves, a broad peak at $2\theta = 20.4^\circ$ is attributed to silk I of SF before the SEDS process. The characteristic diffraction peaks at $2\theta = 12.5^\circ, 14.7^\circ, 16.6^\circ, 22.3^\circ$ are attributed to the PLLA block, and the peaks of 18.9° and 23.2° are attributed to the PEG block. It indicates the existence of a natural crystalline form of PPP copolymer. After the SEDS process, the characteristic peaks of the PPP copolymer became significantly weak. The SEDS process led to the shifting of the physical form of PPP copolymer from crystalline to amorphous. Besides, no obvious characteristic peaks of SF have been found in the XRPD curve of SF/PPP nanoparticles, which could result from the superposition of the broad characteristic peaks of SF at $2\theta = 20.4^\circ$ and the peaks of PEG block at $2\theta = 18.9^\circ$. These results also supported that of FTIR analysis.

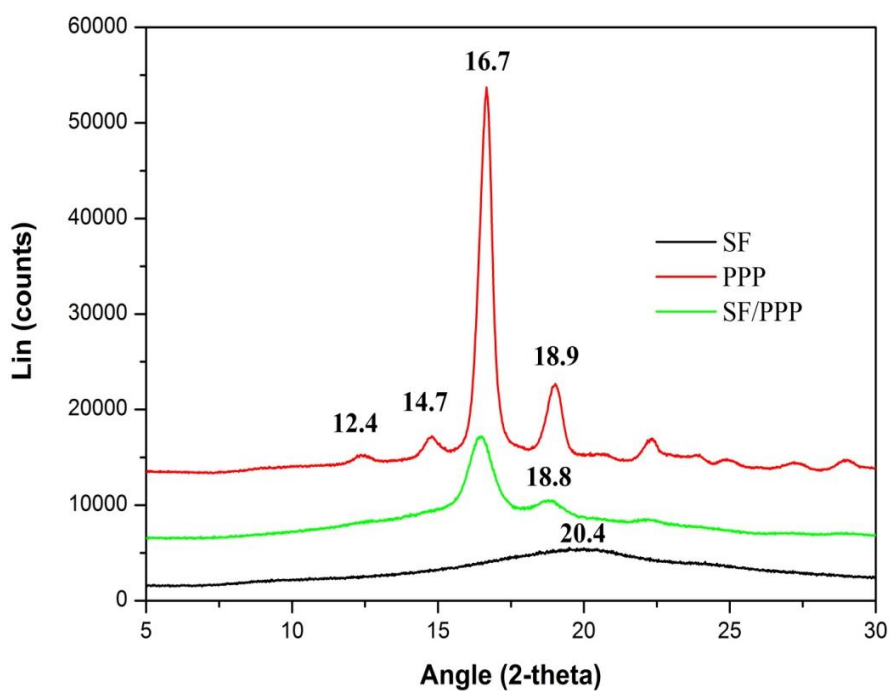


Figure 5.7 XRPD patterns of original PPP, SF nanoparticles, and SF/PPP nanoparticles in the supercritical process

5.5 Biological evaluation of SF/PPP nanoparticles

For biological evaluation of SF/PPP nanoparticles, MTS and LDH assay shown in Section 4.5 of Chapter 4 were used to examine the biocompatibility. Besides, fluorescence microscopy observation described in Section 4.2.6 of Chapter 4 and flow cytometric analysis were employed to study the cellular uptake behavior of SF/PPP nanoparticles.

5.5.1 MTS assay

The cell cytotoxicity of fibroblasts after incubation with different concentrations of PPP nanoparticles and SF/PPP nanoparticles at 10 $\mu\text{g/ml}$, 100 $\mu\text{g/ml}$ and 1000 $\mu\text{g/ml}$ was assessed using a MTS mitochondrial activity assay. The results are shown in Figure 5.8 and all the data were normalized to the cell metabolic activity of fibroblasts without nanoparticle incubation for one day. The cell metabolic activity is directly related to cell viability and the number of live cells.

Figure 5.9 shows that, after one day of incubation, compared with the control group, the viability of fibroblasts displayed no obvious change with 10 $\mu\text{g/ml}$ PPP nanoparticles and 10 $\mu\text{g/ml}$ SF/PP nanoparticles. With the concentration of nanoparticles increased to 100 $\mu\text{g/ml}$, the viability of fibroblasts incubated with SF/PPP nanoparticles is obviously higher than that of PPP nanoparticles. After 3 days of incubation, the biocompatibility of PPP nanoparticles was comparable to that of the control. However, a significant

increase was only observed for the viability of fibroblasts incubated with 1000 $\mu\text{g/ml}$ SF/PPP nanoparticles.

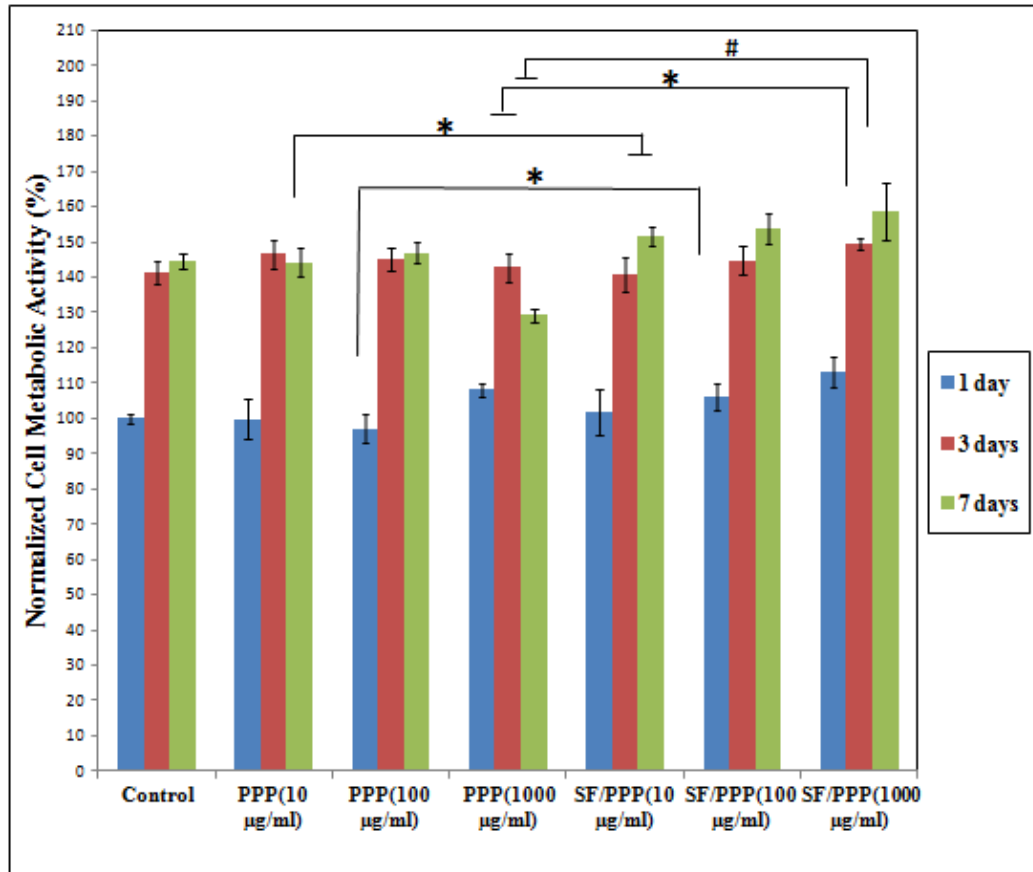


Figure 5.8 Cell proliferation of fibroblasts incubated with PPP nanoparticles and SF/PPP composite nanoparticles for 1 day, 3 days and 7 days measured with a

MTS cell proliferation assay.p-values: # < 0.01; * < 0.05

After 7 days of incubation, compared with the control, a significant decrease in the viability of fibroblasts incubated with 1000 $\mu\text{g/ml}$ PPP nanoparticles was observed. However, SF/PPP nanoparticles significantly increased the cell viability of fibroblasts compared to PPP nanoparticles at 10 $\mu\text{g/ml}$ and 1000 $\mu\text{g/ml}$. These results indicated that SF/PPP nanoparticles showed better biocompatibility than PPP nanoparticles. It can be concluded that adding silk

fibroin into PPP can improve the biocompatibility of the PPP polymer. In fact, many studies have demonstrated silk fibroin possessed excellent biocompatibility and also can improve biocompatibility of hydroxyapatite and synthetic polymer such as PLLA and PCL [168-170]

5.5.2 LDH assay

The cell proliferation of fibroblasts after incubation with different concentrations of PPP nanoparticles and SF/PPP nanoparticles at 10 $\mu\text{g/ml}$, 100 $\mu\text{g/ml}$ and 1000 $\mu\text{g/ml}$ for 1 day, 3 days and 7 days was evaluated using LDH assay. The results are shown in Figure 5.9.

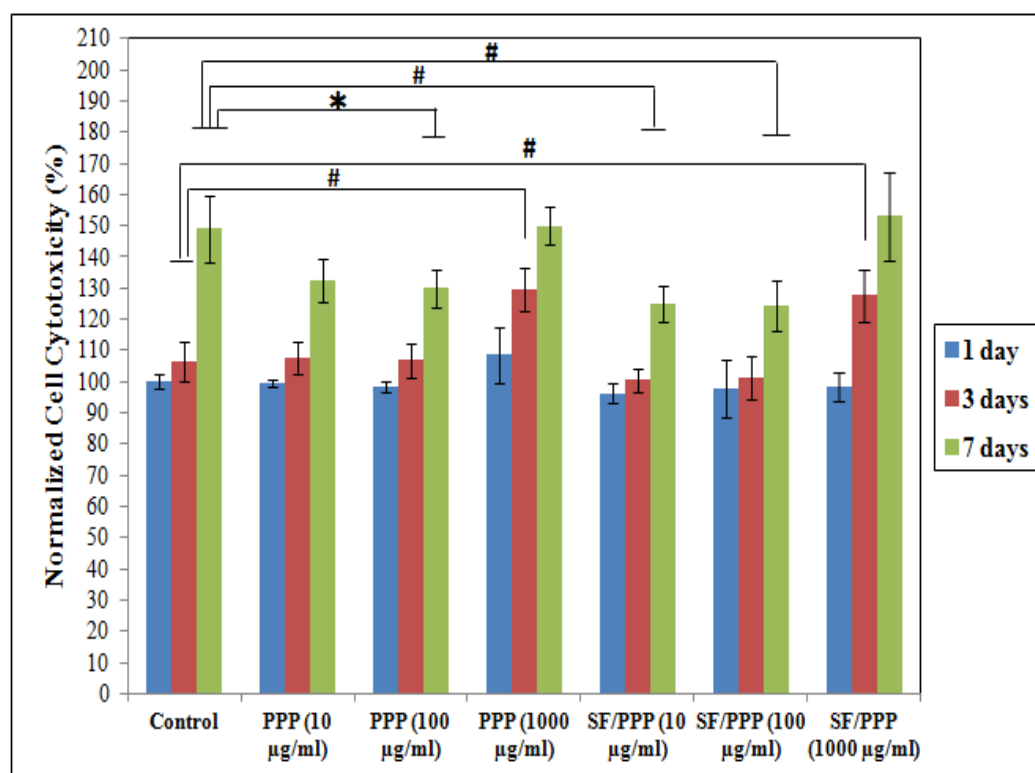


Figure 5.9 Cell proliferation of fibroblasts incubated with SF nanoparticles for 1 day, 3 days and 7 days measured with LDH assay. p-values: # < 0.01; * < 0.05

After 1 day of incubation, compared to the control, PPP nanoparticles and SF/PPP nanoparticles showed no obvious cytotoxicity to fibroblasts. PPP nanoparticles at high concentration (1000 $\mu\text{g/ml}$) exhibited a higher toxicity than SF/PPP nanoparticles slightly. However, there was no significant difference in cytotoxicity to fibroblasts between SF/PPP nanoparticles and PPP nanoparticles.

After 3 days of incubation, PPP nanoparticles and SF/PPP nanoparticles at low concentration (10, 100 $\mu\text{g/ml}$) exhibited no obvious cytotoxicity to fibroblasts. However, the cytotoxicity of SF/PPP nanoparticles was lower than that of PPP nanoparticles slightly. With the concentration of nanoparticles increased to 1000 $\mu\text{g/ml}$, PPP nanoparticles and SF/PPP nanoparticles showed higher cytotoxicity to fibroblasts than the control group significantly.

After 7 days of incubation, PPP nanoparticles at 100 $\mu\text{g/ml}$ and SF/PPP nanoparticles at 10 $\mu\text{g/ml}$ and 100 $\mu\text{g/ml}$ showed lower cytotoxicity than the control significantly. With the concentration of nanoparticles increased to 100 $\mu\text{g/ml}$, the cytotoxicity of PPP and SF/PPP nanoparticles was comparable to that of the control. However, cytotoxicity of SF/PPP nanoparticles at low concentration (10, 100 $\mu\text{g/ml}$) was lower slightly than that of PPP nanoparticles.

In a word, SF/PPP nanoparticles and PPP nanoparticles possessed excellent biocompatibility to fibroblasts. And adding SF into PPP nanoparticles can improve the biocompatibility of PPP slightly. However, there was no significant difference in cytotoxicity to fibroblasts between SF/PPP nanoparticles and PPP nanoparticles.

5.5.3 Cellular uptake of SF/PPP nanoparticles

Fluorescence microscopy

The cellular uptake efficiency of nanoparticles as drug carrier affects its therapeutic properties. To study the cellular uptake of SF/PPP nanoparticles, it was labeled by introducing green fluorescent Fluorescein isothiocyanate (FITC) onto SF/PPP nanoparticles. Figure 5.10 and Figure 5.11 show the fluorescence microscopy images of HFF-1 fibroblasts incubated with 100 $\mu\text{g/ml}$ FITC attached SF/PPP nanoparticles for 30 minutes and 24 hours respectively.

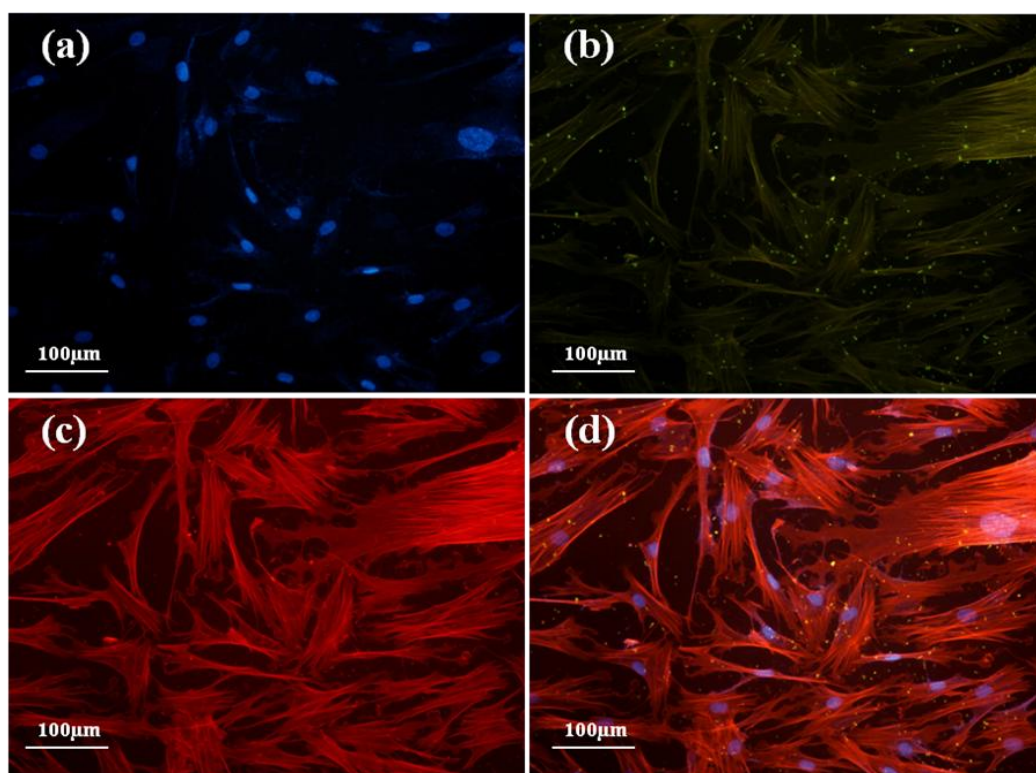


Figure 5.10 Fluorescence microscopy images of filamentous actin (red) and nucleus (blue) stained fibroblasts incubated with 100 $\mu\text{g/ml}$ SF/PPP nanoparticles (green) for 30 minutes (a) DAPI Channel, (b) FITC Channel, (c) TRITC Channel, (d) Merged Image

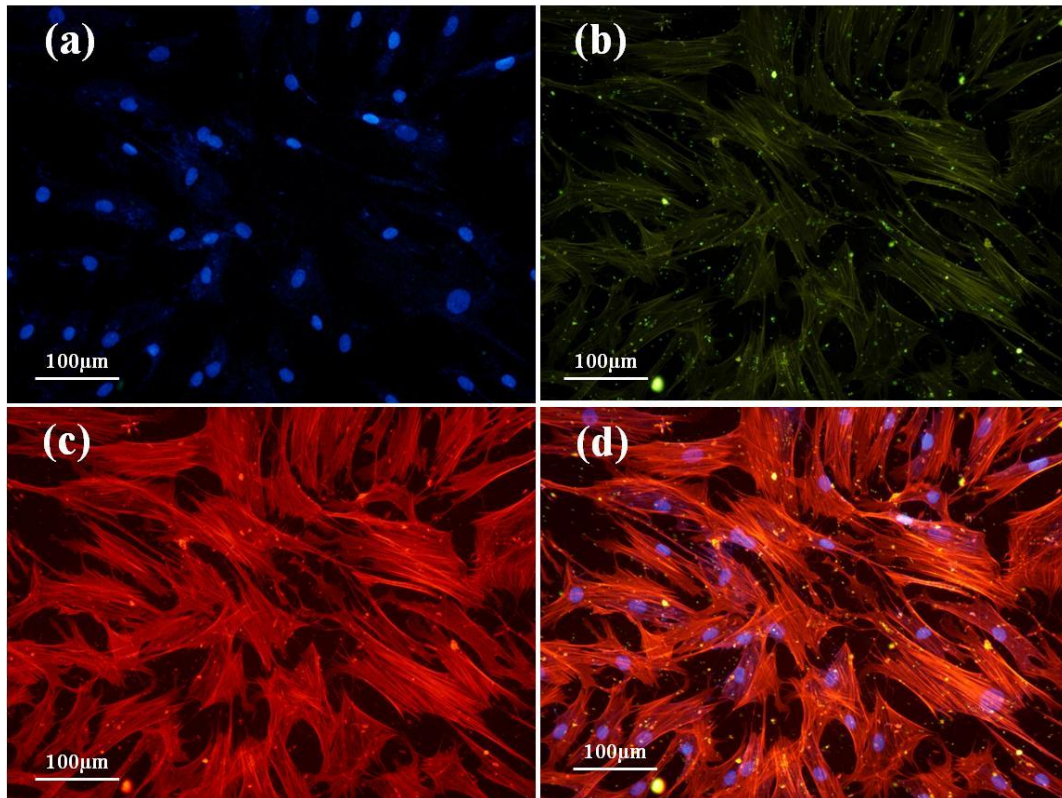


Figure 5.11 Fluorescence microscopy images of filamentous actin (red) and nucleus (blue) stained fibroblasts incubated with 100 µg/ml SF/PPP nanoparticles (green) for 24 hours (a) DAPI Channel, (b) FITC Channel, (c) TRITC Channel, (d) Merged Image

In the Figure 5.10 and Figure 5.11 above, the nanoparticles are observed in green by attached FITC, fibroblast nuclei are visualized in blue by DAPI counterstaining and fibroblast filamentous actins are visualized in red by Phalloidin-TRITC. From the fluorescent images, we observed that, some SF/PPP nanoparticles had adhered to fibroblasts after 30 minutes. After 24 hours, more SF/PPP nanoparticles were observed to be adhered or internalized by fibroblasts compared to 30 minutes of incubation. Therefore, SF/PPP nanoparticles exhibited a time-dependent increase in the cell-associated fluorescence intensity.

Flow cytometric analysis

To measure quantitatively the cellular uptake and kinetic internalization of the SF/PPP nanoparticles further, flow cytometry analysis was employed to compare the cellular uptake of fluorescein loaded SF/PPP nanoparticles using HFF-1 fibroblasts at different times.

Method: HFF-1 human foreskin fibroblast cells were seeded on 25 cm² cell culture flask and allowed to grow to 80% confluence. 100 µg/ml fluorescein incorporated SF/PPP nanoparticles were incubated with cells for 0.5 hour, 4 hours and 24 hours. Cells were then washed extensively three times with 1 ×PBS, and then were detached from tissue culture dishes using 0.05% trypsin-EDTA (GIBCO), centrifuged and then resuspended in cold 1 ×PBS buffer and kept on ice. Cells were then analyzed by flow cytometry (Cytomics FC 500, Beckmann Coulter). Obtained data were processed with WinMDI version 2.9. The fluorescence intensity is proportional to the amount of SF/PPP nanoparticles internalized by the cells.

Results and discussion: Flow cytometric analysis has been widely used to assess cellular uptake of nanoparticle [171-173]. Figure 5.12 and Figure 5.13 show the fluorescence histograms of HFF-1 cells incubated with PPP nanoparticles and SF/PPP nanoparticles respectively for 0.5 hours, 4 hours and 24 hours respectively. Their corresponding fluorescent intensity measurements normalized by the number of cells are shown in Figure 5.14 and Figure 5.15 respectively. Cells with blank treatment were used as a negative control and

showed only the auto-fluorescence of the cells.

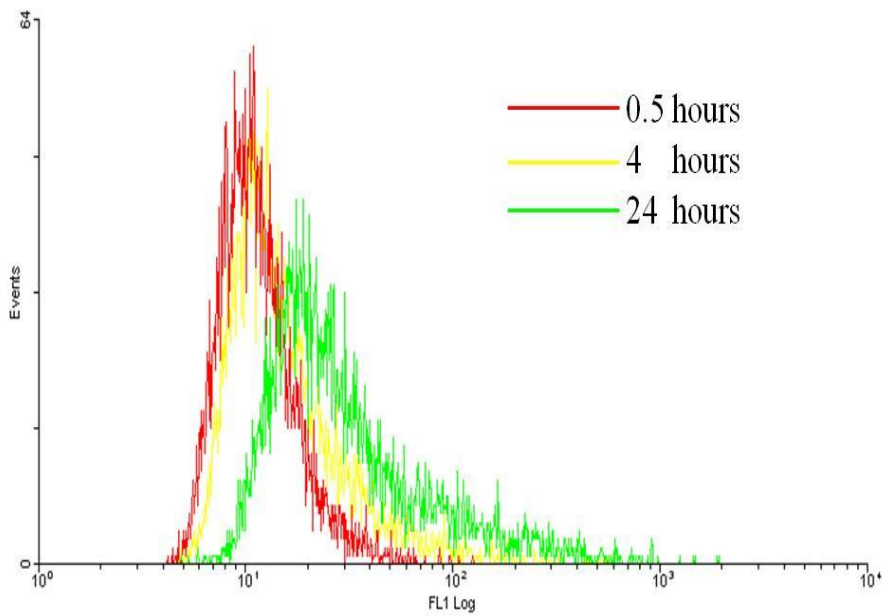


Figure 5.12 Fluorescence histograms of HFF-1 cells incubated with PPP nanoparticles for 0.5h, 4h and 24h

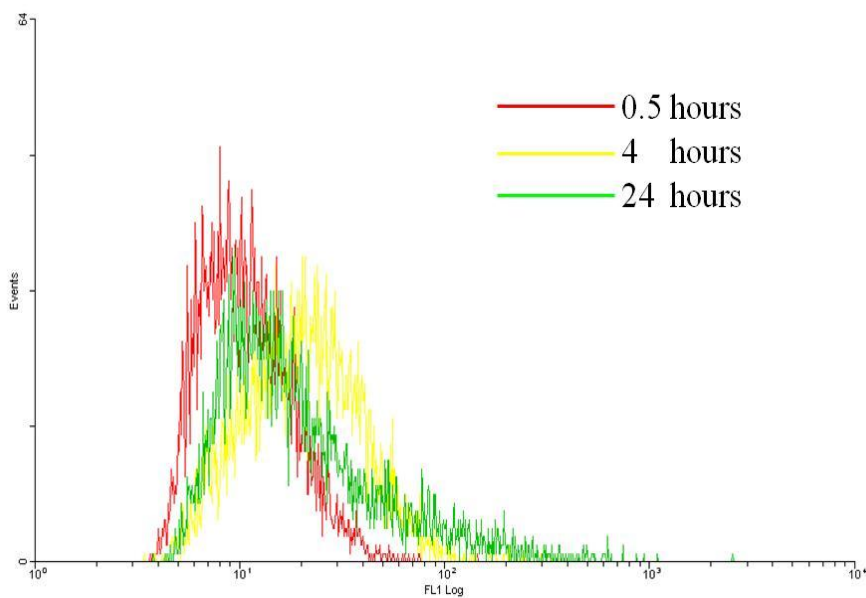


Figure 5.13 Fluorescence histograms of HFF-1 cells incubated with SF/PPP nanoparticle for 0.5h, 4h and 24h

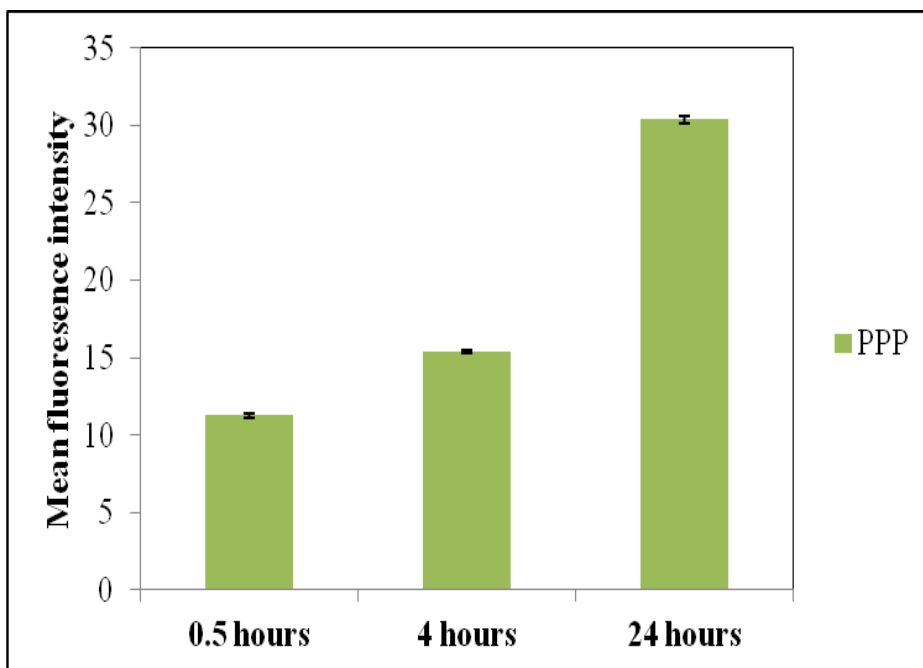


Figure 5.14 Fluorescent intensity measurements normalized by the number of HFF-1 cells incubated with PPP nanoparticles for 0.5h, 4h and 24h

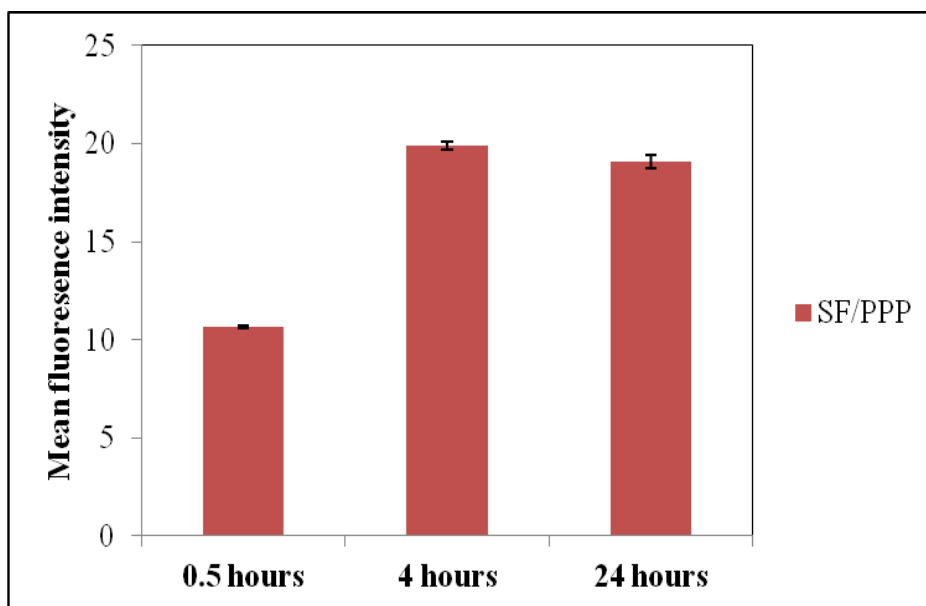


Figure 5.15 Fluorescent intensity measurements normalized by the number of HFF-1 cells incubated with SF/PPP nanoparticles for 0.5h, 4h and 24h

As shown in Figure 5.14 and Figure 5.15, with the increase of incubation

time from 0.5 hours to 4 hours, the fluorescent intensity of PPP and SF/PPP nanoparticles in HFF-1 was significantly enhanced. When incubation time increased to 24 hours, PPP nanoparticles can be internalized into HFF-1 cells continually and fluorescent intensity continues to be enhanced. However, fluorescent intensity of SF/PPP nanoparticles had no significant difference between 4 hours and 24 hours of incubation. It indicated that the speed of internalization of SF/PPP nanoparticles is higher than PPP nanoparticles by HFF-1. Therefore, the cellular uptake of SF/PPP nanoparticles reached a plateau and became saturated more quickly.

In conclusion, the enhanced cellular uptake with increase of time from 0.5 hours to 24 hours indicated by flow cytometry analysis is consistent with that shown in images observed using fluorescent microscopy. Moreover, incorporating silk fibroin into PPP nanoparticles can improve the cell adhesion and accelerate the cellular uptake of PPP nanoparticles. Many studies have showed that silk fibroin can enhance the cell affinity and improve the cell adhesion [6,168,174,175]. It is probably caused by strong affinity of silk fibroin to polysaccharides surrounding cells in tissues.

Generally, the cellular uptake of nanoparticles could be considered as an adhesion (or binding) process followed by the formation of vesicles and then the formed nanoparticle-containing vesicles are internalized by endocytosis [58]. Physicochemical characteristics such as particle size and surface properties played key roles in the internalization process [176, 177]. Nanoparticles made

of silk fibroin and amphilic PLLA-PEG-PLLA combined the advantages of natural and synthetic polymers. Importantly, silk fibroin possesses functional groups (i.e., amino and carboxylic groups) that could be used for surface modifications to achieve the targeted drug delivery. Therefore, SF/PPP nanoparticles by the SEDS process will be a potential application in nanoparticle drug delivery systems, especially targeted drug delivery systems.

5.6 Summary

In this Chapter, SF/PPP nanoparticles with a core-shell structure were successfully developed by the SEDS process. SEM and TEM images indicated that the silk fibroin nanoparticles were dispersed on the PPP nanoparticles. FTIR analysis indicated that composite nanoparticles consist of silk fibroin and PPP polymer. The results of XRPD indicated that the SEDS process reduced the crystalline state of PPP polymer. MTS and LDH assay suggested that SF/PPP nanoparticles possessed much better cell cytotoxicity compared with PPP nanoparticles. Furthermore, the results of cell adhesion assay demonstrated that SF/PPP nanoparticles exhibited good cell adhesion and internalization ability for cells. In conclusion, SF/PPP nanoparticles prepared by the SEDS process could be used as potential biomaterials in the biomedical field, especially nanoparticle drug delivery systems.

Chapter 6 Preparation, characterization and *in vitro* anti-tumor activity of PTX-SF/PPP nanoparticles

6.1 Introduction

The previous study in Chapter 5 has shown that silk fibroin/PPP nanoparticles prepared by the SEDS process is an effective drug carrier. Firstly, the incorporation of silk fibroin into the PPP nanoparticles improved biocompatibility and provided chemical modification. Secondly, the SF/PPP nanoparticles possessed a small particle size with narrow particle size distribution and could be taken up by cells effectively. Therefore, using the silk fibroin/PPP nanoparticles to load drugs and form a nanoparticle drug delivery system may be a potential application in the field of biomedical engineering.

Paclitaxel (PTX), a mitotic inhibitor used in cancer chemotherapy, has exhibited its potency against many kinds of cancers, including advanced ovarian, lung, and breast cancers. However, its poor solubility in water drastically limits its clinical application in its natural form. To enhance drug solubility, paclitaxel is commercially formulated at 6 mg/ml in a vehicle composed of 1:1 blend of Cremophor ®EL and ethanol to make Taxol®. Unfortunately, Cremophor ® EL is toxic and can cause severe side-effects, including hypersensitivity reactions, nephrotoxicity and neurotoxicity [178,179]. Also, the anticancer drug can not be selectively accumulated into tumors tissues. The non-specific distribution will reduce bioavailability and therapeutic efficiency of the anticancer drugs [180].

In order to improve the therapeutic efficacy of PTX and reduce side-effects, many researchers have developed alternative drug delivery systems, including parenteral emulsions, liposomes, nanoparticles and nanospheres [181-184]. Among them, polymer nanoparticle drug delivery systems have attracted much attention owing to high bioavailability and sustained drug release characteristics [185,186]. Besides, it enables many different routes of drug administration, including injection, transdermal absorption, oral application and inhalation. Especially, nanoparticles can extravasate into the tumor tissue via the leaky vessels surrounding tumors and then preferentially accumulate in solid tumors due to the enhanced permeation and retention (EPR) effect [187].

In this Chapter, the SEDS process will be used to prepare a PTX loaded SF/PPP (PTX-SF/PPP) nanoparticles delivery system. The surface morphology, physical and chemical properties, drug load, encapsulation efficiency and *in vitro* drug release properties of PTX-SF/PPP nanoparticles were measured. Moreover, the *in vitro* cytotoxicity and live/dead assay of PTX-SF/PPP nanoparticles were performed using cancer cell lines. The apoptosis index of cancer cells induced by the PTX drug was investigated by flow cytometry.

6.2 Preparation of PTX-SF/PPP nanoparticles by the SEDS process

For the preparation of PTX loaded-SF/PPP composite nanoparticles, the method was described in Section 5.2.2 of Chapter 5. Briefly, PTX was dissolved

in ethanol with silk fibroin nanoparticles and the DCM solution containing PPP was mixed together (for weight, PTX: silk fibroin nanoparticles: PPP =5:4:16), and the final solution concentration of PTX-SF/PPP was 0.5% (w/v). The operating conditions in the SEDS process can be described as follows (P: 10MPa, T: 35 °C; the flow rates of scCO₂ and solution were 25NL · h⁻¹ and 0.5 ml min⁻¹, respectively).

6.3 Surface morphology and structure of PTX-SF/PPP nanoparticles

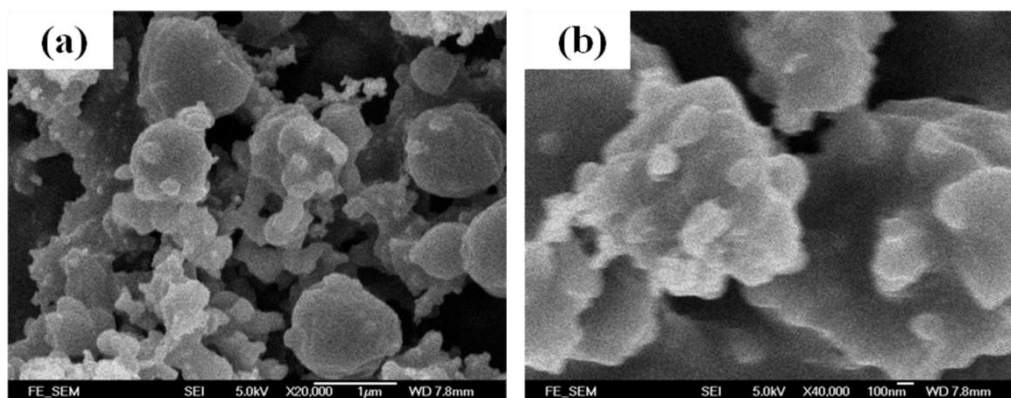


Figure 6.1 FE-SEM photographs of PTX-SF/PPP obtained by the SEDS process (a)

20000 × and (b) 40000 ×

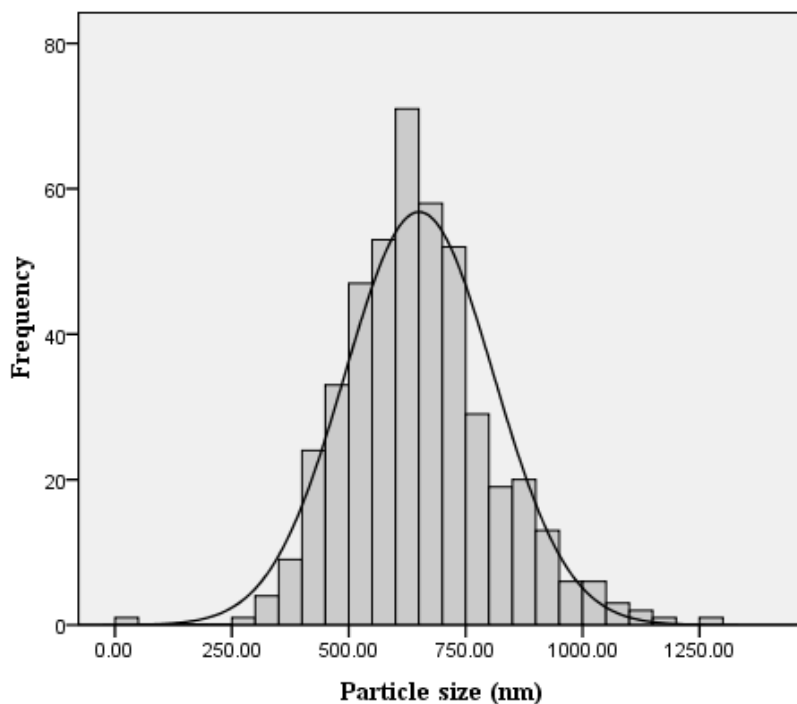


Figure 6.2 Particle size distribution of PTX-SF/PPP obtained by the SEDS process

The surface morphology of PTX-SF/PPP obtained by the SEDS process is shown in Figure 6.1. From this figure, the PTX-loaded SF/PPP nanoparticles exhibit nanostructured morphology with a rather spherical shape and rough surface. Figure 6.2 shows the particle size distribution of PTX-SF/PPP nanoparticles obtained by the SEDS process. Mean particle size is about 650.6 ± 158.8 nm and particle size distribution is 0.635. According to the particle size (50nm) of silk fibroin nanoparticles used in this experiment, it can be concluded that the rough surface results from the precipitation of silk fibroin nanoparticle on the surface of PPP nanoparticles. Obviously, the surface morphology appears to have no significant differences between SF/PPP nanoparticles and PTX-loaded SF/PPP nanoparticles.

6.4 Chemical and physical characterization

The methods about FTIR analysis and XRPD analysis were described in Section 4.4.1 and 4.4.2 of Chapter 4.

6.4.1 FTIR analysis

Figure 6.3 shows a characteristic absorption peak at 1759 cm^{-1} for the C=O Stretching in PPP of placebo SF/PPP. The major characteristic absorption peak of C–C stretching is shown for crystalline PTX at 709 cm^{-1} . After the SEDS process, the main peaks (709 cm^{-1}) appear at the same position compared with the physical mixtures, which suggests that the resulting products contain PTX. The presence of the peak at 1024 cm^{-1} further demonstrates that PTX has been encapsulated by SF/PPP nanoparticles successful.

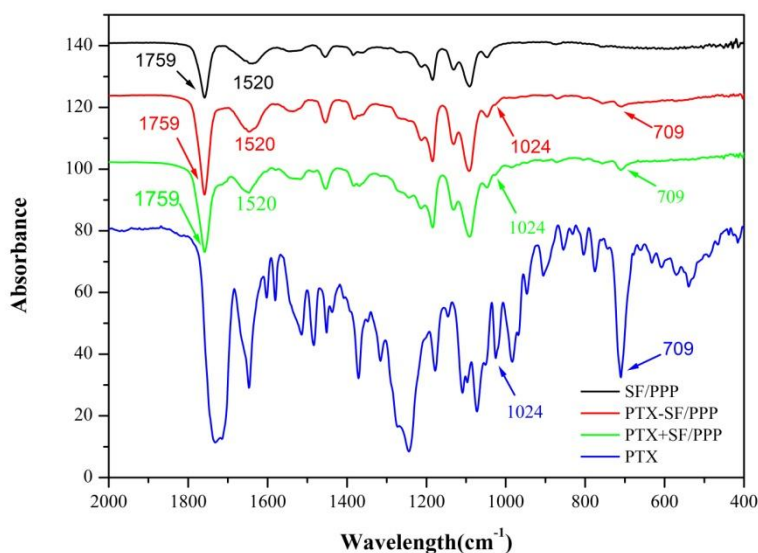


Figure 6.3 FTIR spectras of PTX, SF/PPP nanoparticles, physical mixture of PTX and SF/PPP nanoparticles, and PTX-SF/PPP nanoparticles

6.4.2 XRPD analysis

To investigate the physical state of the drug-loaded polymer nanoparticles prepared by the SEDS process, XRPD analysis was performed on the drug-loaded polymer nanoparticles. Figure 6.4 shows XRPD patterns of free PTX, SF/PPP and PTX-SF/PPP prepared by the SEDS process. Original paclitaxel exhibited the main characteristic XRPD peaks at $2\theta = 5.6^\circ$, 9.1° , 10.1° , 12.7° , 15.6° and 25.3° . After the SEDS process, nearly all the main characteristic peaks of crystalline PTX became weak, especially peaks at $2\theta = 10.1^\circ$ and 15.6° (in the physical mixtures, the weak characteristic peaks of crystalline PTX at 10.1° can still be observed in the XRD patterns). This indicated that the SEDS process reduces the crystallinity of PTX obviously, which could improve the solubility of PTX.

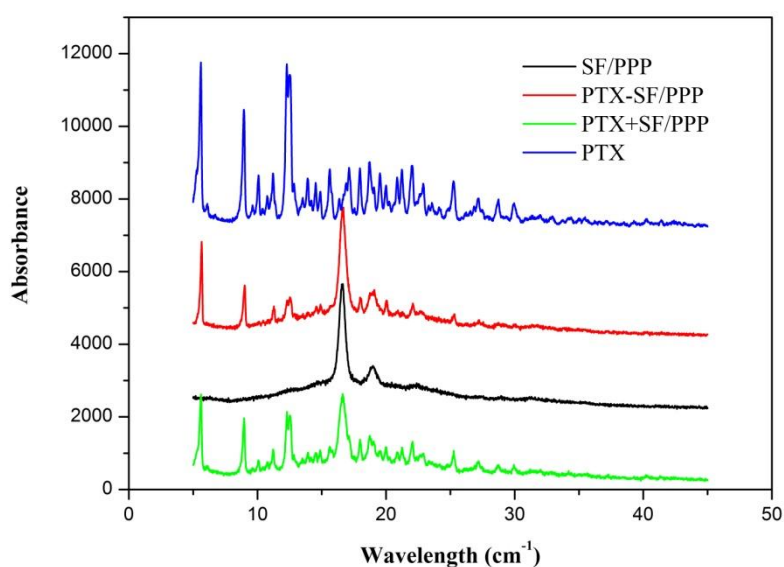


Figure 6.4 XRPD patterns of free PTX, SF/PPP and PTX-SF/PPP prepared by the SEDS process

6.5 Drug loading and *in vitro* release properties

6.5.1 Drug load (DL) and encapsulation efficiency (EE)

DL and EE are two kinds of important parameters to determine the drug loading properties of nanoparticles. The method to calculate the DL and EE of PTX were described in Section 4.6.3 of Chapter 4. In the present study, the theoretical weight ratio of drug to polymer was selected as 1:4 (i.e., theoretical drug load of 20%). The results of HPLC assay indicate the drug load (DL) and encapsulation efficiency (EE) was 18.12%, 90.21%, respectively. The DL and EE of SF/PPP nanoparticles in the study is higher than that of PLLA nanoparticles fabricated by CO₂-based nanoencapsulation technique disclosed by Kang *et al* [133]. It could be supposed that the higher DL and EE result from the different precipitation kinetics of the PTX and SF/PPP in the SEDS process. The silk fibroin nanoparticles can act as a crystal nucleus, which can promote the precipitation of PLLA-PEG-PLLA (PPP) and PTX. Actually, further studies are demanded to explore the actual reason. As nearly all the drug is loaded on the SF/PPP nanoparticles, it would be more commercially attractive.

6.5.2 *In vitro* drug release

In terms of the unique microenvironment surrounding tumor cells, in which the average extracellular pH value in tumors is between 6.0 and 7.0. However, the extracellular pH value in normal tissues is about 7.4. The *in vitro* release

profile of PTX from nanoparticles was studied in different pH conditions (pH 6.0 and 7.4). Figure 6.5 shows the *in vitro* release profile of PTX from PTX loaded SF/PPP (PTX-SF/PPP) nanoparticles in PBS buffer (pH 6.0 and 7.4). As shown in Figure 6.5, the drug release in PBS buffer (pH 7.4) was slower than that in in PBS buffer (pH 6.0). And 16.1% and 24.5% of paclitaxel was released at pH 7.4 and 6.0, respectively in one week (Figure 6.5). Therefore, there was no burst effect and PTX can be released in a controlled way from SF/PPP nanoparticles. Furthermore, nanoencapsulation of PTX by SF/PPP nanoparticles could improve the solubility of PTX. Besides, higher release rate of PTX from SF/PPP nanoparticles in PBS buffer (pH 6.0) as compared to that in PBS buffer (pH 7.4) also could benefit patients undergoing cancer treatment. Therefore, this nanoparticle drug delivery system could be suitable for tumor therapy.

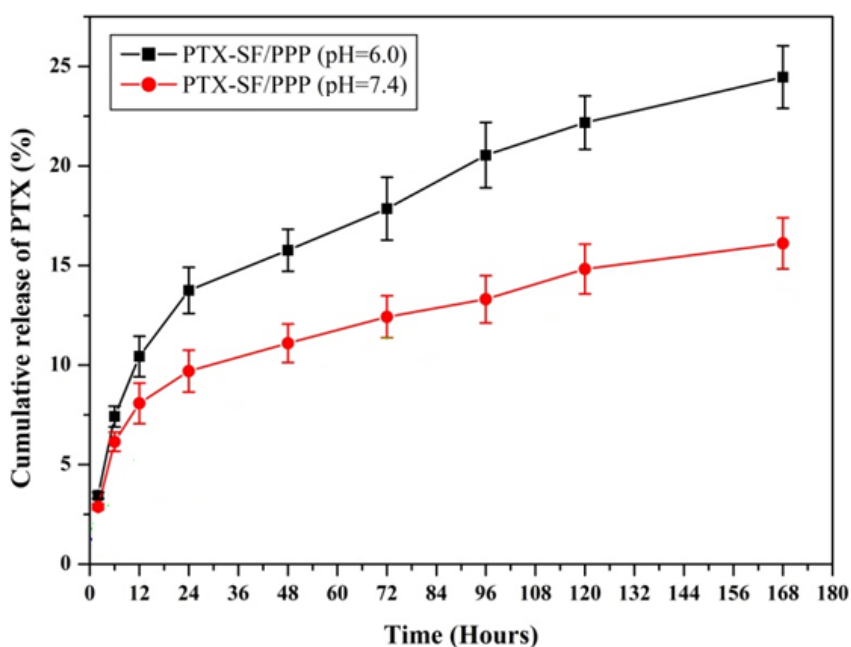


Figure 6.5 *In vitro* release profile of PTX from PTX-SF/PPP nanoparticles in PBS buffer (pH 6.0 and 7.4)

The faster release of PTX from the PTX-SF/PPP nanoparticles at lower conditions results from two possible reasons. One is that lower pH may cause faster degradation of SF/PPP polymer. The other is that the amino group of the drug could be protonated at lower pH condition. This pH-dependent release property has been shown to be beneficial for tumor treatment. It is likely that most PTX remain on the nanoparticles for a long time when PTX-SF/PPP nanoparticles is delivered into the plasma at normal physiological conditions (pH=7.4). After the PTX-SF/PPP nanoparticles reach the tumor tissue where the pH value is lower than that in the normal tissue and are internalized by tumor cells via endocytosis, the release of PTX will be enhanced. Therefore, pH-dependent release property decreases the side effect to the normal tissues and enhances the therapeutic efficiency against tumors.

6.5.3 MTS assay

The cytotoxicity and subsequent therapeutic potential of PTX-SF/PPP nanoparticles were evaluated by incubating *Human breast adenocarcinoma cell line* (MCF-7) and *Human liver hepatocellular carcinoma cell line* (HePG-2) cells with free PTX, SF/PPP nanoparticles, and PTX-SF/PPP nanoparticles (Equivalent 0.5 µg/ml PTX for nanoparticles) for 1, 2, 3, 5, and 7 days. Cell growth was then assessed by using the MTS assay described in Section 4.5.2 of Chapter 4. The MTS assay is an effective technique to assess the *in vitro* cytotoxicity of biomaterials. In the MTS assay, the correlation between

absorbance at 490 nm and cell numbers is linear.

Figure 6.6 and Figure 6.10 shows the cell viability of MCF-7 and HePG-2 cells incubated with nanoparticles for 1, 2, 3, 5 and 7 days respectively. Obviously, the empty SF/PPP nanoparticles have no obvious toxicity for tumor cell at all the time intervals tested. However, free PTX and PTX-SF/PPP nanoparticles inhibited growth of MCF-7 and HePG-2 cells significantly in one week. Therefore, the cytotoxicity of PTX-SF/PPP nanoparticles was mostly caused by the encapsulated PTX. Moreover, a clear time-dependent cytotoxicity of PTX and PTX-SF/PPP nanoparticles was observed in both experimental conditions.

***In vitro* cytotoxicity to MCF-7 cells**

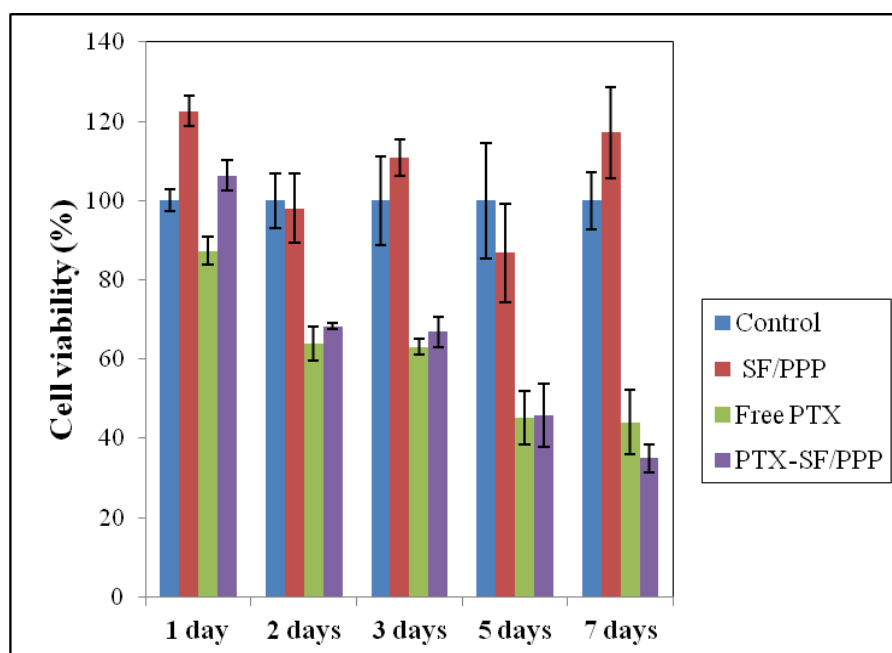


Figure 6.6 Cell viability of MCF-7 cells incubated with nanoparticles for 1, 2, 3, 5 and 7 days

As shown in Figure 6.6, the cell viability of MCF-7 cells after one day of incubation with free PTX decreased by about 12.6%. The cytotoxicity of free PTX was higher than that of PTX-SF/PPP nanoparticles significantly ($p < 0.05$). Similar results had been reported by Wu *et al* and Shi *et al* [188, 189]. It may be caused by two possible reasons. One is free PTX may diffuse into the MCF-7 cells under *in vitro* conditions more efficiently than PTX-SF/PPP nanoparticles, which are taken up by cells through endocytosis. The other possible reason is that free PTX is effective once it enters the cells, while the PTX encapsulated in SF/PPP nanoparticles needs escape from endosome/lysosome pathway for endocytosis and be released in a controlled way [188, 189]

After 7 days of incubation with free PTX, the cell viability of MCF-7 cells decreased by about 55.9%. However, PTX-SF/PPP nanoparticles possessed a slightly higher cytotoxicity ($p > 0.05$) and a approximately 65.1% decrease was observed in the cell viability of MCF-7 cells after 7 days of incubation with PTX-SF/PPP nanoparticles. It indicated that with the increase of incubation time from one day to 7 days, the PTX-SF/PPP nanoparticles exhibited faster improvement of cytotoxicity to MCF-7 cells than free PTX.

The results of MTS assay were supported by the optical images of MCF-7 cells shown in Figure 6.7, Figure 6.8 and Figure 6.9 incubated with SF/PPP nanoparticles, free PTX and PTX-SF/PPP nanoparticles at all the time intervals tested. It can be seen that SF/PPP nanoparticles have no obvious cytotoxicity. However, free PTX and PTX-SF/PPP nanoparticles exhibited obvious

cytotoxicity. With the increase of incubation time, the attachment ability of the cells became poor, a large number of cells floated and became round, then brushed off.

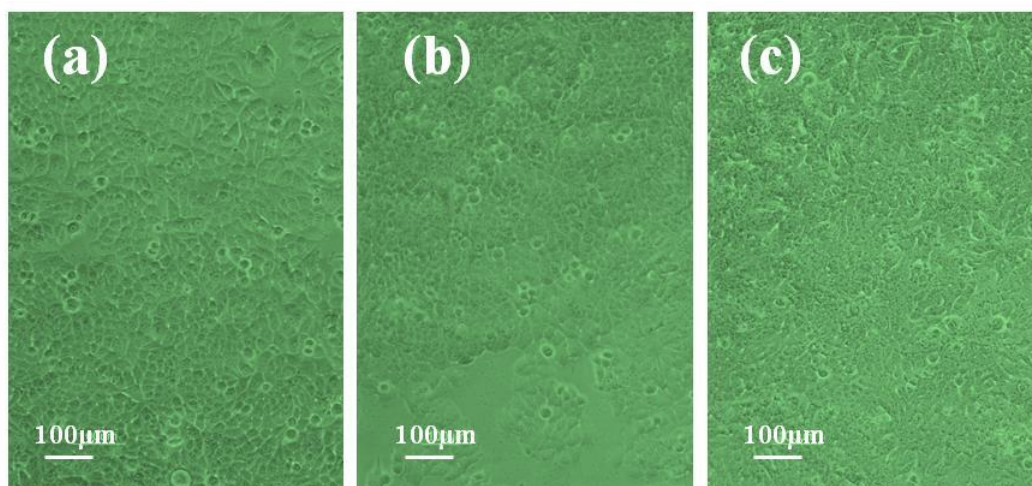


Figure 6.7 Optical images of MCF-7 cells incubated with 0.5 µg/ml SF/PPP nanoparticles for (a) 1 day, (b) 2 days and (c) 5 days

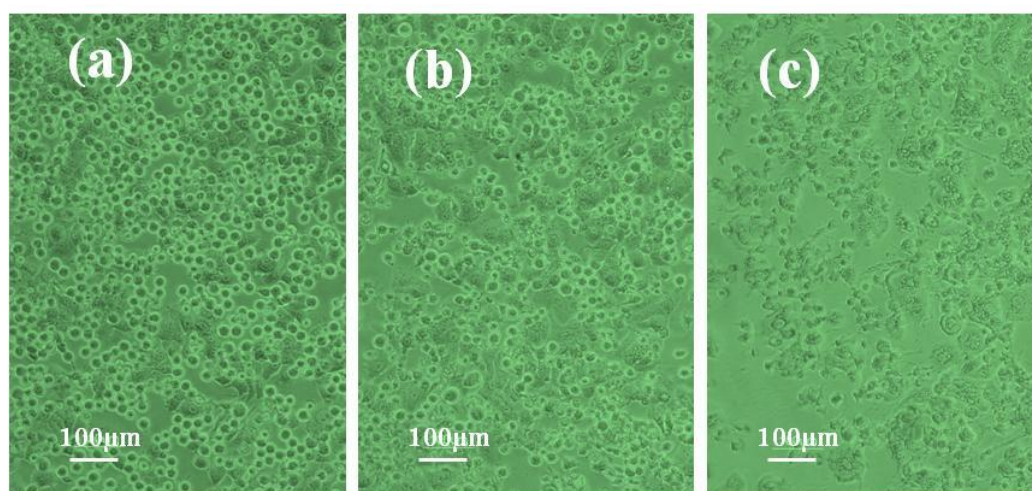


Figure 6.8 Optical images of MCF-7 cells incubated with 0.5 µg/ml PTX for (a) 1 day, (b) 2 days and (c) 5 days

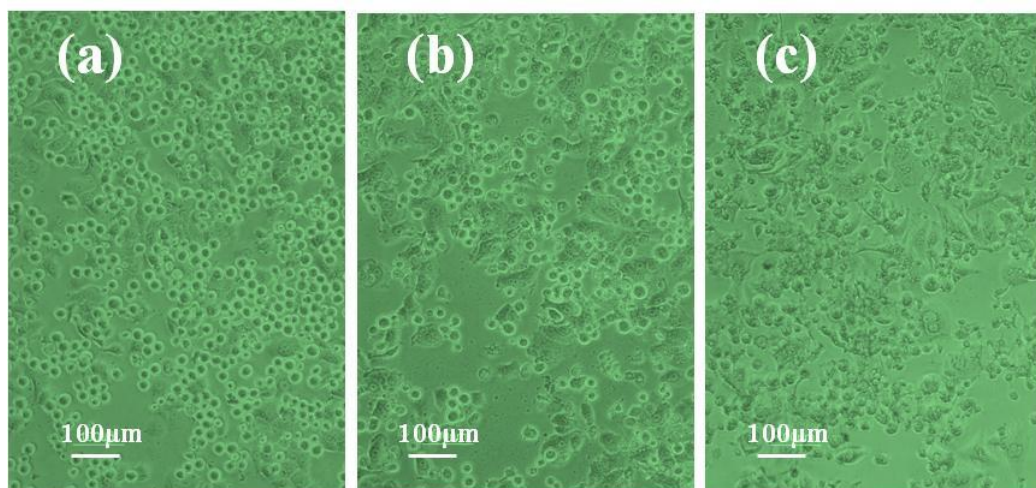


Figure 6.9 Optical images of MCF-7 cells incubated with 0.5 µg/ml PTX-SF/PPP nanoparticles for (a) 1 day, (b) 2 days and (c) 5 days

***In vitro* cytotoxicity to HePG-2 cells**

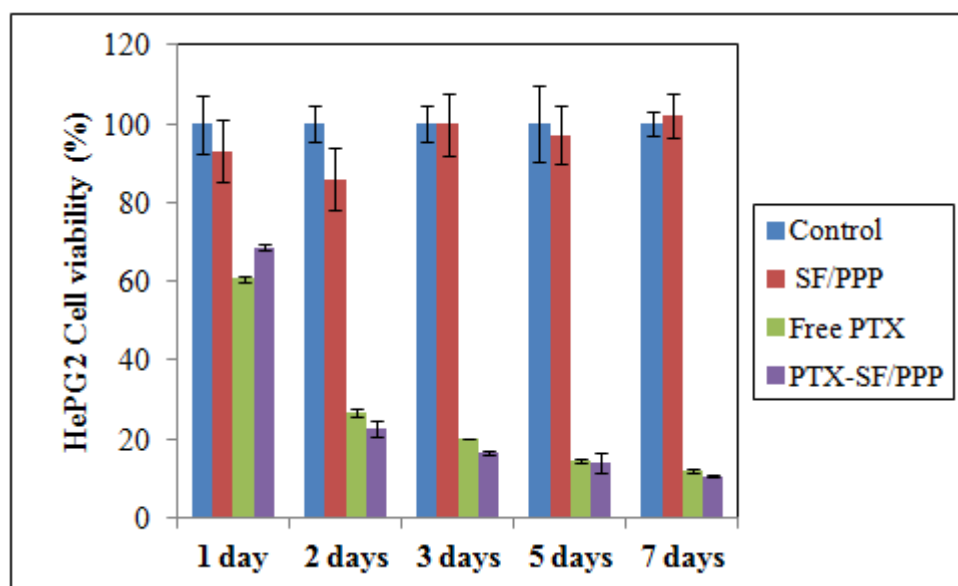


Figure 6.10 Cell viability of HePG-2 cells incubated with nanoparticles for 1, 2, 3, 5 and 7 days

As shown in Figure 6.10, after one day of incubation, the cytotoxicity of free PTX to HePG-2 cells was also higher than PTX-SF/PPP nanoparticles significantly ($p < 0.05$). Free PTX and PTX-SF/PPP nanoparticles caused a 39.3%

and 31.3% decrease in cell viability of HePG-2 cells respectively. One week later, free PTX and PTX-SF/PPP nanoparticles increased the toxicity significantly and cause a 88.2% and 89.4% decrease in the cell viability of MCF-7 cells respectively. However, there is no significant difference ($p>0.05$). Therefore, these results of MTS assay for HePG-2 cells were in accord with that for MCF-7 cells. However, the higher cytotoxicity of free PTX and PTX-SF/PPP nanoparticles to HePG-2 than MCF-7 cells might be attributed to different characteristics between MCF-2 and HePG-2 cells.

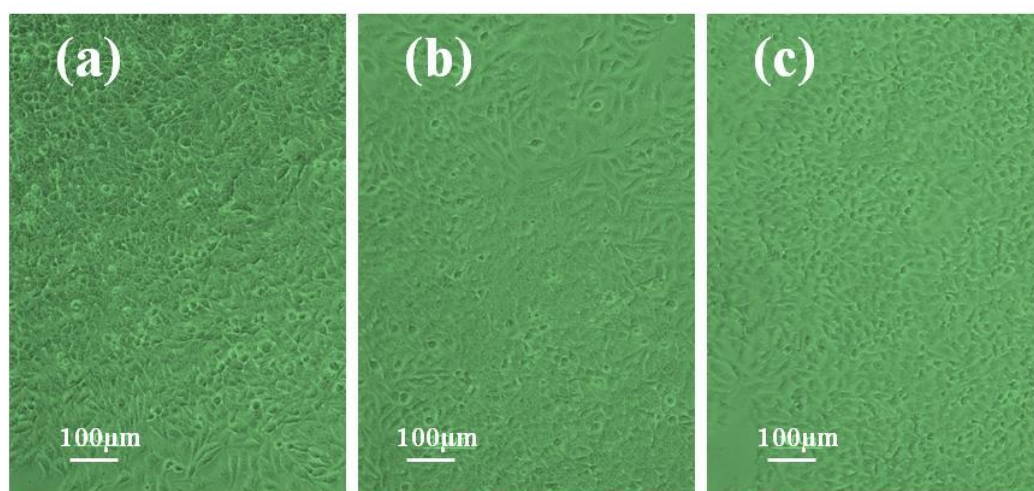


Figure 6.11 Optical images of HePG-2 cells incubated with 0.5 µg/ml SF/PPP nanoparticles for (a) 1 day, (b) 2 days and (c) 5 days

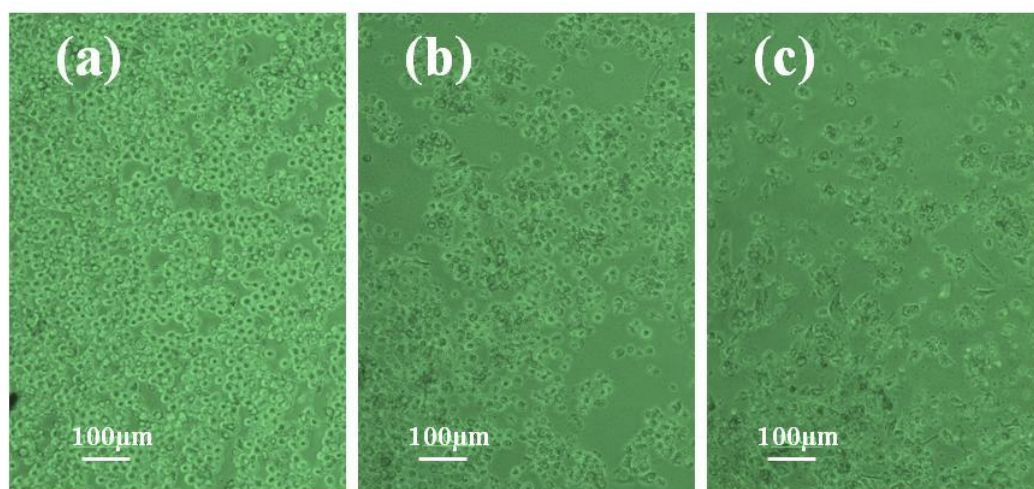


Figure 6.12 Optical images of HePG-2 cells incubated with 0.5 $\mu\text{g/ml}$ PTX nanoparticles for (a) 1 day, (b) 2 days and (c) 5 days

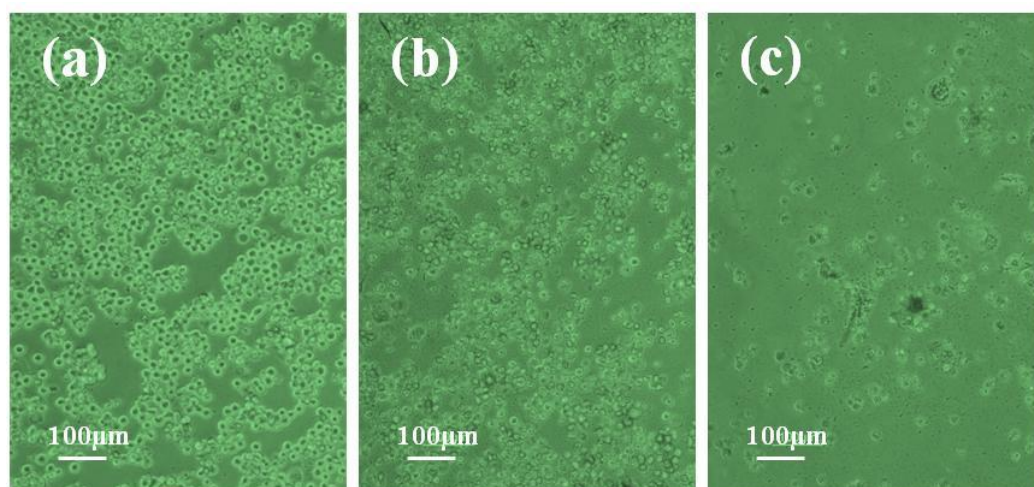


Figure 6.13 Optical images of HePG-2 cells incubated with 0.5 $\mu\text{g/ml}$ PTX-SF/PPP nanoparticles for (a) 1 day, (b) 2 days and (c) 5 days

Figure 6.11, Figure 6.12 and Figure 6.13 showed the cell morphologies of HePG-2 cells incubated with SF/PPP, free PTX and PTX-SF/PPP nanoparticles respectively at all the time intervals tested. There is no obvious cytotoxicity that can be observed for SF/PPP nanoparticles. And PTX and PTX-SF/PPP can induce continuous cytotoxicity of HePG-2 cells with the increase of incubation time. Generally it is thought that drug-loaded nanoparticles are taken up by cells through internalization, and subsequently release the drug inside the cells. These results indicated that the PTX-SF/PPP nanoparticles exhibited a sustained drug release property and thus can kill the tumor cell continuously.

Paclitaxel (PTX) is a widely-used anticancer drug at low doses. However, its application is limited by low solubility and severe side effects. Moreover, the drug carrier in clinical application especially Cremophor $\text{\textcircled{R}}$ EL is toxic and can

cause severe side effects [178, 179]. SF/PPP nanoparticles have excellent biocompatibility and the use of PTX-SF/PPP nanoparticles for systemic drug delivery would be beneficial to avoid the toxicity of free PTX alone to normal tissue, especially in the first day. With increase of incubation time from one day to 7 days, PTX-SF/PPP nanoparticles improved therapeutic efficiency significantly. It also indicated that the SEDS process is an effective technology to encapsulate PTX into SF/PPP nanoparticles without impairing the anti-tumor ability of PTX *in vitro*. Besides, owing to prolonged blood circulation of PTX-SF/PPP, enhanced permeability and the retention effect in the tumor interstitium and improvement of solubility of PTX, the PTX-SF/PPP nanoparticles may possess better anti-tumor activity than free PTX *in vivo* and thus have potential application in drug delivery system for tumor therapy.

6.5.4 Live/dead assay

The cytotoxicity of nanoparticles can also be evaluated by fluorescence-based live/dead assay. The procedure can determine the intracellular esterase activity and plasma membrane integrity using two fluorescent dyes fluorescein diacetate (FDA) and propidium iodide (PI) (Invitrogen, US), and thus identify live cells versus dead cells. FDA can pass through the cell membrane and live cells will convert FDA to produce a green fluorescence by intracellular esterase activity. PI is membrane impermeant which can only penetrate the membranes of dead or dying cells.

Method: HepG-2 cells and MCF-7 cells were seeded in 6 well plates and then allowed to attach overnight at 37 °C in a humidified cell incubator with 5% CO₂. After 24 hours, the initial viability of HepG-2 cells and MCF-7 cells after incubation with 0.5 µg/ml free PTX and PTX loaded SF/PPP nanoparticles, equivalent to containing 0.5 µg/ml PTX were characterized by cell live/dead assay based on the fluorescence of two dyes, fluorescein diacetate (FDA) and propidium iodide (PI) (Invitrogen, US). Cells were stained by 1 µg/ml FDA and 1 µg/ml PI simultaneously and then washed by 1×PBS. Stained cells were then observed using a Fluorescent Microscope (Nikon, Eclipse 80i). Viable cells fluoresce green and dead cells fluoresce red

Results and discussion: The results of the Live/Dead assay for MCF-7 cells when incubation with control, free PTX and PTX-SF/PPP nanoparticles respectively are shown in Figure 6.14, Figure 6.15 and Figure 6.16 respectively. And the results of the Live/Dead assay for HePG-2 cells when incubation with control, free PTX and PTX-SF/PPP nanoparticles are shown in Figure 6.17, Figure 6.18 and Figure 6.19 respectively. Live cells are labeled green because of their esterase activity. Dead cells are labeled red due to loss of membrane integrity. The cells in control group were not exposed to nanoparticles. As shown from these Live/Dead images, few or no red cell was observed in the control group. However, when incubating with free PTX or PTX-SF/PPP nanoparticles more dead cells were observed for HepG-2 than MCF-7 cells after 24 hours incubation. Moreover, the percentage of HePG-2

cells that were killed was higher than that of MCF-7 cells. These results supported that of MTS assay.

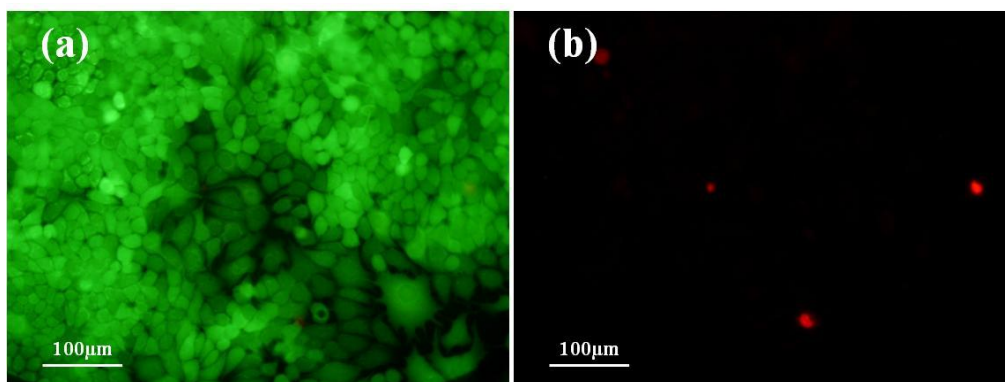


Figure 6.14 Live/Dead images of MCF-7 cells incubated with control (blank) for 24 hours (a) live cell and (b) dead cells

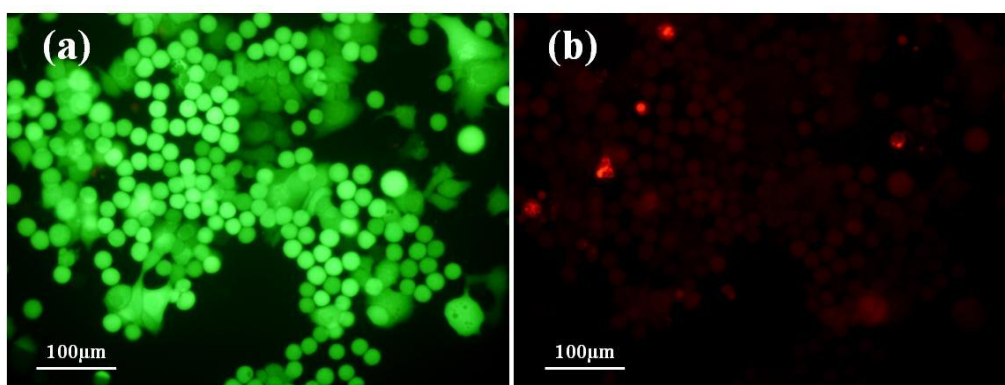


Figure 6.15 Live/Dead images of MCF-7 cells incubated with free PTX for 24 hours (a) live cell and (b) dead cells

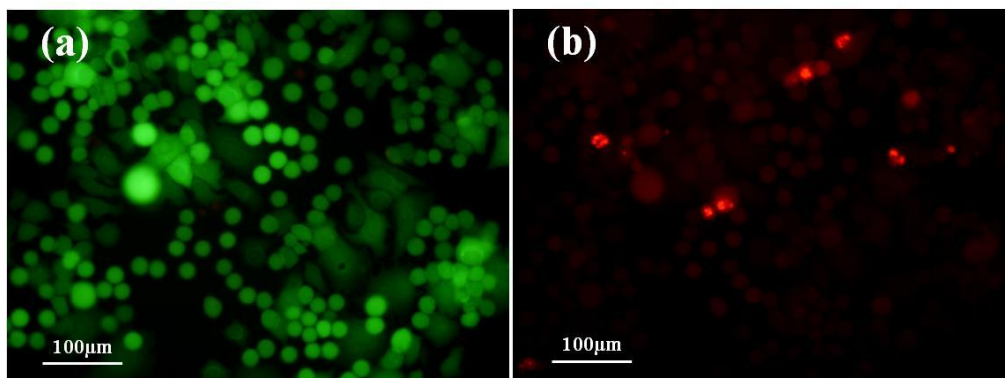


Figure 6.16 Live/Dead images of MCF-7 cells incubated with SF/PPP-PTX

nanoparticles for 24 hours (a) live cell and (b) dead cells

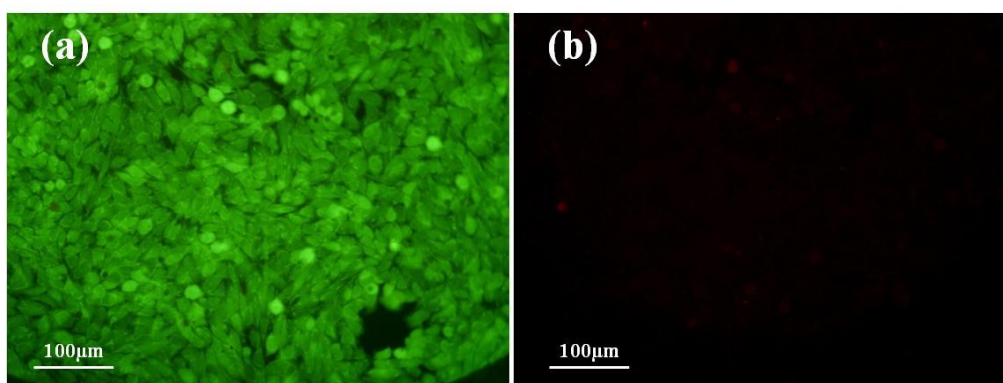


Figure 6.17 Live/Dead images of HePG-2 cells incubated with control (blank) for 24 hours (a) live cell and (b) dead cells

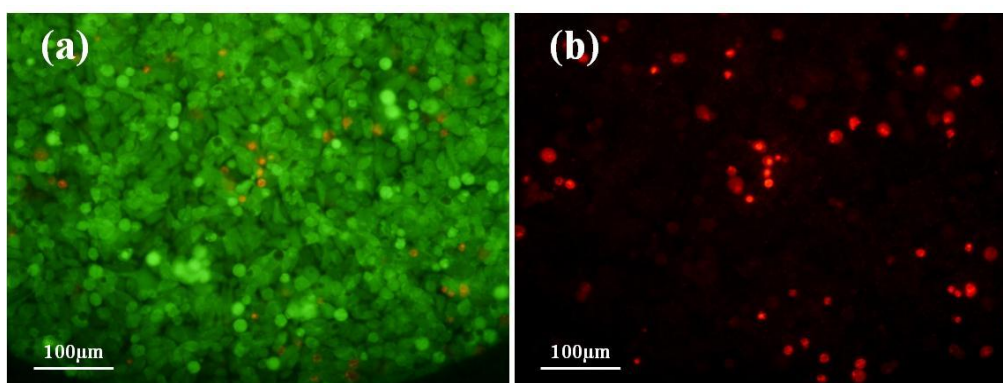


Figure 6.18 Live/Dead images of HePG-2 cells incubated with free PTX for 24 hours (a) live cell and (b) dead cells

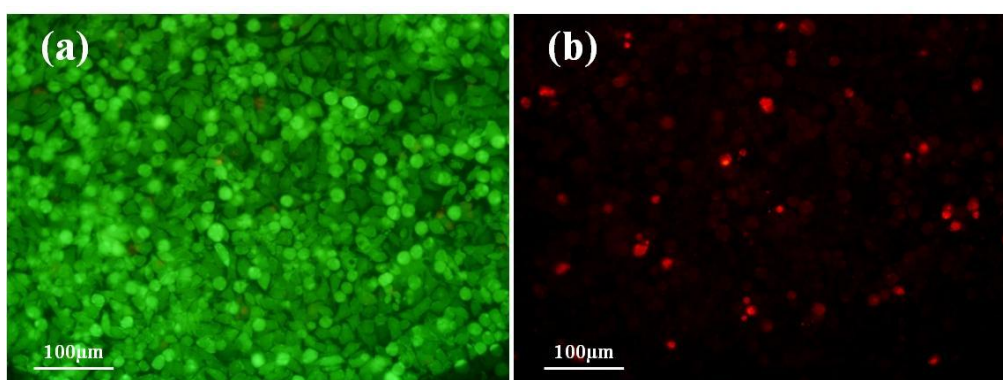


Figure 6.19 Live/Dead images of HePG-2 cells incubated with PTX-SF/PPP nanoparticles for 24 hours (a) live cell and (b) dead cells

6.6 Summary

In this Chapter, PTX loaded SF/PPP nanoparticles were fabricated successfully by the SEDS process. SEM images showed that they exhibit rather spherical shapes and rough surfaces, which result from many silk fibroin nanoparticles localized on the surface of PPP particles. FTIR analysis indicated that the PTX was encapsulated by SF/PPP nanoparticles. The results of XRD analysis supported the result of FTIR analysis and also suggested that the crystalline state of PTX has decreased obviously. Furthermore, the UV-Vis/HPLC analysis showed that drug load (DL) and encapsulation efficiency (EE) was 18.12% and 90.21% respectively. The *in vitro* drug release experiment suggested that the solubility of the paclitaxel increased a lot after being encapsulated by SF/PPP. Besides, the PTX-SF/PPP nanoparticles exhibited a sustained release and only 16.1% and 24.5% of paclitaxel was released at pH 7.4 and 6.0, respectively in one week. The different release rate of PTX indicated that the drug delivery system could be a potential application in tumor-targeted therapy. *In vitro* cytotoxicity for MCF-7 cells and HePG-2 cells suggested that PTX encapsulated in SF/PPP polymer has a slightly higher cytotoxicity after 7 days of incubation than that of free PTX. Therefore, PTX-SF/PPP nanoparticles will have potential application in particle drug delivery system for tumor therapy.

Chapter 7 Preparation, characterization and *in vitro* anti-tumor activity of smart PTX-FA-SF/PPP nanoparticles

7.1 Introduction

In previous studies, silk fibroin has been incorporated into synthetic PLLA-PEG-PLLA (PPP) polymer successfully to obtain silk fibroin/PLLA-PEG-PLLA (SF/PPP) nanoparticles by the SEDS process. PPP, as an amphiphilic polymer, can improve the solubility of insoluble drugs. Moreover, the hydrophilic poly (ethylene glycol) chains also can decrease opsonization and elimination by the reticuloendothelial system (RES) and result in long circulation in the blood. The introduction of silk fibroin can improve the biocompatibility of synthetic PLLA-PEG-PLLA polymer. Moreover, the reactive amino groups of silk fibroin allow the chemical modification site to develop smart drug delivery system.

In this Chapter, folic acid (FA) was covalently linked to PTX loaded silk fibroin/PLLA-PEG-PLLA (PTX-SF/PPP) nanoparticles to prepare smart PTX-FA-SF/PPP nanoparticles for tumor-targeted delivery and achieve objective 5 described in Section 1.2 of Chapter 1. The morphology, chemical properties, drug loading and *in vitro* release properties of PTX-FA-SF/PPP nanoparticles were investigated. Furthermore, the cellular uptake behavior of FA-SF/PPP nanoparticles was studied by flow cytometry. Finally, *in vitro* cytotoxicity of

drug-loaded nanoparticles was evaluated using cancer cell lines and normal cell lines.

7.2 Fabrication of PTX-FA-SF/PPP nanoparticles

20 mg of folic acid (FA) and 4 mg of N-hydroxysuccinimide (NHS) were dissolved in 1 ml of 0.1 N NaOH. Then 20 mg of N-(3-dimethylaminopropyl)-N-ethylcarbodiimide (EDC) was added into the resulting solution and underwent constant shaking in the dark for 30 min to obtain NHS-folate at 20 °C. Subsequently, 4 ml of PTX-SF/PPP nanoparticles (PTX: SF: PPP=5: 4: 16) suspension (content 2.5 mg/ml) was added into the solution above to react with NHS-Folate for 2h at room temperature. The reaction mixture was washed using ddH₂O and then purified from unreacted folic acid by three cycles of differential centrifugation (14000 rpm, 5 min) and the pellets were dried for the next experiment.

As mentioned before, the silk fibroin nanoparticles were incorporated into the PLLA-PEG-PLLA polymer to form the PTX-SF/PPP nanoparticles by the SEDS process. A large number of silk fibroin nanoparticles were localized on the surface of PTX-SF/PPP nanoparticles. Therefore, the amino group of silk fibroin can react with the folic acid to form PTX-FA-SF/PPP nanoparticles. Figure 7.1 shows the illustration of PTX-FA-SF/PPP nanoparticles. The schematic diagram of the process for preparing PTX-FA-SF/PPP nanoparticles is presented in Figure 7.2.

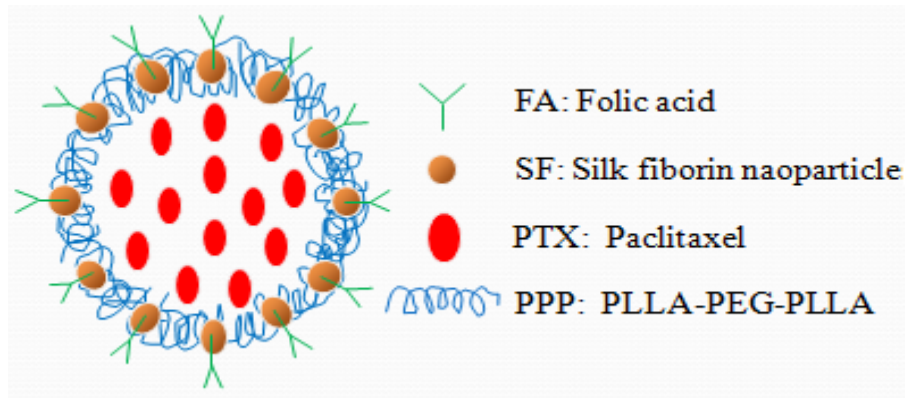


Figure 7.1 Illustration of PTX-FA-SF/PPP nanoparticles

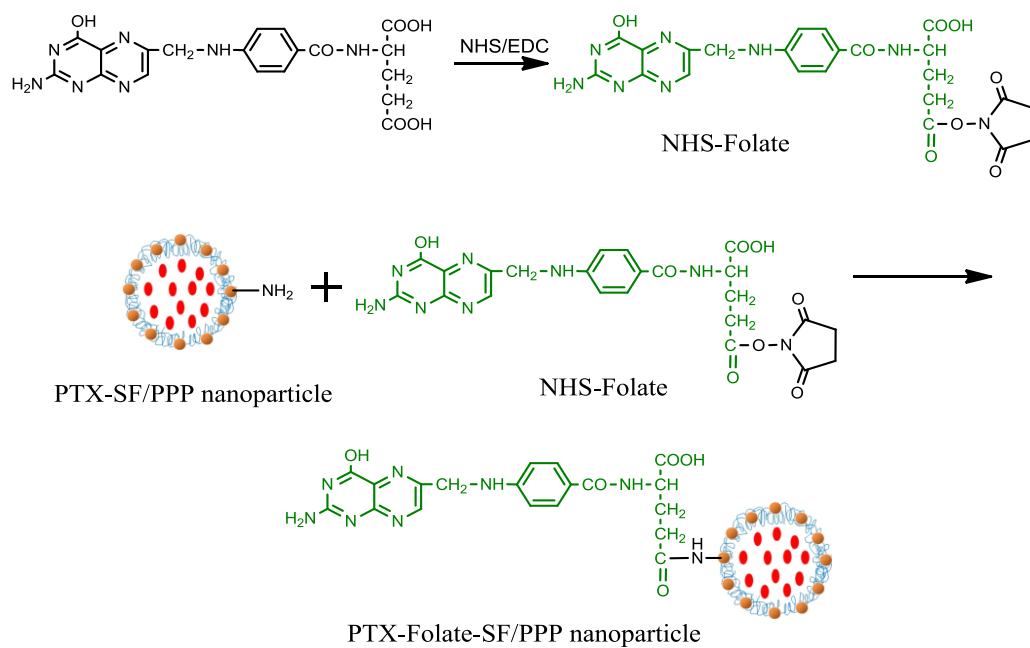


Figure 7.2 Schematic diagram of the preparation strategy for the production of

PTX-FA-SF/PPP nanoparticles

7.3 Surface morphology and particle size distribution

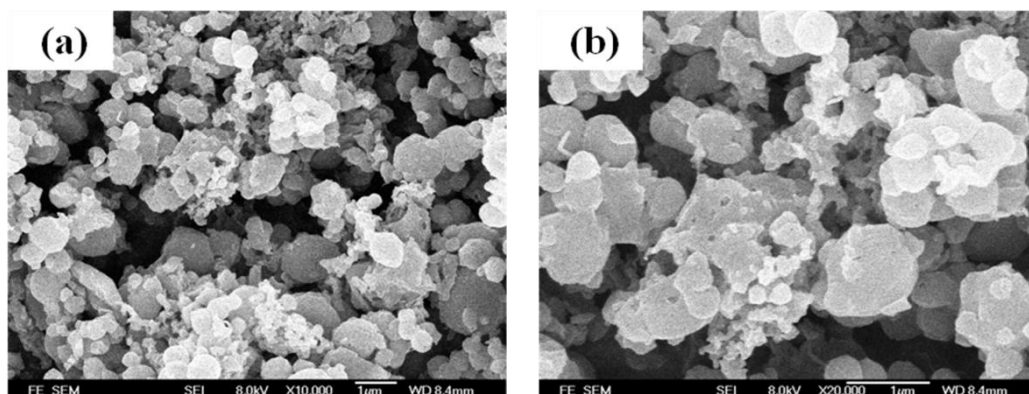


Figure 7.3 FE-SEM photos of PTX-FA-SF/PPP nanoparticles (a) 10000 × and (b) 20000 ×

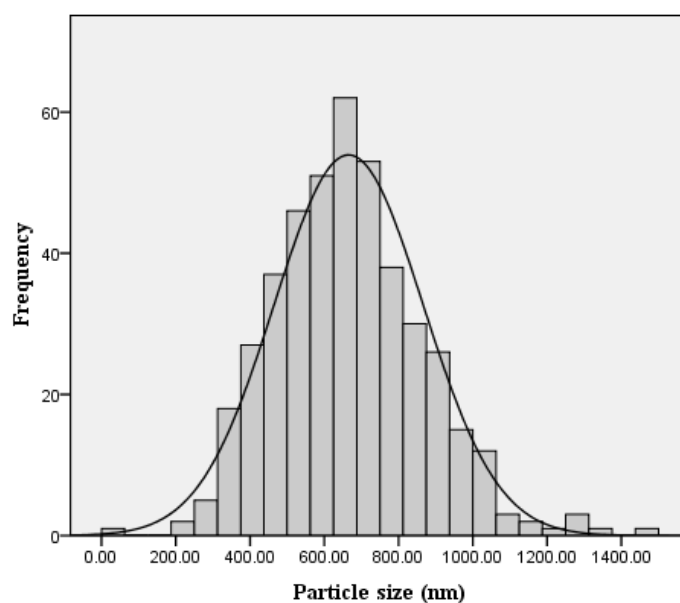


Figure 7.4 Particle size distribution of PTX-FA-SF/PPP nanoparticles

The surface morphology and particle size distribution of PTX-FA-SF/PPP nanoparticles prepared by the SEDS process are shown in Figure 7.3 and Figure 7.4 respectively. According to these figures, the particle size and particle size distribution of PTX-SF/PPP nanoparticles is 665.4 ± 200.6 nm and 0.776 respectively. Compared with that of PTX-SF/PPP nanoparticles, the particle size

of PTX-FA-SF/PPP increased by about 15 nm. However, there is no significant difference. The bigger size might result from successful folic acid conjugation. Besides, many small pores appear on the surface morphology of PTX-FA-SF/PPP nanoparticles. However, the surface of PTX-SF/PPP prepared by SEDS process is tight. It should be noted that the folic acid modification occurs in the NaOH solution and dried PTX-FA-SF/PPP nanoparticles have been obtained by freeze drying process. Therefore, these pores might be attributed to degradation of PTX-SF/PPP nanoparticles in the process of folic acid modification slightly and water evaporation from PTX-FA-SF/PPP nanoparticles by freeze drying.

7.4 Chemical properties

7.4.1 FTIR analysis

Figure 7.5 shows FTIR spectras of folic acid (FA), PTX-SF/PPP nanoparticles, and PTX-FA-SF/PPP nanoparticles. The characteristic peak of folic acid at 1606 cm^{-1} , 1695 cm^{-1} and 1483 cm^{-1} is due to benzene's conjugated double absorption), ester bond, and hetero-ring, conjugated double bond, respectively. For the PTX-SF/PPP nanoparticles, the main characteristic peak at 709 cm^{-1} , 1521 cm^{-1} and at 1759 cm^{-1} is attributed to C–C stretching of PTX, β -sheet of silk fibroin nanoparticles and C=O stretching of PPP in SF/PPP nanoparticles respectively. After folic acid modification, no obvious characteristic FTIR absorption peak of folic acid was observed in the spectra of

PTX-FA-SF/PPP nanoparticles. In general, the characteristic FTIR absorption peak of folic acid is very difficult to be found due to low content of folic acid grafted on the PTX-SF/PPP. In order to study the conjugation of folic acid with the PTX-FA-SF/PPP, an enzymatic hydrolysis experiment was designed to characterize PTX-FA-SF/PPP and determine the content of folic acid on the PTX-FA-SF/PPP.

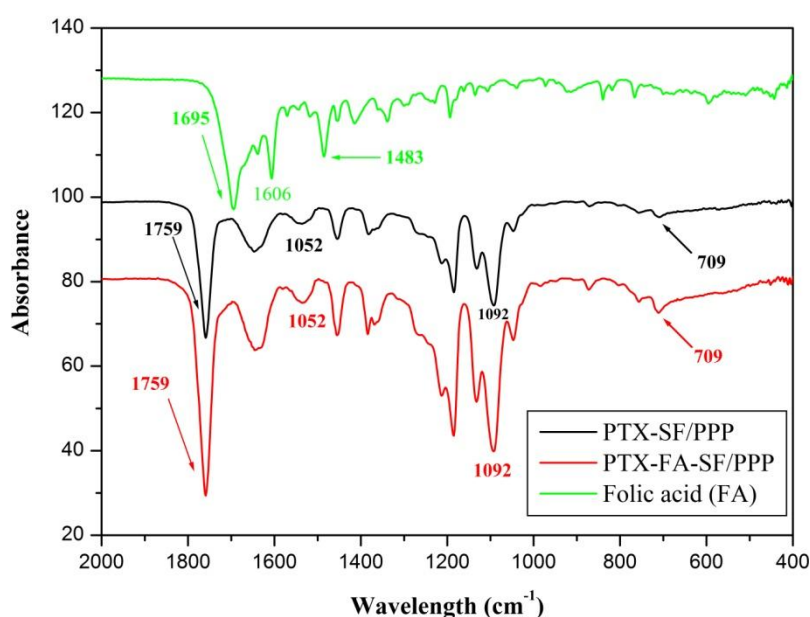


Figure 7.5 FTIR spectras of folic acid (FA), PTX-SF/PPP nanoparticles, and PTX-FA-SF/PPP nanoparticles

7.4.2 Determination of folic acid content

Calibration curve of folic acid

Method: 1 mg of folic acid was dissolved in 10 ml of 0.1N NaOH. The resulting solution was diluted by pH 8.0 NaOH to obtain folic acid solutions with

different concentrations (0.05; 0.025; 0.0125; 0.00625; 0.003125 mg/ml). An ultraviolet spectrophotometer was used to measure their OD value at 280 nm and 365 nm respectively. Then an equation could be calculated by performing linear regression.

Results: Figure 7.6 and Figure 7.7 show the calibration curves of folic acid when the wavelength is 365 nm and 280 nm respectively. As shown in these two figures, there is a linear response for folic acid within a concentration range of 0.05~0.003125 mg/ml under UV detection. When the wavelength is 365 nm and 280 nm, the equation is $Y=0.06686+16.87316*X$ ($R^2=0.99783$) respectively.

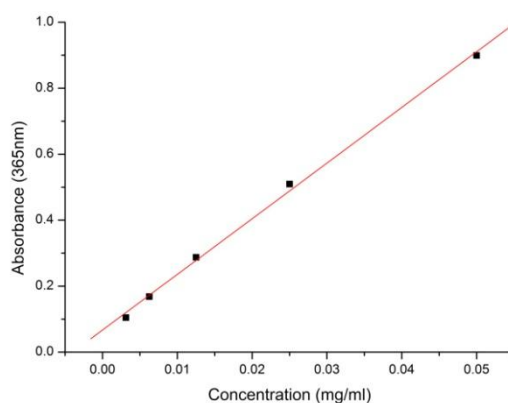


Figure 7.6 Calibration curve of folic acid at 365nm

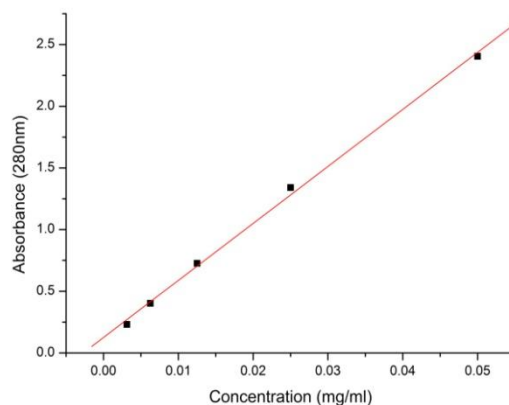


Figure 7.7 Calibration curve of folic acid at 280nm

Determination of folic acid content

10 mg of lyophilized PTX-FA-SF/PPP nanoparticles and 10 mg of PTX-SF/PPP nanoparticles (control group) were added into 4 ml of 0.25 g/ml pancreatin solution and reacted for 24 hours to obtain hydrolysates at room temperature. Then the supernatant from the enzymatic hydrolysate above obtained by centrifugation (14000 rpm, 5 min) was analyzed by an UV spectrophotometer (Shimadzu, Tokyo, Japan) in the 200~500 nm range. The percentage of folic acid conjugated with PTX-SF/PPP nanoparticles was measured according to calibration curve of folic acid when the wavelength is 280 and 365 nm respectively.

The amount of folate conjugated with PTX-SF/PPP nanoparticles was determined using an ultraviolet spectrophotometer. Figure 7.8 indicates the UV-Vis spectra of folic acid (FA), PTX-SF/PPP nanoparticles, and pancreatin hydrolysates of PTX-SF/PPP nanoparticles and PTX-FA-SF/PPP nanoparticles.

In general, silk fibroin consists of Ala (43.07%), Gly (27.27%), Ser (11.26%), Tyr (5.26%) and Asp (4.47%). Strong absorption was observed at around 205 and 280 nm owing to the presence of the side chains (conjugated double bond: C=C-C=C) of aromatic amino acids (Tyr, Ser). For folic acid, the characteristic peaks are at 280 nm and at 365 nm. Obviously, compared to that of PTX-SF/PPP nanoparticles, the UV-Vis spectra of pancreatin hydrolysates PTX-FA-SF/PPP nanoparticles showed a stronger peak at 280 nm and new peak at 365 nm. This indicates that the folate was conjugated with the amino

groups of PTX-SF/PPP nanoparticles successfully.

According to the calibration curve of folic acid at 365 nm, it can be calculated that the folic acid (FA) content is about 0.01669 mg/10 mg of PTX-FA-SF-PPP nanoparticles. Folic acid can bind to tumor cell selectively, promote tumor-targeted internalization. Therefore, PTX-FA-SF-PPP nanoparticles will have potential application in tumor-targeted drug delivery.

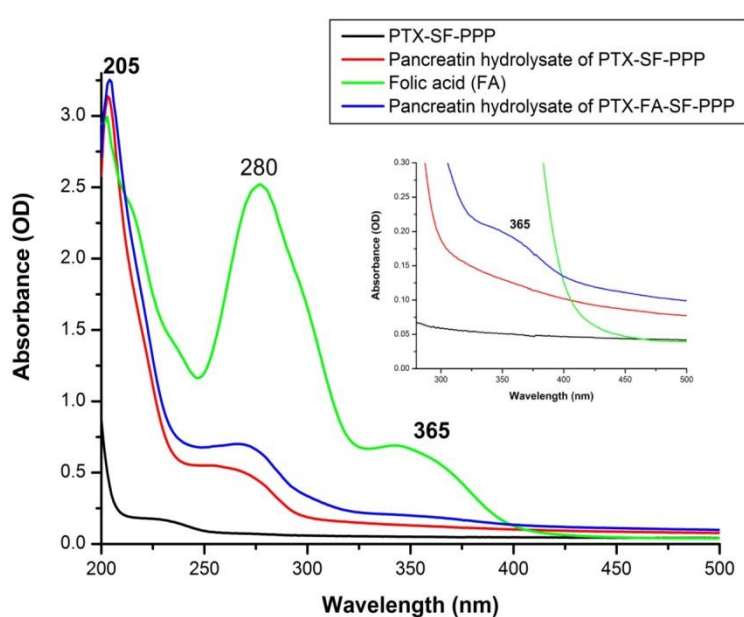


Figure 7.8 UV-Vis spectras of folic acid (FA), PTX-SF/PPP nanoparticles, pancreatin hydrolysates of PTX-SF/PPP nanoparticles and PTX-FA-SF/PPP nanoparticles

7.5 Drug load, encapsulation efficiency, and *in vitro* drug release properties

7.5.1 Drug load and encapsulation efficiency

The UV-Vis/HPLC assay was used to measure the PTX content in

lyophilized PTX-FA-SF/PPP nanoparticles. The method was described in Chapter 6. In this study, the drug load (DL) and encapsulation efficiency (EE) of PTX-SF/PPP nanoparticles is 18.1% and 90.6% respectively. After folic acid modification, the DL and EE decreased to 15.5% and 77.4% respectively. The loss of PTX may have resulted from the drug release and washing out of PTX-SF/PPP nanoparticles by the ddH₂O.

7.5.2 *In vitro* drug release

The UV-Vis/ HPLC assay method was used to measure the PTX content in lyophilized PTX-FA-SF/PPP nanoparticles. The method was described in Chapter 6. In this study, the DL and EE of PTX-SF/PPP nanoparticles were 18.1% and 90.6% respectively. After folic acid modification, the DL and EE of PTX-FA-SF/PPP nanoparticles decreased to 15.5% and 77.4% respectively. The loss of PTX may have resulted from the drug release and washing out of PTX-SF/PPP nanoparticles by the ddH₂O.

The *in vitro* drug release property of PTX-FA-SF/PPP nanoparticles is also investigated in PBS solution under different pH conditions (6.0 and 7.4). As shown in Figure 7.9, in the first 6 hours, there was a burst effect with regard to PTX. And the cumulative release of PTX was 8.1% and 11.6% in PBS solution (pH 7.4) and PBS solution (pH 6.0) respectively. Then the PTX could be released in a stable way. After 7 days, the cumulative release of PTX increased to 27.8% and 21.3% in PBS solution (pH 7.4) and PBS solution (pH 6.0), respectively.

Compared to the *in vitro* drug release curve of PTX from PTX-SF/PPP, it can be concluded that the drug release rate of PTX-FA-SF/PPP nanoparticles is slightly higher than that of PTX-SF/PPP nanoparticles. In general, the drug release may be mainly controlled by drug diffusion from polymer particles. Therefore pores localized on the surface of PTX-FA-SF/PPP nanoparticles could improve the release of PTX molecules.

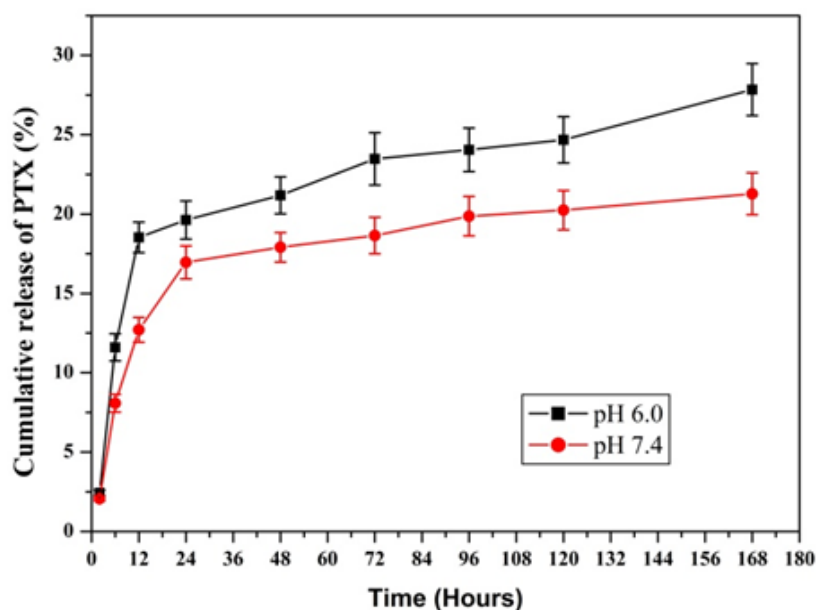


Figure 7.9 *In vitro* release profile of PTX from PTX-FA-SF/PPP nanoparticles in PBS buffer (pH 6.0 and 7.4)

7.6 Tumor targeting analysis

The cellular uptake of the fluorescent SF/PPP nanoparticles and folate conjugated SF/PPP nanoparticles (FA-SF/PPP) was analyzed using a flow cytometry method shown in Section 5.5.3 of Chapter 5 to quantify the amount of the nanoparticles internalized by the cells. The flow cytometry evaluates the fluorescence intensity of each cell. In order to assess the tumor targeting property

of the FA-SF/PPP nanoparticles against folate receptors (FR) on the cell, MCF-7 cell line and HFF-1 cell line were used as FR-positive cancer cells and FR-negative normal cells, respectively. Figure 7.10 and Figure 7.11 shows the fluorescence histograms of HFF-1 and MCF-7 cells incubated with SF/PPP nanoparticles for 0.5h, 4h and 24h respectively. Their results about cellular uptake presented by mean fluorescence intensity of HFF-1 and MCF-7 cells incubated with SF/PPP nanoparticles for 0.5h, 4h and 24h have been exhibited in Figure 7.12. Figure 7.13 and Figure 7.14 shows the fluorescence histograms of HFF-1 and MCF-7 cells incubated with FA-SF/PPP nanoparticles for 0.5h, 4h and 24h respectively. The Figure 7.15 summarized the results of Figure 7.13 and Figure 7.14 and indicated the results of the cellular uptake presented by mean fluorescence intensity of HFF-1 and MCF-7 cells incubated with FA-SF/PPP nanoparticles for 0.5h, 4h and 24h.

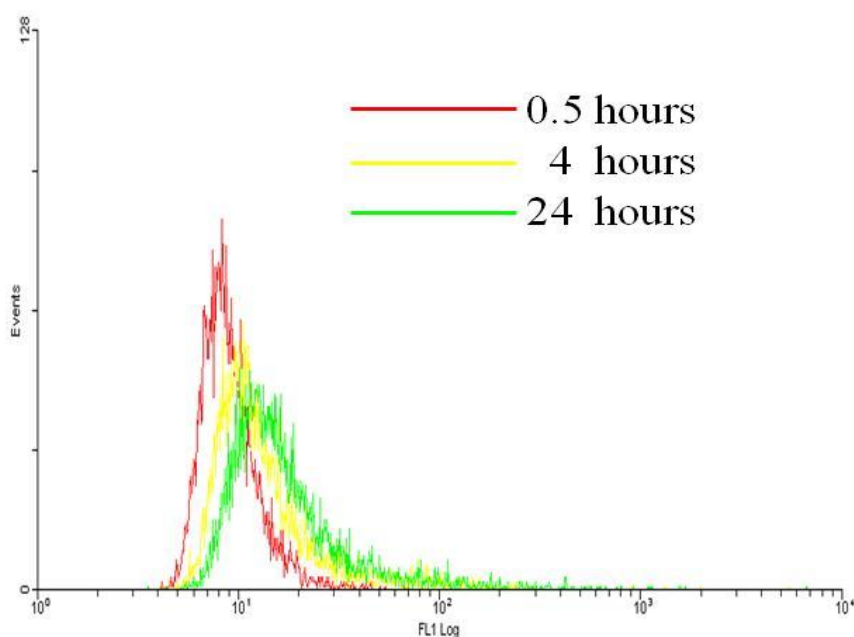


Figure 7.10 Fluorescence histograms of HFF-1 cells incubated with SF/PPP nanoparticles for 0.5h, 4h and 24h

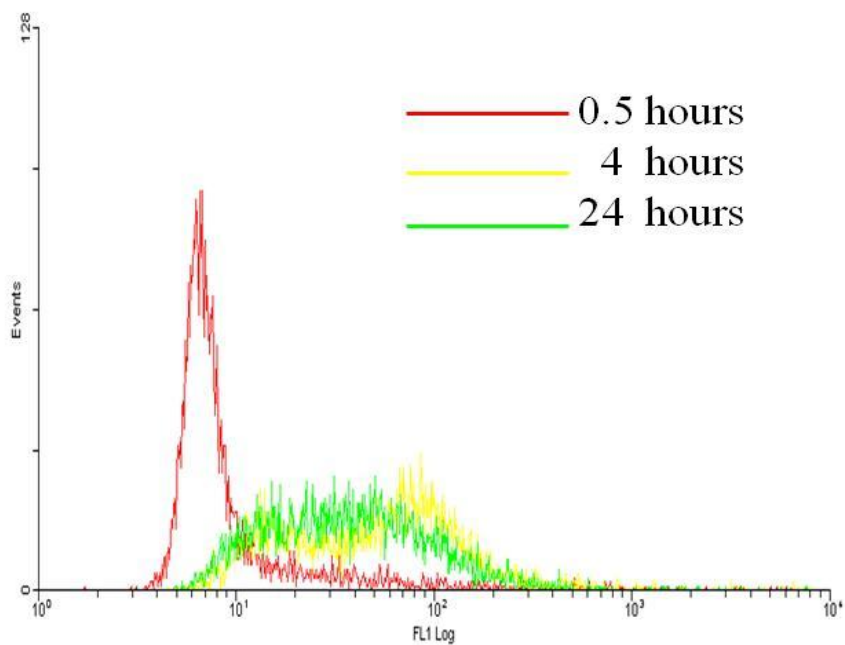


Figure 7.11 Fluorescence histograms of MCF-7 cells incubated with SF/PPP nanoparticles for 0.5h, 4h and 24h

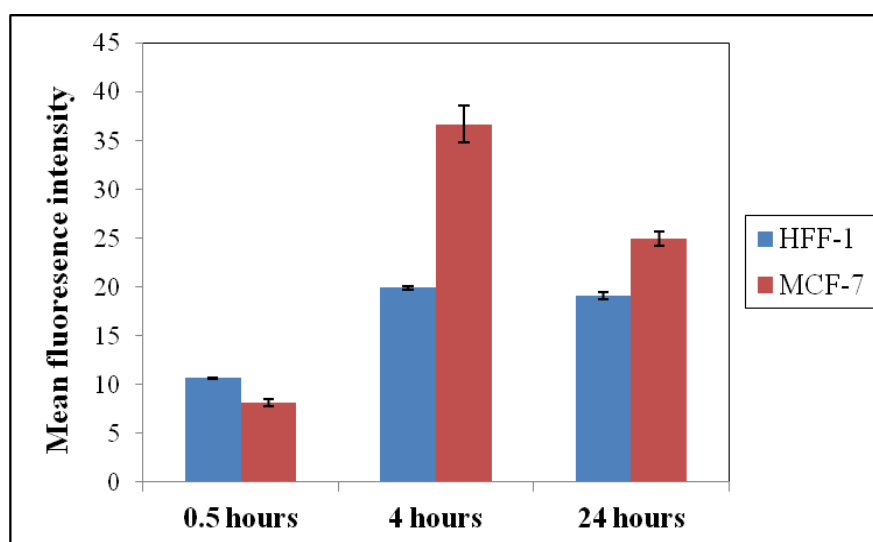


Figure 7.12 Cellular uptake of SF/PPP nanoparticles by HFF-1 and MCF-7 cells for 0.5h, 4h and 24h

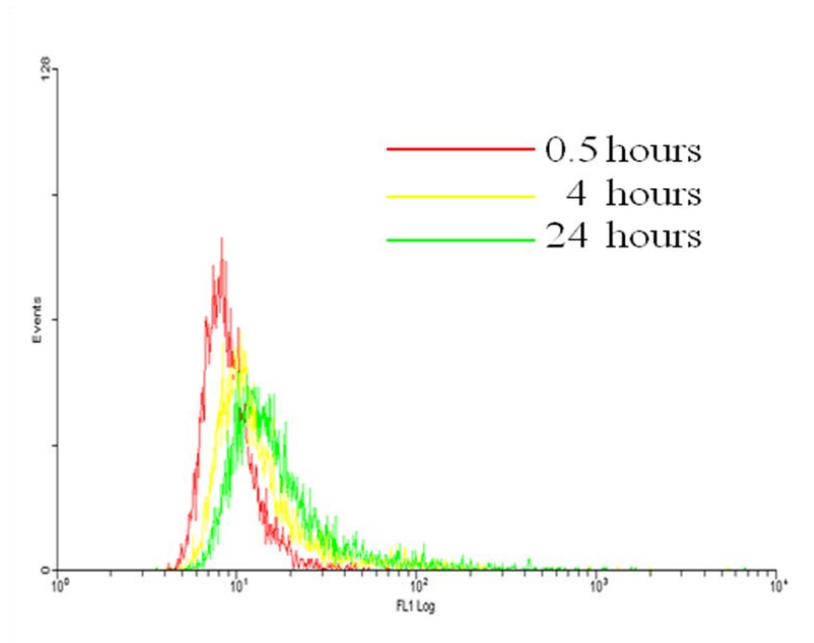


Figure 7.13 Fluorescence histograms of HHF-1 cells incubated with FA-SF/PPP nanoparticles for 0.5h, 4h and 24h

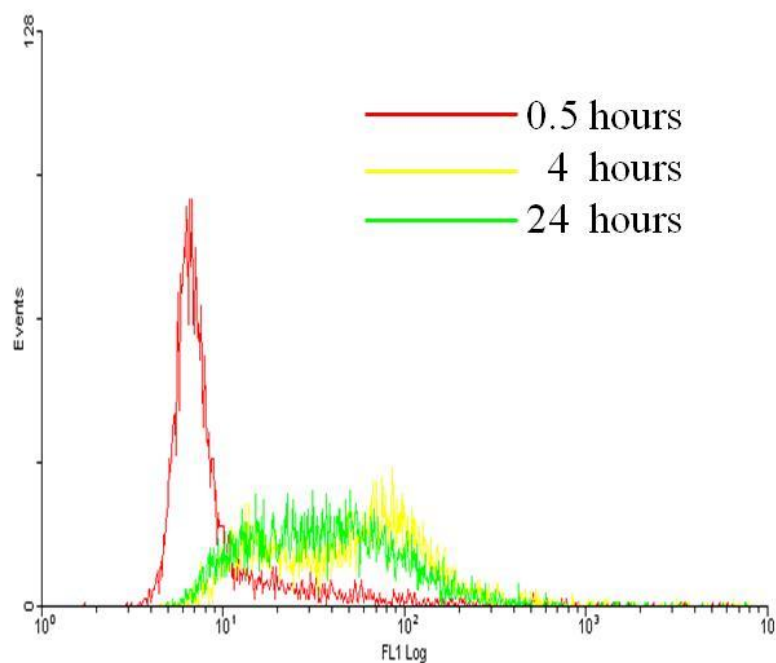


Figure 7.14 Fluorescence histograms of MCF-7 cells incubated with FA-SF/PPP nanoparticles for 0.5h, 4h and 24h

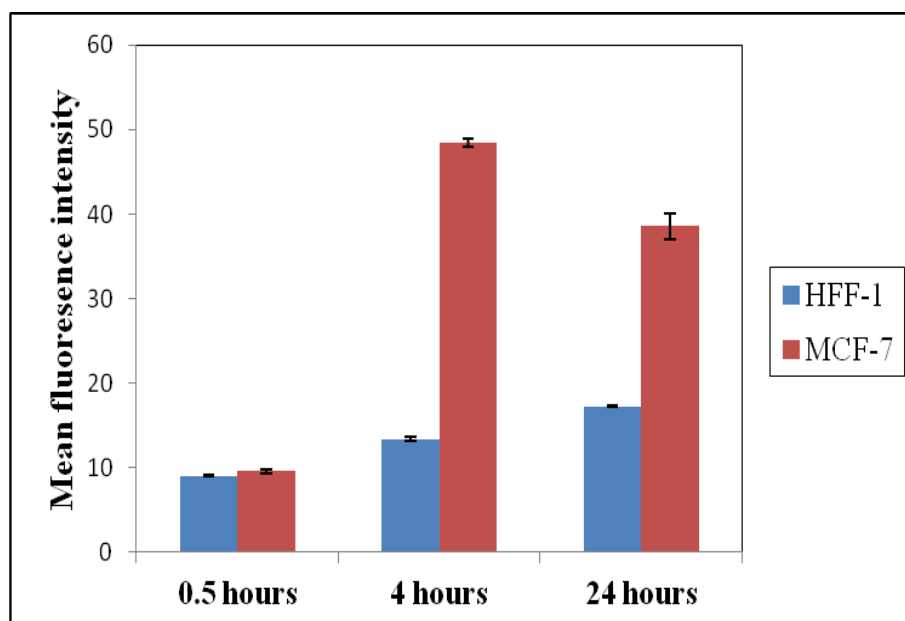


Figure 7.15 Cellular uptake of FA-SF/PPP nanoparticles by HFF-1 and MCF-7 cells for 0.5h, 4h and 24h

As shown in Figure 7.12, the fluorescence intensity of MCF-7 cells was significantly lower than that of HFF-1 cells after 30 minutes of incubation with SF/PPP nanoparticles. However, in the case of FA-SF/PPP, Figure 7.15 indicates that MCF-7 cells displays a higher the fluorescence intensity than HFF-1 cells. After 4 hours of incubation, fluorescence intensity of two kinds of nanoparticles internalized by MCF-7 cells is significantly higher than that internalized by HFF-1 cells. Table 7.1 summarizes the results about ratio of fluorescence intensity of nanoparticles in MCF-7 cells to that in HFF-1 cells at different incubation time (hours). Obviously, when incubation time increased from 0.5 hours to 4 hours, FA-SF/PPP nanoparticles possessed faster cellular uptake by MCF-7 cells than SF/PPP nanoparticles significantly ($p < 0.05$). Therefore, folic acid grafted on SF/PPP nanoparticles plays an important role to improve cellular uptake of SF/PPP nanoparticles against MCF-7 cells in a short time relatively.

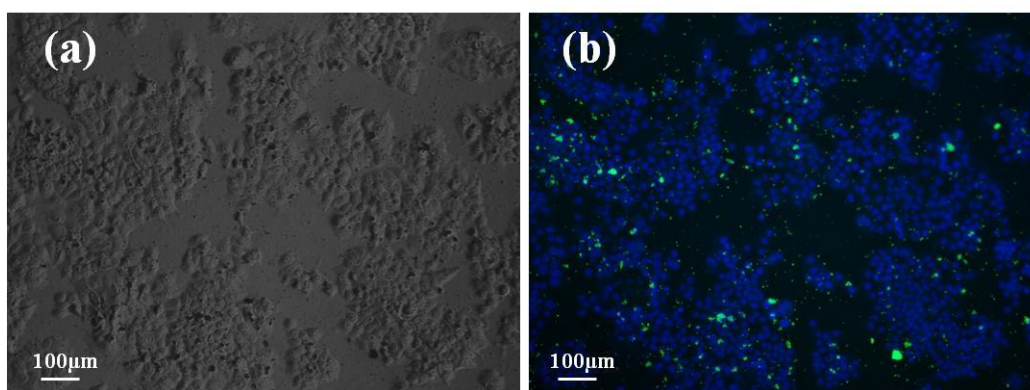


Figure 7.16 (a) DIC and (b) Fluorescence images of MCF-7 cells after 0.5h of incubation with SF/PPP nanoparticles

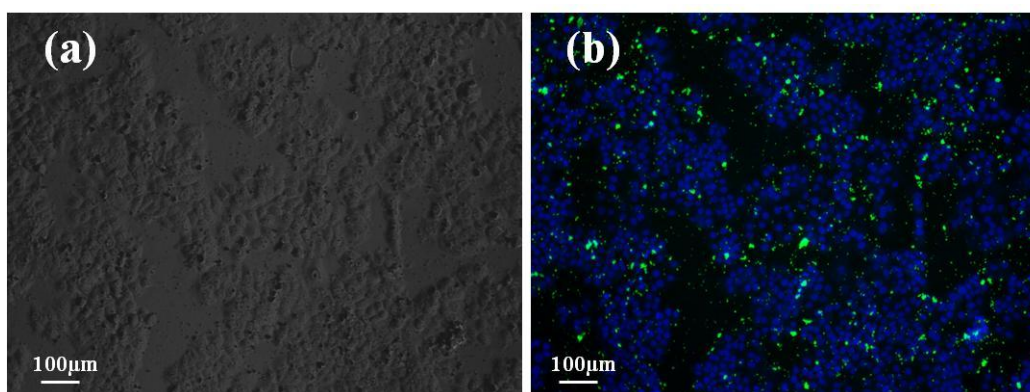


Figure 7.17(a) DIC and (b) Fluorescence images of MCF-7 cells after 0.5h of incubation with FA-SF/PPP nanoparticles

The fluorescence microscopy observation for MCF-7 cells incubated with SF/PPP and FA-SF/PPP nanoparticles for 0.5h shown in Figure 7.16 and Figure 7.17 also indicate that the fluorescence intensity of FA-SF/PPP nanoparticles in the MCF-7 cells was higher than that of SF/PPP nanoparticles. It must be noted that the ratio of amount of FA-SF/PPP nanoparticles internalized by MCF-7 cells to HFF-1 cells was higher than that of SF/PPP nanoparticles when incubation time was 4 hours and 24 hours for SF/PPP significantly ($p < 0.05$, shown in Table 7.1). It indicates that the enhanced cellular uptake of

FA-SF/PPP nanoparticles can maintain in a long period.

Table 7.1 The ratio of fluorescence intensity of nanoparticles in MCF-7 cells to that in HFF-1 cells at different incubation time (hours)

Nanoparticles	Incubation time			
	0.5 hours	4 hours	24 hours	
SF/PPP	0.75	1.675	1.31	Mean
	0.056	0.036	0.22	SD
FA-SF/PPP	1.06	3.64	2.24	Mean
	0.021	0.110	0.083	SD
<i>P</i> value	0.001	0.004	0.002	

Therefore, according to the results of flow cytometric analysis and fluorescence microscopy observation, it can be concluded that the cellular uptake of the SF/PPP into MCF-7 cells was improved using covalent conjugating folic acid (FA) to SF/PPP nanoparticles. Actually, the FA-SF/PPP nanoparticles were internalized into the MCF-7 cells via a folate receptor (FR)-mediated endocytosis because of high expression of FR on cells membrane of MCF-7 cells [190, 191]. In contrast, for HFF-1 cells without overexpressed folic acid receptors, the fluorescence intensity in cytoplasm displays a lower difference between the SF/PPP and FA-SF/PPP nanoparticles. The effective transportation of SF/PPP nanoparticles into cells may be mediated through a nonspecific endocytosis

process. Therefore, the FA-SF/PPP nanoparticles can be internalized into MCF-7 cancer cells through a folate receptor (FA)-mediated endocytosis mechanism and thus possess a tumor-specific targeting ability for the drug delivery.

7.7 *In vitro* cytotoxicity study

The flow cytometric analysis showed that folic acid modified SF/PPP (FA-SF/PPP) nanoparticles exhibited higher cellular uptake ability than SF/PPP nanoparticles by folic acid receptor-overexpressing cancer cells. Does the conjugation of folic acid to SF/PPP nanoparticles influence the transport of anti-tumor agents to cells? To investigate the issue, *in vitro* cytotoxicity of control, PTX-SF/PPP, PTX-FA-SF/PPP nanoparticles were compared using MCF-7 (FR⁺) and HFF-1 (FR⁻) as target cells. MTS assay described in Section 4.2.6 has been used to measure the *in vitro* cytotoxicity of samples. As presented in Chapter 6, SF/PPP nanoparticles as drug carrier showed relatively nontoxic to cells. Therefore, cytotoxicity of PTX loaded SF/PPP nanoparticles resulted from mostly PTX encapsulated in nanoparticles.

7.7.1 *In vitro* cytotoxicity to MCF-7 cells

Figure 7.18 indicates the cell viability of MCF-7 cells incubated with nanoparticles for 1, 2, 3, 5 and 7 days. As shown in Figure 7.18, two kinds of samples, including PTX-SF/PPP and PTX-FA-SF/PPP nanoparticles showed a time-dependent cytotoxicity to MCF-7 cells. With increase of incubation time to

seven days, the cell viability of MCF-7 cells incubated with PTX-SF/PPP and PTX-FA-SF/PPP nanoparticles was reduced to 27.9% and 30.3% respectively. However, there was no significant difference between cytotoxicity of PTX-SF/PPP and PTX-FA-SF/PPP nanoparticles after 7 days of incubation.

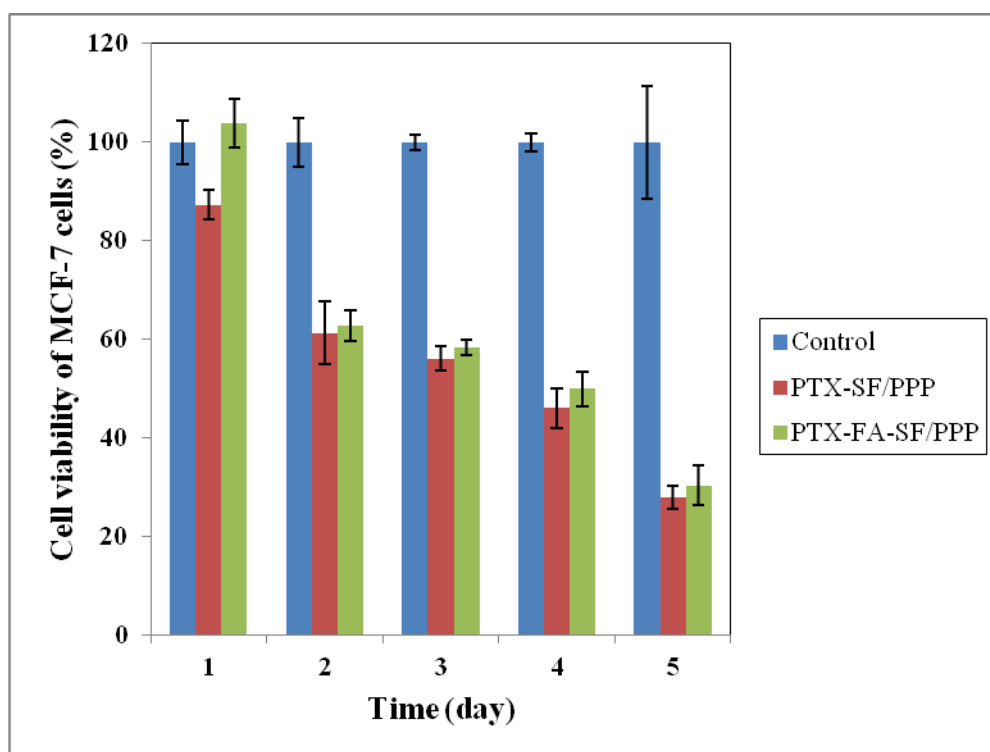


Figure 7.18 Cell viability of MCF-7 cells incubated with nanoparticles for 1, 2, 3, 5 and 7 days

The Live/dead assay shown in Figure 7.21 and Figure 7.22 also supported these results. Green cells and red cells were considered to be live cells and dead cells, respectively. After one day of incubation with PTX-SF/PPP and PTX-FA-SF/PPP nanoparticles, many dead cells have been observed.

Furthermore, the cell morphology changes of MCF-7 cells incubated with these two kinds of samples for 0, 1, 2, 3, 5 and 7 days were also investigated. As shown in Figure 7.19 (a) and Figure 7.20 (a), MCF-7 cells

displayed typical epithelial morphology before adding the PTX loaded nanoparticles. However, after the attachment ability of the cells became poor and a large number of cells floated, became round and brushed off with increase of incubation time to 7 days, a behavior consistent with cell death.

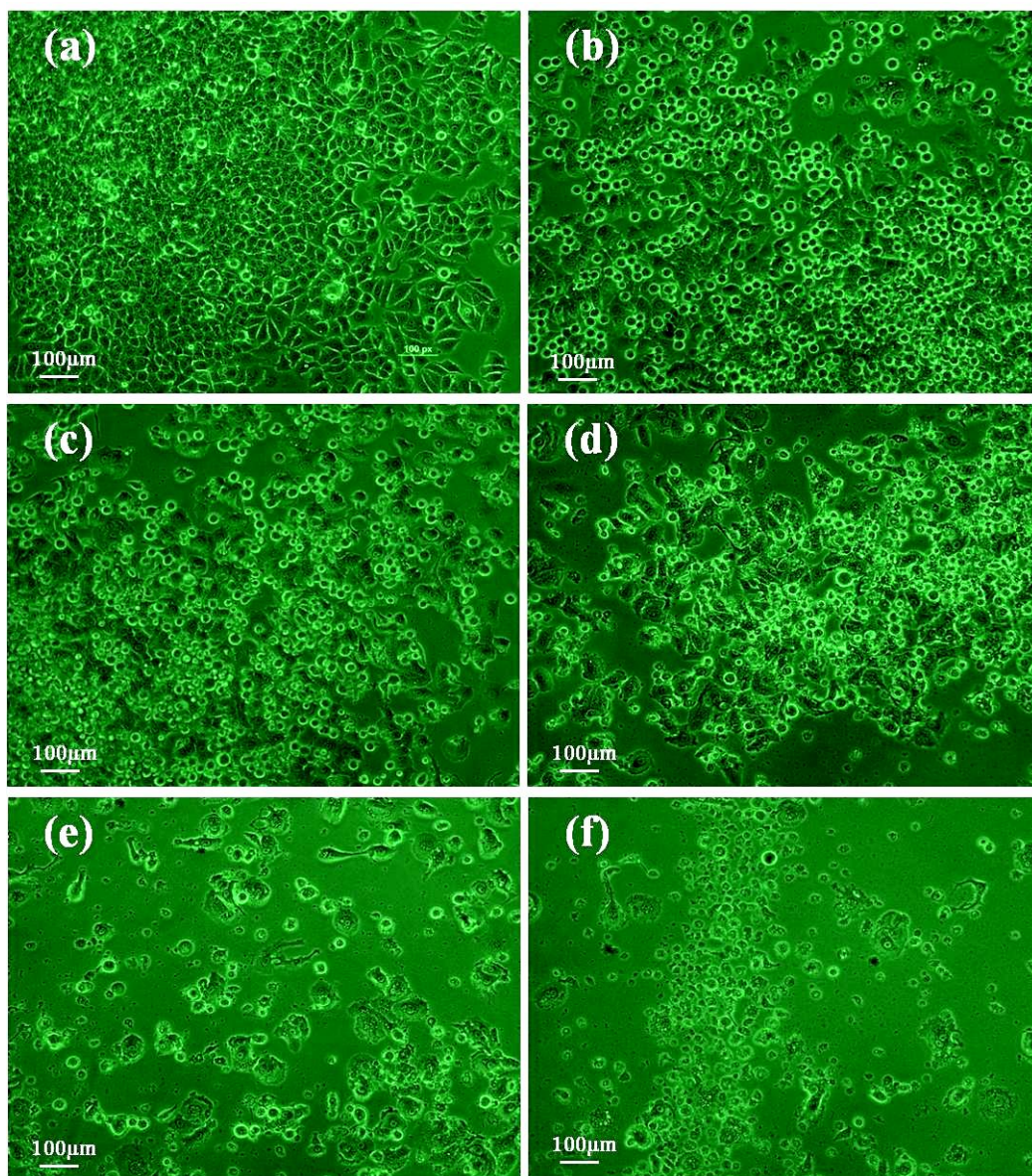


Figure 7.19 Optical images of MCF-7 cells incubated with PTX-FA-SF/PPP nanoparticles for (a) 0 day, (b) 1 day, (c) 2 days, (d) 3 days, (e) 5 days and (f) 7 days

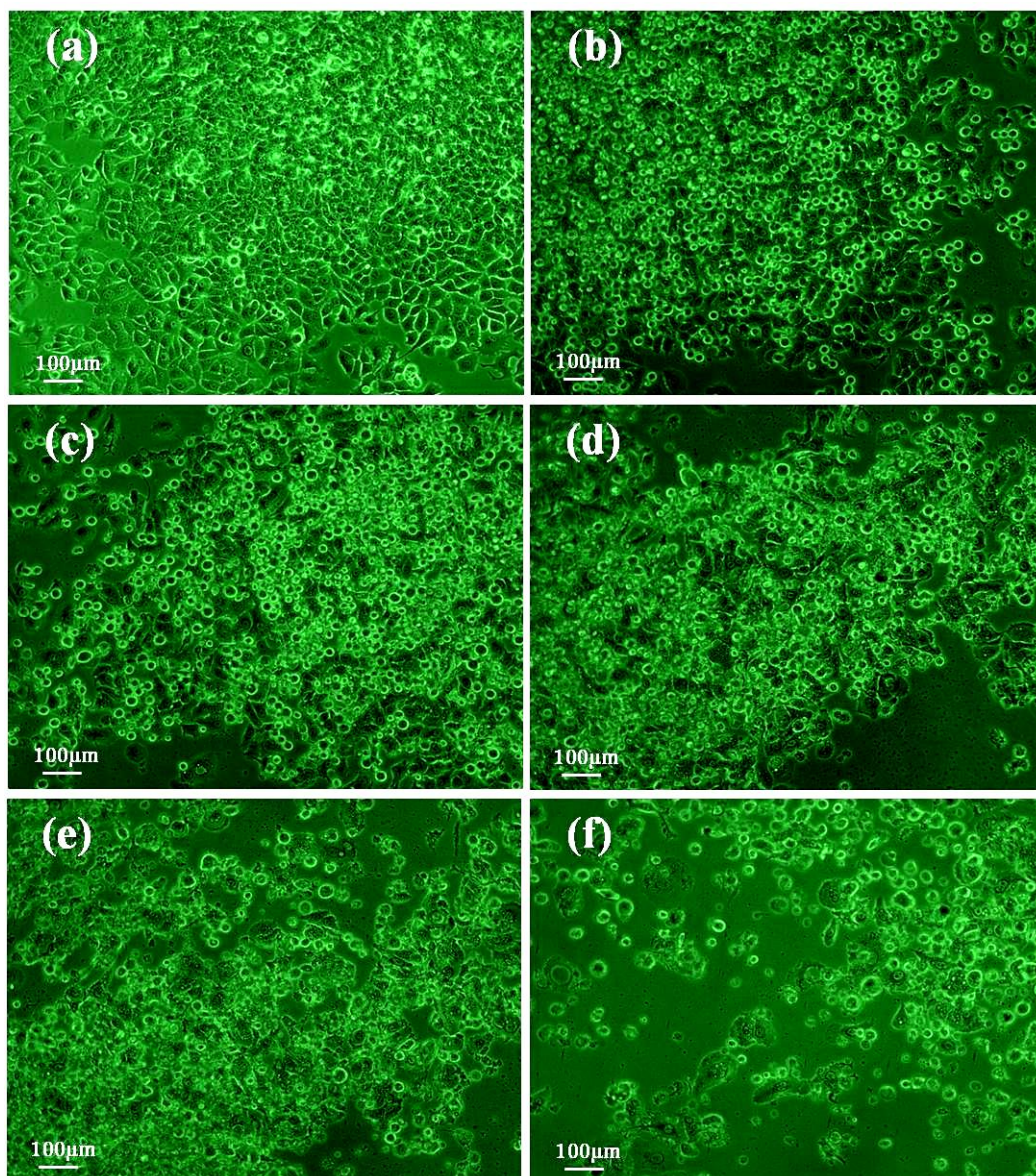


Figure 7.20 Optical images of MCF-7 cells incubated with PTX-SF/PPP nanoparticles for (a) 0 day, (b) 1 day, (c) 2 days, (d) 3 days, (e) 5 days and (f) 7 days

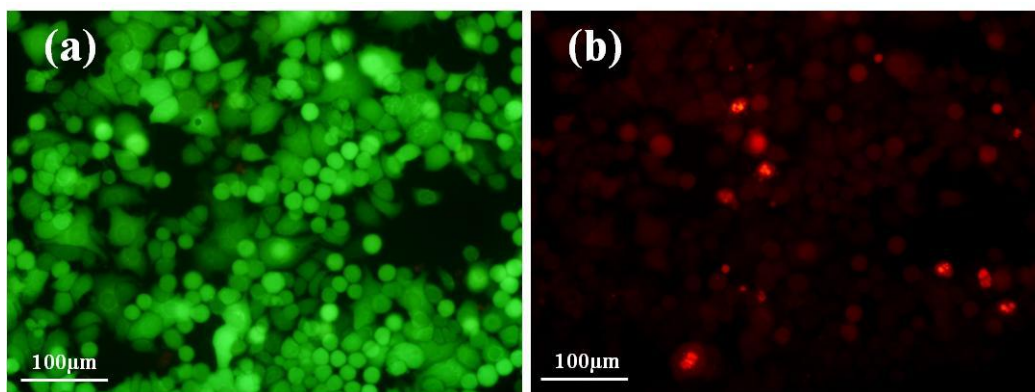


Figure 7.21 Live/Dead images of MCF-7 cells incubated with 0.5 µg/ml PTX-SF/PPP for 24 hours (a) live cell and (b) dead cells

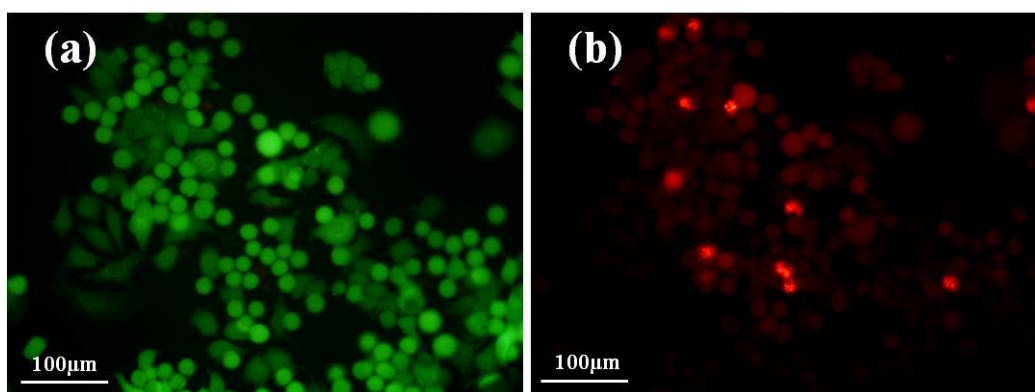


Figure 7.22 Live/Dead images of MCF-7 cells incubated with 0.5 µg/ml PTX-FA-SF/PPP for 24 hours (a) live cell and (b) dead cells

7.7.2 *In vitro* cytotoxicity to HFF-1 cells

The cytotoxicities of PTX-SF/PPP and PTX-FA-SF/PPP nanoparticles to HFF-1 cells were also studied. Figure 7.23 shows cell viability of HFF-1 cells incubated with nanoparticles for 1, 2, 3, 5 and 7 days. Obviously, cell viability of HFF-1 cells was reduced to 47.6% and 44.1% respectively after 7 days of incubation with PTX-SF/PPP and PTX-FA-SF/PPP nanoparticles respectively. These results were also supported by the morphology changes of HFF-1 cells in

the process of incubation with PTX-SF/PPP and PTX-FA-SF/PPP nanoparticles. As shown in Figure 7.24, before incubation, HFF-1 cells exhibited typical fibroblast morphology. However, when incubation time increased to 7 day, a large number of cells floated, brushed off, and became round, a behavior consistent with cell death. In general, cytotoxicity of PTX-FA-SF/PPP nanoparticles is slightly higher than PTX-SF/PPP nanoparticles after 7 days incubation. However, the significant difference of cytotoxicity between PTX-SF/PPP and PTX-FA-SF/PPP nanoparticles was not observed.

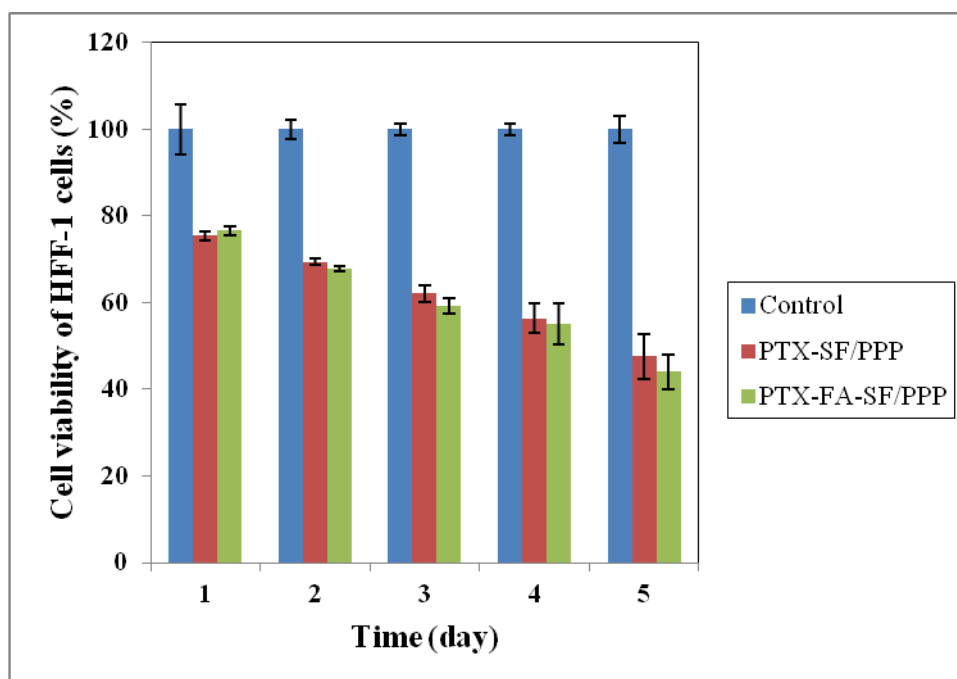


Figure 7.23 Cell viability of HFF-1 cells incubated with nanoparticles for 1, 2, 3, 5 and 7 days

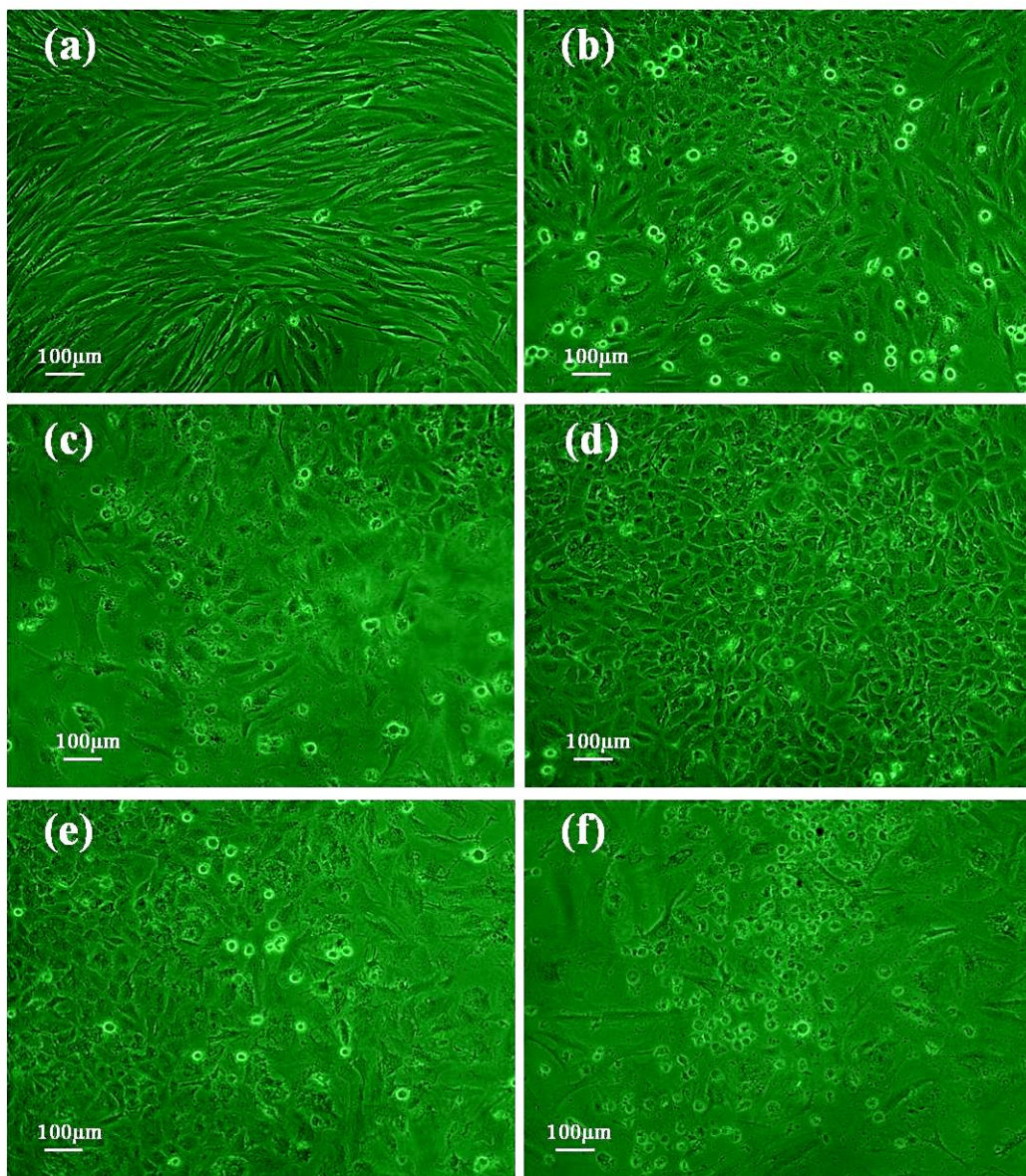


Figure 7.24 Optical images of HFF-1 cells incubated with PTX-FA-SF/PPP nanoparticles for (a) 0 day, (b) 1 day, (c) 2 days, (d) 3 days, (e) 5 days and (f) 7 days

7.7.3 Comparison of cytotoxicity to MCF-7 and HFF-1 cells

In this study, MCF-7 cells with overexpressed folate receptors and HFF-1 cells without overexpressed folate receptors was chosen as a tumor cells

model and normal cells model respectively. The study on difference of cytotoxicity between MCF-7 and HFF-1 cells can help understand the delivery of anticancer agents to cells. As shown in Figure 7.18, PTX-load nanoparticles including PTX-SF/PPP and PTX-FA-SF/PPP nanoparticles caused a $72.1\% \pm 2.4\%$ and $69.6\% \pm 4.1\%$ decrease in the cell viability of MCF-7 cells respectively. However, cell viability of HFF-1 cells incubated with PTX-SF/PPP and PTX-FA-SF/PPP nanoparticles decreased by $52.4\% \pm 5.1\%$ and $55.9\% \pm 4\%$ respectively. Therefore, PTX loaded nanoparticles exhibited higher cytotoxicity to MCF-7 than to HFF-1 cells after one week of incubation significantly ($p < 0.05$). The result will be beneficial to the tumor therapy and reduce the damage to normal cells.

Besides, it should be noted that cell viability of MCF-7 cell incubated with PTX-SF/PPP nanoparticles was lower than that incubated with PTX-FA-SF/PPP nanoparticles for one day. Moreover, according to the results of *in vitro* cytotoxicity in Chapter 6, the PTX-SF/PPP nanoparticles possessed a lower cytotoxicity to MCF-7 than free PTX after one day of incubation. It might result from two possible reasons. On one hand, under *in vitro* conditions, free PTX was transported into the MCF-7 cells more efficiently than PTX-SF/PPP nanoparticles, which are taken up by cells through endocytosis. On the other hand, free PTX is effective once it enters cells, while the PTX encapsulated in SF/PPP nanoparticles need escape from endosome/lysosome pathway for endocytosis and be released in a controlled way [188, 189]. As PTX-SF/PPP

nanoparticles possessed a faster drug release rate than free PTX *in vitro*, it is probably that PTX-SF/PPP nanoparticles can be internalized by MCF-7 cells faster than free PTX. Therefore, the process of endosome escape will inhibit the cytotoxicity of PTX-SF/PPP nanoparticles. However, in a long period, more PTX-SF/PPP nanoparticles were internalized and PTX can be released from PTX-SF/PPP nanoparticles to inhibit the cell viability of MCF-7 in a stable way.

Here, PTX-SF/PPP nanoparticles displayed a higher cytotoxicity to MCF-7 cells than PTX-FA-SF/PPP nanoparticles after one day of incubation. According to the analysis above, PTX-FA-SF/PPP could possess faster cellular uptake by MCF-7 cells than PTX-SF/PPP nanoparticles. Moreover, faster internalization should result from folate-mediated specific endocytosis. The results were also supported by the results of flow cytometric analysis.

In contrast, the cytotoxicity of PTX-SF/PPP and PTX-FA-SF/PPP to HFF-1 cells has no obvious difference after one day of incubation. It can be concluded that HFF-1 without overexpressed folate receptors can not mediate a folate-specific cellular uptake of PTX-SF/PPP and PTX-FA-SF/PPP. Therefore, the cellular uptake of PTX-SF/PPP and PTX-FA-SF/PPP nanoparticles has no obvious difference and thus similar anti-tumor ability was observed.

In summary, the different cytotoxicity between HFF-1 and MCF-7 cells indicated that PTX-FA-SF/PPP nanoparticles possessed faster cellular uptake by MCF-7 cells than PTX-SF/PPP and folic acid (FA) on PTX-FA-SF/PPP improved the tumor-specific cellular uptake. Therefore, PTX-FA-SF/PPP nanoparticles can

be used as smart drug delivery system for tumor-targeted therapy.

7.8 Summary

In this Chapter, folic acid was conjugated on the surface of PTX-SF/PPP nanoparticles successfully. The result of UV-Vis spectra analysis indicated that the folic acid (FA) content was about 0.01669 mg/10 mg PTX-FA-SF-PPP nanoparticles. Folic acid modification and freeze drying reduced the PTX content. And the drug load and encapsulation efficiency of PTX-FA-SF/PPP nanoparticles decreased to 15.5% and 77.4% from 18.1% and 90.6% respectively. Moreover, PTX could be released from PTX-FA-SF/PPP nanoparticles in a controlled way. The cumulative release of PTX increased to 27.8% and 21.3% in PBS buffer (pH 6.0) and PBS buffer (pH 7.4) respectively in one week. Flow cytometric analysis and the fluorescence microscopy observation indicated that FA-SF/PPP nanoparticles exhibited a higher cellular uptake ability than SF/PPP nanoparticles and can be internalized into tumour cells via a folate-receptor-mediated endocytosis mechanism and thus possessed a tumour-specific targeting ability for the delivery of drugs. *In vitro* cytotoxicity studies indicated that PTX-FA-SF/PPP nanoparticles showed a time-dependent cytotoxicity and can treat tumour cells effectively. Therefore PTX-FA-SF/PPP nanoparticles could be utilized as a smart drug delivery system for tumour-targeted therapy.

Chapter 8 Conclusion and suggestions for future work

8.1 Conclusion

The development of novel nanoparticle drug delivery systems via green nanotechnology is critical to enhance drug bioavailability and reduce the severity of side-effects during the administration of drugs in the biomedical field, especially for tumor therapy. In Chapter 2, the fundamental knowledge framework of silk fibroin-based nanoparticle drug delivery systems for tumor therapy was reviewed and knowledge gaps identified. The purpose of this research was to fill the knowledge gaps and develop a silk fibroin-based nanoparticle drug delivery system by supercritical CO₂ technology to treat tumors. This purpose was achieved by completing the five objectives identified in Chapter 1 as summarized in the following aspects.

1. To prepare silk fibroin nanoparticles of small particle size and excellent biocompatibility by novel nanotechnology. This objective was achieved in Chapter 3. Solution-enhanced dispersion by supercritical CO₂ (SEDS) was firstly used to successfully prepare silk fibroin nanoparticles with particle sizes from 52.5 nm to 102.3 nm and particle size distribution (span) from 0.32 to 0.66. Meanwhile, the investigation using 24 full factorial design indicated that increasing the concentration and the flow rate of silk fibroin solution and precipitation temperature raised the particle size and particle size distribution of silk fibroin nanoparticles, while reducing the precipitation pressure decreased the

particle size and particle size distribution. The optimized process parameters to produce silk fibroin nanoparticles can be described as follows (P: 20 MPa, T: 35 °C; Concentration of solution: 0.5%; Flow rates of solution: 0.5 ml min⁻¹, respectively). Based on the analysis of the effect of process parameters on particle size, a possible silk fibroin nanoparticle formation mechanism was proposed based on the formation and growth of silk fibroin nuclei in the gaseous miscible phase evolved from initial droplets generated by a liquid-liquid phase split. The mutual mass transfer between supercritical CO₂ (scCO₂) and solution superimposed on the supersaturation was the most important process parameter to affect nanoparticle formation.

2. To characterize silk fibroin (SF) nanoparticles prepared by the SEDS process and explore its application in drug delivery systems. This objective was achieved in Chapter 4. The results indicated that the SF nanoparticles prepared by the SEDS process exhibited excellent biocompatibility and time and concentration-dependent cellular uptake properties. A PTX and IDMC loading experiment suggested that the drug load (DL) and encapsulation efficiency (EE) of PTX-SF and IDMC-SF nanoparticles were about 19.86% and 99.32%, and 6.11% and 30.52% respectively. Different DL and EE for two kinds of drug encapsulated by SF nanoparticles may have resulted from different precipitation kinetics in the SEDS process. After the ethanol treatment, DL and EE of IDMC-SF nanoparticles decreased to 2.05% and 10.23%. However, almost all PTX was lost. An *in vitro* drug release experiment indicated that the

accumulative release of IDMC from IDMC-SF nanoparticles was 61.15% after 6 h and reached 87% after 24 h. The drug release then reached a plateau and only 5% more of the drug was released over the next 24 h. Obviously there is no burst effect and the drug is released in a stable way. In a word, the SF nanoparticles fabricated by the SEDS process are a potential drug carrier to be used in biomedical field.

3. To develop a novel SF/PPP nanoparticle drug carrier to overcome the shortcomings of natural SF and synthetic PLLA-PEG-PLLA (PPP) polymer in supercritical CO₂. This objective was achieved in Chapter 5. In this study, SF/PPP nanoparticles with mean particle size of 634.1 ± 173.7 nm were successfully fabricated by a modified SEDS process, in which a stainless steel cylinder container with a piston was designed as “injector” and could deliver a suspension composed of silk fibroin nanoparticles and PPP solution to avoid obstruction of the pump and delivery system. SEM and TEM images indicated that the silk fibroin nanoparticles were dispersed on the PPP nanoparticles. FTIR analysis indicated that the composite nanoparticles consist of silk fibroin and PPP polymer. The results of XRD indicated that the SEDS process reduced the crystalline state of products. The MTS assay indicated that SF/PPP nanoparticles possess much better biocompatibility and faster cell adhesion and internalization ability compared with PPP nanoparticles. In conclusion, SF/PPP nanoparticles prepared by the SEDS process could be used as potential biomaterials in the biomedical field, especially nanoparticle drug delivery systems.

4. To encapsulate PTX using SF/PPP nanoparticles by the SEDS process and study the anti-tumor activity of PTX loaded SF/PPP nanoparticles *in vitro*. This objective was achieved in Chapter 6. The resulting PTX loaded SF/PPP (PTX-SF/PPP) nanoparticles with mean particle size of 650.6 ± 158.8 nm do not need induction of water insolubility and avoid the drug loss of PTX loaded silk fibroin nanoparticles in post-treatment. PTX-SF/PPP nanoparticles enhanced the solubility of PTX exhibiting a controlled drug release. Especially the drug release rate in PBS solution could be accelerated with decrease of pH value from 7.4 to 6.0. This property can benefit tumor-specific therapy due to the unique tumor environment. *In vitro* cytotoxicity assay for MCF-7 cells and HePG-2 cells indicated that PTX-SF/PPP nanoparticles had a slightly higher cytotoxicity after one week than that of free PTX. However, the difference was not significant. In terms of the characteristics of nanoparticles, PTX-SF/PPP nanoparticles have potential application in the field of tumor therapy.

5. To develop smart folic acid grafted PTX-/SF/PPP nanoparticles for tumor-targeted therapy. This objective was achieved in Chapter 7. The mean particle size of PTX-SF/PPP nanoparticles is 665.4 ± 200.6 nm. The analysis of the UV-Vis spectra of pancreatin hydrolysates of PTX-SF/PPP nanoparticles and PTX-FA-SF/PPP nanoparticles indicated the content of folic acid (FA) grafted on the PTX-SF/PPP nanoparticles was about 0.01669 mg/10 mg of PTX-FA-SF-PPP nanoparticles. Folic acid modification and freeze drying reduced the PTX content. And the drug load and encapsulation efficiency of PTX-FA-SF/PPP nanoparticles

decreased to 15.5% and 77.4% from 18.1% and 90.6% respectively. Moreover, PTX can be released from PTX-FA-SF/PPP nanoparticles in a sustained way. The cumulative release of PTX increased to 27.8% and 21.3% in pH 7.4 and pH 6.0 PBS buffer respectively. The flow cytometric analysis showed that the FA-SF/PPP possessed a higher cellular uptake by MCF-7 tumor cells than SF/PPP nanoparticles. However, the MTS assay indicated that *in vitro* anti-tumor activity had no significant difference between PTX-loaded FA-SF/PPP and PTX-loaded SF/PPP nanoparticles. In terms of tumor-targeted delivery and high drug load and controlled drug release properties, the PTX-FA-SF/PPP nanoparticles could be utilized as an effective drug delivery system for tumor-targeted therapy.

8.2 Suggestions for future research

Although the objectives of this thesis have been achieved, there are unavoidable limitations to the current research work that ideally need further investigation.

1. Silk fibroin nanoparticles prepared by the SEDS process are water-soluble natural biopolymers with excellent biocompatibility. In the present study, IDMC and PTX were chosen as the drug model. IDMC and PTX loaded nanoparticles could be prepared successfully. However, drug leakage occurs and a large number of drugs have been lost in the process of water-insoluble induction by ethanol treatment. Therefore, to choose suitable drugs, especially

anti-cancer drugs to avoid drug leakage caused by ethanol treatment will be very necessary.

2. Improvement of supercritical antisolvent (CO₂) apparatus: In chapter 5, a particle suspension delivery system was introduced to deliver suspension solution which included silk fibroin nanoparticles and PLLA-PEG-PLLA (PPP) into the high-pressure vessel. However, silk fibroin nanoparticles are difficult to be dispersed into DCM solution containing PPP polymer over a long time period. Therefore, the SF/PPP nanoparticles prepared by the SEDS process cannot exhibit regular spherical shape. The improvement of supercritical antisolvent (CO₂) apparatus such as setting up an ultrasonic energy near samples will be useful to obtain a homogenous nanoparticle suspension solution and prepare composite nanoparticles. Moreover, more studies about designing novel nozzles and how to decrease the particle size of SF/PPP nanoparticles is very necessary because particles of small size can enhance the cellular uptake and tumor targeting behaviour via the EPR effect.

3. Two kinds of methods shown in Chapter 5 were used to prepare silk fibroin /PLLA-PEG-PLLA (SF/PPP) composite nanoparticles. Particularly, a homogenous solution including SF and PPP polymers were used to prepare SF/PPP nanoparticles. However, no SF/PPP composite nanoparticles formed. Future work can focus on selecting suitable synthetic polymers to combine with silk fibroin to prepare natural SF/synthetic polymer composite nanoparticles by the SEDS process.

4. An animal model was suggested to evaluate the *in vivo* anti-tumor activity. There existed a significantly different environment between *in vitro* and *in vivo*. Even though PTX-loaded SF/PPP and FA-SF/PPP nanoparticles displayed sustained drug release properties and noticeable anti-tumor efficacy *in vitro*, it is highly recommended to conduct further experiments using *in vivo* animal models. For example, pharmacokinetic and biodistribution studies can be used to evaluate the blood circulating levels of nanoparticles and the effect of passive tumor targeting (EPR effect). Compared to *in vitro* cytotoxicity, *in vivo* anti-tumor activity in animal models can exhibit a more realistic therapeutic efficacy of PTX-loaded nanoparticles against cancer. The relevant work will be investigated in future work.

References

- [1] Park JH, von Maltzahn G, Xu MJ. Cooperative nanomaterial system to sensitize, target, and treat tumors. *Proc Natl Acad Sci USA* 2010; 107: 981-986.
- [2] Ahmad MZ, Akhter S, Jain GK, Rahman M, Pathan SA, Ahmad FJ, Khar RK. Metallic nanoparticles: technology overview & drug delivery applications in oncology. *Expert Opin Drug Deliv* 2010; 7: 927-942.
- [3] Knobloch T, Sithisarn P, Cinatl J Jr, Kreuter J. Interaction of folate-conjugated human serum albumin (HSA) nanoparticles with tumour cells. *Int J Pharm* 2011; 406: 128-134.
- [4] Freiberg S, Zhu XX. Polymer microspheres for controlled drug release. *Int J Pharm* 2004; 282: 1-18.
- [5] Danhier F, Feron O, Pr at V. To exploit the tumor microenvironment: Passive and active tumor targeting of nanocarriers for anti-cancer drug delivery. *J Control Release* 2010; 148: 135-146.
- [6] Gobin AS, Rhea R, Newman RA, Mathur A. Silk fibroin coated liposomes for long-term and targeted drug delivery. *Int J Nanomedicine* 2006; 1: 81-87.
- [7] Yeo JH, Lee KG, Lee YW, Kim SY. Simple preparation and characteristics of silk fibroin microsphere. *Eur Polym J* 2003; 39: 1195-1199.
- [8] Kundu J, Patra C, Kundu S C. Design, fabrication and characterization of silk fibroin-HPMC-PEG blended films as vehicle for transmucosal delivery. *Mater Sci Eng C* 2008; 28: 1376-1380.

- [9] Nazarov R, Jin HJ, Kaplan DL. Porous 3D scaffolds from regenerated silk fibroin. *Biomacromolecules* 2004; 5: 718-726.
- [10] Kim UJ, Park J, Li C, Jin HJ, Valluzzi R, Kaplan DL. Structure and properties of silk hydrogels. *Biomacromolecules* 2004; 5: 786-792.
- [11] Zhang F, Zuo B, Bai L. Study on the structure of SF fiber mats electrospun with HFIP and FA and cells behavior. *J Mater Sci* 2009; 44: 5682-5687.
- [12] Wenk E, Wandrey AJ, Merkle HP, Meinel L. Silk fibroin spheres as a platform for controlled drug delivery. *J Control Release* 2008; 132: 26-34.
- [13] Silva SS, Santos TC, Cerqueira MT, Marques AP, Reys LL, Silva TH, Caridade SG, Mano JF and Reis RL The use of ionic liquids in the processing of chitosan/silk hydrogels for biomedical applications. *Green Chem* 2012; 14: 1463-1470.
- [14] Dyakonov T, Yang CH, Bush D, Gosangari S, Majuru S, Fatmi A. Design and characterization of a silk-fibroin-based drug delivery platform using Naproxen as a model drug. *J Drug Deliv* 2012; 2012: 490514. doi:10.1155/2012/490514.
- [15] Yang X, Chen Y, Yuan R, Chen G, Blanco E, Gao J, Shuai X. Folate-encoded and Fe₃O₄-loaded polymeric micelles for dual targeting of cancer cells. *Polymer* 2008; 49: 3477-3485.
- [16] Daniels TR, Delgado T, Helguera G, Penichet ML. The transferrin receptor part II: targeted delivery of therapeutic agents into cancer cells. *Clin Immunol* 2006; 121: 159-176.

- [17]van Vlerken LE, Amiji MM. Multi-functional polymeric nanoparticles for tumour-targeted drug delivery. *Expert Opin Drug Deliv* 2006; 3: 205-216.
- [18]Minamimura T, Sato H, Kasaoka S, Saito T, Ishizawa S, Takemori S, Tazawa K, Tsukada K. Tumor regression by inductive hyperthermia combined with hepatic embolization using dextran magnetite-incorporated microspheres in rats. *Int J Oncol* 2000; 16: 1153-1158.
- [19]Pyo D. Two different shapes of insulin nanoparticles produced by solution enhanced dispersion supercritical fluid (SEDS) process. *Bull Korean Chem Soc* 2009; 30: 1215-1217.
- [20]Zhao Z, Li Y, Chen AZ, Zheng ZJ, Hu JY, Li JS, Li G. Generation of silk fibroin nanoparticles via solution-enhanced dispersion by supercritical CO₂. *Ind Eng Chem Res* 2013; 52: 3752-3761.
- [21]Kang YQ, Wu J, Yin GF, Huang ZB, Yao YD, Liao XM, Chen AZ, Pu XM. Preparation, characterization and *in vitro* cytotoxicity of indomethacin-loaded PLLA/PLGA nanoparticles using supercritical CO₂ technique. *Eur J Pharm Biopharm* 2008; 70: 85-97.
- [22]Egusquiaguirre SP, Igartua M, Hernández RM, Pedraz JL. Nanoparticle delivery systems for cancer therapy: advances in clinical and preclinical research. *Clin Transl Oncol* 2012; 14: 83-93.
- [23]Zhang J, Lan CQ, Post M, Simard B, Deslandes Y, and Hsieh TH. Design of nanoparticles as drug carriers for cancer therapy. *Cancer, Genomics & Proteomics* 2006; 3: 147-157.

- [24]Scheithauer W, Kornek G, Zeh B. Palliative chemotherapy versus supportive care in patients with metastatic gastric cancer: a randomized trial. Proceedings of the Second International Conference on Biology, Prevention and Treatment of GI Malignancy. Koln, Germany, 1995; 68.
- [25]Glimelius B, Ekstrom K, Hoffman K et al. Randomized comparison between chemotherapy plus best supportive care with best supportive care in advanced gastric cancer. *Ann Oncol* 1997; 8: 163-168.
- [26]Reynolds AR, Moghimi SM and Hodiwalla-Dilke K. Nanoparticle mediated gene delivery to tumor vasculature. *Trends Mol Med* 2003; 9: 2-4.
- [27]Kreuter J. Nanoparticles as drug delivery systems. *Encyclopedia of Nanoscience and Nanotechnology* 2004; 7: 161-180.
- [28]Birrenbach G, Speiser, PP. Polymerized micelles and their use as adjuvants in immunology. *J Pharm Sci* 1976; 65: 1763-1766
- [29]Maeda H, Wu J, Sawa T, Matsumura Y, Hori K. Tumor vascular permeability and the EPR effect in macromolecular therapeutics: a review. *J Control Release* 2000; 65:271-284.
- [30]Yu MK, Park J, Jon S. Targeting strategies for multifunctional nanoparticles in cancer imaging and therapy. *Theranostics* 2012; 2: 3-44.
- [31]Jain RK, Stylianopoulos T. Delivering nanomedicine to solid tumors. *Nat Rev Clin Oncol* 2010; 7: 653-664.
- [32]Jang SH, Wientjes MG, Lu D, Au JL. Drug delivery and transport to solid tumors. *Pharm Res* 2003; 20:1337-1350.

- [33] Wang AZ, Langer R, Farokhzad OC. Nanoparticle delivery of cancer drugs. *Annu Rev Med* 2012; 63: 185-198.
- [34] Matsumura Y, Maeda H. A new concept for macromolecular therapeutics in cancer chemotherapy: mechanism of tumoritropic accumulation of proteins and the antitumor agent smancs. *Cancer Res* 1986; 46: 6387-6392.
- [35] Xu J, Ganesh S, Amiji M. Non-condensing polymeric nanoparticles for targeted gene and siRNA delivery. *Int J Pharm* 2012; 427: 21-34.
- [36] Patel RR, Patel JK. Novel technologies of oral controlled release drug delivery system. *Syst Rev Pharm* 2010; 1: 128-132.
- [37] Dey NS, Majumdar S, Rao MEB, Multiparticulate drug delivery systems for controlled release. *Trop J Pharm Res* 2008; 7: 1067-1075.
- [38] Varde NK, Pack DW. Microspheres for controlled release drug delivery. *Expert Opin Biol Ther* 2004; 4: 35-51.
- [39] Hu CM, Aryal S, Zhang L. Nanoparticle-assisted combination therapies for effective cancer treatment. *Ther Deliv* 2010; 1: 323-334.
- [40] Cho K, Wang X, Nie S, Chen ZG, Shin DM. Therapeutic nanoparticles for drug delivery in cancer. *Clin Cancer Res* 2008; 14: 1310-1316.
- [41] Alexis F, Pridgen EM, Langer R, Farokhzad OC. Nanoparticle technologies for cancer therapy. *Handb Exp Pharmacol* 2010; 197: 55-86.
- [42] Markman M. Pegylated liposomal doxorubicin in the treatment of cancers of the breast and ovary. *Expert Opin Pharmacother* 2006; 7: 1469-1474.

- [43]Rivera E. Current status of liposomal anthracycline therapy in metastatic breast cancer. *Clin Breast Cancer* 2003; 4:S76-83.
- [44]Rosenthal E, Poizot-Martin I, Saint-Marc T, Spano JP, Cacoub P, Group DNXS. Phase IV study of liposomal daunorubicin (DaunoXome) in AIDS-related Kaposi sarcoma. *Am J Clin Oncol* 2002; 25: 57-59.
- [45]Gibson JD, Khanal BP, Zubarev ER. Paclitaxel-functionalized gold nanoparticles. *J Am Chem Soc* 2007; 129: 11653-11661.
- [46]Hwu JR, Lin YS, Josephrajan T, Hsu MH, Cheng FY, Yeh CS, Su WC, Shieh DB. Targeted paclitaxel by conjugation to iron oxide and gold nanoparticles. *J Am Chem Soc* 2009; 131: 66-68.
- [47]Conde J, Doria G, Baptista P. Noble metal nanoparticles applications in cancer. *J Drug Deliv.* 2012; 2012:751075. doi: 10.1155/2012/751075.
- [48]Kim TY, Kim DW, Chung JY, et al. Phase I and pharmacokinetic study of Genexol-PM, a cremophor-free, polymeric micelle-formulated paclitaxel, in patients with advanced malignancies. *Clin Cancer Res* 2004; 10: 3708–3716.
- [49]Baker JR Jr. Dendrimer-based nanoparticles for cancer therapy. *Hematology Am Soc Hematol Educ Program* 2009:708-719.
- [50]Yokoyama M, Kwon GS, Okano T, Sakurai Y, Seto T, Kataoka K. Preparation of micelle-forming polymer-drug conjugates. *Bioconjug Chem* 1992; 3: 295-301.
- [51]Sudhir SC, Dennis HR, and Sinjan D. Nanoparticles prepared using natural and synthetic polymers. *Nanoparticulate Drug Delivery Systems*.2007; 3:

51-59.

- [52]Edlund U. and Albertsson AC. Degradable polymer microspheres for controlled drug delivery. *Adv Polym Sci* 2002; 157: 67-112.
- [53]Jahanshahi .M, Babaei Z. Protein nanoparticle: A unique system as drug delivery vehicles. *Afr J of Biotechnol* 2008; 7: 4926-4934.
- [54]Hawkins MJ, Soon-Shiong P, Desai N. Protein nanoparticles as drug carriers in clinical medicine. *Adv. Drug Deliv Rev* 2008; 60:876-885
- [55]Jahanshahi M, Sanati MH, Hajizadeh S, Babaei Z. Gelatin nanoparticles fabrication and optimization of the particle size. *Physica status solidi (a)* 2008; 205: 2898-2902.
- [56]Massimiliano P, Valentina P, Giuseppe M, Giuseppe A, Emanuela G, Gianluca Q, Maurizio F, Marco DS. Controlled self assembly of collagen nanoparticle. *J Nanopart Res* 2011; 13:6141-6147.
- [57]Gradishar WJ, Tjulandin S, Davidson N, et al. Phase III trial of nanoparticle albumin-bound paclitaxel compared with polyethylated castor oil-based paclitaxel in women with breast cancer. *J Clin Oncol* 2005; 23: 7794-7803.
- [58]Kundu J, Chung YI, Kim YH, Tae G, Kundu SC. Silk fibroin nanoparticles for cellular uptake and control release. *Int J Pharm* 2010; 388: 242-250.
- [59]Unger RE, Wolf M, Peters K, Motta A, Migliaresi C, James Kirkpatrick C. Growth of human cells on a non-woven silk fibroin net: a potential for use in tissue engineering. *Biomaterials* 2004; 25: 1069-1075.
- [60]Yoshimizu H, Asakura T. Preparation and characterization of silk fibroin

- powder and its application to enzyme immobilization. *J Appl Polym Sci* 1990; 40: 127-134.
- [61]Minoura N, Aiba S, Gotoh Y, Tsukada M, Imai Y. Attachment and growth of cultured fibroblast cells on silk protein matrices. *J Biol Mater Res* 1995; 29: 1215-1221.
- [62]Inoue K, Kurokawa M, Nishikawa S, Tsukada M. Use of *Bombyx mori* silk fibroin as a substratum for cultivation of animal cells. *J Biochem Biophys Meth* 1998; 37:159-164.
- [63]Hanawa T, Watanabe A, Tsuchiya T, Ikoma R, Hidaka M, Sugihara M. New oral dosage form for elderly patients: preparation and characterization of silk fibroin gel. *Chem Pharm Bull* 1995; 43: 284-288.
- [64]Hanawa T, Watanabe A, Tsuchiya T, Ikoma R, Hidaka M, Sugihara M. New oral dosage form for elderly patients.II. Release behavior of benfotiamine from silk gel. *Chem Pharm Bull* 1995; 43: 872-875.
- [65]Yeo JH, Lee KG, Kim HC, Oh YL, Kim AJ, Kim SY. The effects of PVA/chitosan/fibroin (PCF)-blended spongy sheets on wound healing in rats. *Biol Pharm Bull* 2000; 23: 1220-1223.
- [66]Lammel AS, Hu X, Park SH, Kaplan DL, Scheibel TR. Controlling silk fibroin particle features for drug delivery. *Biomaterials* 2010; 31: 4583-4591.
- [67]Yan HB, Zhang YQ, Ma YL, and Zhou L X. Biosynthesis of insulin-silk fibroin nanoparticles conjugates and *in vitro* evaluation of a drug delivery system. *J Nanopart Res* 2009; 11:1937 -1152.

- [68]Chen M, Shao Z, Chen X. Paclitaxel-loaded silk fibroin nanospheres. *J Biomed Mater Res A*. 2012; 100: 203-210.
- [69]Deepak T, Michel D, Yashwant P. Nanoparticulate drug delivery systems. New York: Informa Healthcare USA 2007; 166:51-60.
- [70]Letchford K, Burt H. A review of the formation and classification of amphiphilic block copolymer nanoparticulate structures: micelles, nanospheres, nanocapsules and polymersomes. *Eur J Pharm Biopharm* 2007; 65: 259-269.
- [71]Asadi H, Rostamizadeh K, Salari D, Hamidi M. Preparation and characterization of tri-block poly(lactide)-poly(ethylene glycol)-poly(lactide) nanogels for controlled release of naltrexone. *Int J Pharm* 2011; 416: 356-364.
- [72]Vonarbourg A, Passirani C, Saulnier P, Benoit JP. Parameters influencing the stealthiness of colloidal drug delivery systems. *Biomaterials* 2006; 27: 4356-4373.
- [73]Dunn SE, Brindley A, Davis SS, Davies MC, Illum L. Polystyrene-poly (ethylene glycol)(PS-PEG2000) particles as model systems for site specific drug delivery. 2. The effect of PEG surface density on the *in vitro* cell interaction and *in vivo* biodistribution. *Pharm Res* 1994; 11: 1016-1022.
- [74]Wang XH, Sui SC, Yan YN, Zhang RJ. Design and fabrication of PLGA sandwiched cell/fibrin constructs for complex organ regeneration. *J Bioact*

Compat Polym 2010; 25: 229-240.

- [75]Agrawal CM, Athanasiou KA. Technique to control pH in vicinity of biodegrading PLA-PGA implants. *J Biomed Mater Res* 1997; 38: 105-14.
- [76]Cardone RA, Casavola V, Reshkin SJ. The role of disturbed pH dynamics and the Na⁺/H⁺ exchanger in metastasis. *Nat Rev Cancer* 2005; 5: 786-795.
- [77]Bulmus V, Woodward M, Lin L, Murthy N, Stayton P, Hoffman A. A new pH-responsive and glutathione-reactive, endosomal membrane-disruptive polymeric carrier for intracellular delivery of biomolecular drugs. *J Control Release* 2003; 93:105-120.
- [78]Kim D, Lee ES, Oh KT, Gao ZG, Bae YH. Doxorubicin-loaded polymeric micelle overcomes multidrug resistance of cancer by double-targeting folate receptor and early endosomal pH. *Small* 2008; 4: 2043-2050.
- [79]Lu Y, Low PS. Folate-mediated delivery of macromolecular anticancer therapeutic agents. *Adv Drug Deliv Rev* 2002; 54: 675-693.
- [80]Pu X, Liu J, Guo Y, Yan X, Yang H, Yuan Q. Study progression in polymeric micelles for the targeting delivery of poorly soluble anticancer agents to tumor. *Asian J Pharm Sci* 2012; 7: 1-17
- [81]Low PS, Antony AC. Folate receptor-targeted drugs for cancer and inflammatory diseases. *Adv Drug Deliv Rev* 2004; 56: 1055-1058.
- [82]Zhao XB, Lee RJ. Tumor-selective targeted delivery of genes and antisense oligodeoxyribonucleotides via the folate receptor. *Adv Drug Deliv Rev* 2004; 56: 1193-1204.

- [83] Wang F, Chen Y, Zhang D, Zhang Q, Zheng D, Hao L, Liu Y, Duan C, Jia L, Liu G. Folate-mediated targeted and intracellular delivery of paclitaxel using a novel deoxycholic acid-O-carboxymethylated chitosan-folic acid micelles. *Int J Nanomedicine* 2012; 7: 325-337.
- [84] Lee ES, Na K, Bae YH. Polymeric micelle for tumor pH and folate-mediated targeting. *J Control Release* 2003; 91: 103-113.
- [85] Mansouri S, Cuie Y, Winnik F, Shi Q, Lavigne P. Characterization of folate-chitosan-DNA nanoparticles for gene therapy. *Biomaterials* 2006; 27: 2060-2065.
- [86] Oyewumi MO, Yokel RA, Jay M, Coakley T, Mumper RJ. Comparison of cell uptake, biodistribution and tumor retention of folate-coated and PEG-coated gadolinium nanoparticles in tumor-bearing mice. *J Control Release* 2004; 95: 613-626.
- [87] Zhao P, Wang H, Yu M, Cao S, Zhang F, Chang J, Niu R. Paclitaxel-loaded, folic-acid-targeted and TAT-peptide-conjugated polymeric liposomes: *in vitro* and *in vivo* evaluation. *Pharm Res* 2010; 27: 1914-1926.
- [88] Grabnar PA, Kristl J. The manufacturing techniques of drug-loaded polymeric nanoparticles from preformed polymers. *J Microencapsul* 2011; 28: 323-335.
- [89] Zhang YQ, Shen WD, Xiang RL, Zhuge LJ, Gao WJ and Wang WB. Formation of silk fibroin nanoparticles in water-miscible organic solvent and their characterization. *J Nanopart Res* 2007; 9: 885-900.

- [90]Cao ZB, Chen X, Yao JR, Huang L, Shao ZZ. The preparation of regenerated silk fibroin microspheres. *Soft Matter* 2007; 3: 910-915.
- [91]Xie R, Wu H, Xu J, Deng Q. The preparation of silk fibroin drug-loading microspheres. *J Fiber Bioeng Inf* 2008; 1: 73-80.
- [92]Wang X, Wenk E, Matsumoto A, Meinel L, Li C, Kaplan DL. Silk microspheres for encapsulation and controlled release. *J Control Release* 2007; 117: 360-370.
- [93]Breslauer DN, Muller SJ, Lee LP. Generation of monodisperse silk microspheres prepared with microfluidics. *Biomacromolecules* 2010; 11: 643-647.
- [94]Hirenkumar K. Makadia and Steven J. Siegel.2; Poly lactic-co-glycolic acid (PLGA) as biodegradable controlled drug delivery carrier. *Polymers* 2011, 3, 1377-1397.
- [95]Soppimath KS, Aminabhavi TM, Kulkarni AR, Rudzinski WE. Biodegradable polymeric nanoparticles as drug delivery devices. *J Control Release* 2001; 70: 1-20.
- [96]Bindschaedler C, Gurny R, Doelker E. Process for preparing a powder of water-insoluble polymer which can be redispersed in a liquid phase, the resulting powder and utilization thereof. US Patent 4968350, 1990.
- [97]Rao JP, Geckeler KE. Polymer nanoparticles: preparation techniques and size control parameters. *Prog Polym Sci* 2011; 36: 887-913.
- [98]Reis CP, Neufeld RJ, Ribeiro AJ, Veiga F. Nanoencapsulation I. Methods for

- preparation of drug-loaded polymeric nanoparticles. *Nanomedicine* 2006; 2: 8-21.
- [99] Fessi H, Puisieux F, Devissaguet JP, Ammoury N, Benita S. Nanocapsule formation by interfacial polymer deposition following solvent displacement. *Int J Pharm* 1989; 55: R1-4.
- [100] Govender T, Stolnik S, Garnett MC, Illum L, Davis SS. PLGA nanoparticles prepared by nanoprecipitation: drug loading and release studies of a water soluble drug. *J Control Release* 1999; 57: 171-185.
- [101] Vehring R. Pharmaceutical particle engineering via spray drying. *Pharm Res* 2007; 25: 999-1022.
- [102] Mansour HM, Rhee YS, Wu X. Nanomedicine in pulmonary delivery. *Int J Nanomedicine* 2009; 4: 299-319.
- [103] Shariati A, Peters CJ. Recent developments in particle design using supercritical fluids, *Curr Opin Solid State Mater Sci* 2003; 7: 371-383.
- [104] Kumar SK, Johnston. KP. Modeling the solubility of solids in supercritical fluids with density as the independent variable. *J Supercrit Fluids* 1988; 1: 15-22.
- [105] Abbas KA, Mohamed A, Abdulami ASR, Abas HA. A review on supercritical fluid extraction as new analytical method. *Am J Biochem & Biotech* 2008; 4: 345-353.
- [106] Chen AZ, Pu XM, Kang YQ, Liao L, Yao YD, Yin GF. Preparation of 5-fluorouracil-poly(L-lactide) microparticles using solution-enhanced

- dispersion by supercritical CO₂. *Macromol Rapid Commun* 2006; 27: 1254-1259.
- [107] Kang YQ, Wu J, Yin GF, Huang ZB, Yao YD, Liao XM, Chen AZ, Pu XM. Preparation, characterization and *in vitro* cytotoxicity of indomethacin-loaded PLLA/PLGA microparticles using supercritical CO₂ technique. *Eur J Pharm Biopharm* 2008; 70: 85-97.
- [108] Hong HL, He WZ, Suo QL, Shan A. Progress in supercritical fluid precipitation technology used for preparation of microparticles. *Progress in chemistry* 2005; 17: 89-792.
- [109] Blasig A, Shi C, Enick RM. Effect of concentration and degree of saturation on RESS of a CO₂-soluble fluoropolymer. *Ind Eng Chem Res* 2002; 41: 4976-4983.
- [110] Rodrigues M, Peirico N, Matos H, Azevedo EG, Lobato MR, Almeida AJ. Microcomposites theophylline/hydrogenated palm oil from a PGSS process for controlled drug delivery systems. *J Supercrit Fluids* 2004; 29:175-184.
- [111] Zhao XH, Zu YG, Li QY, Wang MX, Zu BS, Zhang XN, Jiang R, Zu CL. Preparation and characterization of camptothecin powder micronized by a supercritical antisolvent (SAS) process. *J Supercrit Fluids* 2010; 51: 412-419.
- [112] Mishima K. Biodegradable particle formation for drug and gene delivery using supercritical fluid and dense gas. *Adv Drug Deliv Rev* 2008; 14; 60:

411-32.

- [113] Jung J. and Perrut M. Particle design using supercritical fluids: Literature and patent survey. *J Supercrit Fluids* 2001; 20: 179-219.
- [114] Rantakylä M. Particle production by supercritical antisolvent processing techniques. PhD thesis, Helsinki: University of Technology, 2004.
- [115] Knez Z, Weidner E. Particles formation and particle design using supercritical fluids. *Curr Opin Solid State Mater Sci* 2003; 7: 353-361.
- [116] Davies OR, Lewis AL, Whitaker MJ, Tai H, Shakesheff KM, Howdle SM. Applications of supercritical CO₂ in the fabrication of polymer systems for drug delivery and tissue engineering. *Adv Drug Deliv Rev* 2008; 60: 373-387.
- [117] Pourmortazavi SM, Hajimirsadeghi SS Application of supercritical carbon dioxide in energetic materials processes: A review. *Ind. Eng. Chem. Res* 2005; 44: 6523-6533.
- [118] Yeo SD, Kiran E. Formation of polymer particles with supercritical fluids: A review. *J Supercrit Fluids* 2005; 34: 287-308.
- [119] Gallagher PM, Coffey MP, Krukonis VJ, Klasutis N. Gas antisolvent recrystallization: new process to recrystallize compounds insoluble in supercritical fluids. *ACS Symp Ser* 1989; 406: 334-354.
- [120] Yu WL, Xia F, Jin HY, Lin CC, Zhan YP. Production of submicroparticles of β -sitosterol using an aerosol solvent extraction system.

Chin J Chem Eng 2008; 16; 956-960.

- [121] Liu XW, Li ZY, Han B and Yuan TL. Supercritical antisolvent precipitation of microparticles of quercetin. Chin J Chem Eng 2005; 13: 128-130.
- [122] Kim MS, Lee S, Park JS, Woo JS, Hwang SJ. Micronization of cilostazol using supercritical antisolvent (SAS) process: Effect of process parameters. Powder Technol 2007; 177: 64-70.
- [123] Hanna, M., York, P. Method and apparatus for the formation of particles, WO 95/01221, 1995.
- [124] Suo QL, He WZ, Huang YC, Li CP, Hong HL, Li YX, Zhu MD. Micronization of the natural pigment-bixin by the SEDS process through prefilming atomization. Powder Technol 2005; 154: 110-115.
- [125] Kang YQ, Yin GF, Ping OY, Huang ZB, Yao YD, Liao XM, Chen AZ, Pu XM. Preparation of PLLA/PLGA microparticles using solution enhanced dispersion by supercritical fluids (SEDS). J Colloid Interface Sc 2008; 322: 87-94.
- [126] Sun YP. Supercritical fluid technology in materials science and engineering. Marcel Dekker, Inc. 2002: 445-446.
- [127] Chen AZ. Study of poly(L-Lactide) based drug delivery system by supercritical fluid technology. PhD thesis. Sichuan: Sichuan University. 2007
- [128] Ghaderi R, Artursson P, Carlfors J. Preparation of biodegradable microparticles using solution-enhanced dispersion by supercritical fluids

- (SEDS). *Pharm Res* 1999; 16: 676-681.
- [129] Chen AZ, Pu XM, Kang YQ, Liao L, Yao YD, Yin GF. Study of poly(L-lactide) microparticles based on supercritical CO₂. *J Mater Sci Mater Med* 2007; 18: 2339-2345.
- [130] Hanna M, York P. Patent WO 98/36825, 1998.
- [131] Pyo D. Two Different shapes of insulin microparticles produced by solution enhanced dispersion supercritical fluid (SEDS) process. *Bull Korean Chem Soc* 2009; 30: 1215-1217.
- [132] Chen AZ, Li Y, Chau FT, Lau TY, Hu JY, Zhao Z, Mok DKW. Application of organic nonsolvent in the process of solution-enhanced dispersion by supercritical CO₂ to prepare puerarin fine particles. *J Supercrit Fluids* 2009; 49: 394-402.
- [133] Kang Y, Wu J, Yin G, Huang Z, Liao X, Yao Y, Ouyang P, Wang H, Yang Q. Characterization and biological evaluation of paclitaxel-loaded poly(L-lactic acid) microparticles prepared by supercritical CO₂. *Langmuir* 2008; 24: 7432-7441.
- [134] Kalogiannis CG, Michailof CM, Panayiotou CG. Microencapsulation of amoxicillin in poly(L-lactic acid) by supercritical antisolvent precipitation. *Ind Eng Chem Res* 2006; 45: 8738-8743
- [135] Ghaderi R, Artursson P, Carlfors J. A new method for preparing biodegradable microparticles and entrapment of hydrocortisone in dl-PLG microparticles using supercritical fluids. *Eur J Pharm Sci* 2000; 10: 1-9.

- [136] Chen AZ, Kang YQ, Pu XM, Yin GF, Li Y, Hu JY. Development of Fe₃O₄-poly(L-lactide) magnetic microparticles in supercritical CO₂. *J Colloid Interface Sci* 2009; 330: 317-322.
- [137] Toropainen T, Velaga S, Heikkilä T, Matilainen L, Jarho P, Carlfors J, Lehto VP, Järvinen T, Järvinen K. Preparation of budesonide/gamma-cyclodextrin complexes in supercritical fluids with a novel SEDS method. *J Pharm Sci* 2006; 95: 2235-2245.
- [138] Whitaker MJ, Hao J, Davies OR, Serhatkulu G, Stolnik-Trenkic S, Howdle SM, Shakesheff KM. The production of protein-loaded microparticles by supercritical fluid enhanced mixing and spraying. *J Control Release* 2005; 101: 85-92.
- [139] Zhao Z, Chen AZ, Li Y, Hu JY, Liu X, Li JS, Zhang Y, Li G, Zheng ZJ. Fabrication of silk fibroin nanoparticles for controlled drug delivery. *J Nanopart Res* 2012; 14:736-745.
- [140] Zhao XH, Chen XQ, Zu YG, Jiang R, Zhao DM. Recrystallization and micronization of taxol using the supercritical antisolvent (SAS) process. *Ind Eng Chem Res* 2012; 51: 9591-9597.
- [141] Reverchon E, De Marco I. Mechanisms controlling supercritical antisolvent precipitates morphology. *Chem Eng J* 2011; 169: 358-370.
- [142] He WZ, Jiang ZH, Suo QL, Li GM. Mechanism of dispersing an active component into a polymeric carrier by the SEDS-PA process. *J Mater Sci* 2010; 45: 467-474.

- [143] Tenorio A, Gordillo MD, Pereyra CM, Martínez de la Ossa EJ. Screening design of experiment applied to supercritical antisolvent precipitation of amoxicillin. *J Supercrit Fluids* 2008; 44: 230-237.
- [144] Wang Q, Guan YX, Yao SJ, Zhu ZQ. Microparticle formation of sodium cellulose sulfate using supercritical fluid assisted atomization introduced by hydrodynamic cavitation mixer. *Chem Eng J* 2010; 159: 220-229.
- [145] Reverchon E, De Marco I. Supercritical antisolvent precipitation of cephalosporins. *Powder Technol* 2006; 164: 139-146.
- [146] Reverchon E, Della Porta G, De Marco I. Role of phase behavior and atomization in the supercritical antisolvent precipitation. *Ind Eng Chem Res* 2003; 42: 6406-6414.
- [147] Braeuer A, Dowy S, Torino E, Rossmann M, Luther SK, Schluecker E, Leipertz A, Reverchon E. Analysis of the supercritical antisolvent mechanisms governing particles precipitation and morphology by in situ laser scattering techniques. *Chem Eng J* 2011; 173: 258-266.
- [148] Wang Q, Guan YX, Yao SJ, Zhu ZQ. Controllable preparation and formation mechanism of BSA microparticles using supercritical assisted atomization with an enhanced mixer. *J Supercrit Fluids* 2011; 56: 97-104.
- [149] Montes A, Tenorio A, Gordillo MD, Pereyra CM, de la Ossa EJM. Supercritical antisolvent precipitation of ampicillin in complete miscibility conditions. *Ind Eng Chem Res* 2011; 50: 2343-2347.
- [150] Jin HY, Hemingway M, Xia F, Li NS, Zhao YP. Production

of β -Carotene nanoparticles by the solution enhanced dispersion with enhanced mass transfer by ultra-sound in supercritical CO₂ (SEDS-EM). Ind Eng Chem Res 2011; 50: 13475-13484.

- [151] Kalani M, Yunus R. Application of supercritical antisolvent method in drug encapsulation: a review. Int J Nanomed 2011; 6: 1429-1442.
- [152] Lee BM, Kim SJ, Lee BC, Kim HS, Kim H, Lee YW. Preparation of micronized β -HMX using supercritical carbon dioxide as antisolvent. Ind Eng Chem Res 2011; 50: 9107-9115.
- [153] Amiraliyan N, Nouri M, Haghghat Kish M. Structural characterization and mechanical properties of electrospun silk fibroin nanofiber mats. Polym Sci Ser A 2010; 52: 407-412.
- [154] Yang L, Kuang J, Wang J, Li Z, Zhang LM. Loading and *in vitro* controlled release of indomethacin using amphiphilic cholesteryl-bearing carboxymethyl-cellulose derivatives. Macromol Biosci 2008; 8: 279-286.
- [155] Zhang JX, Yan MQ, Li XH, Qiu LY, Li XD, Li XJ, Jin Y, Zhu KJ. Local delivery of indomethacin to arthritis-bearing rats through polymeric micelles based on amphiphilic polyphosphazenes. Pharm Res 2007; 24: 1944-1953.
- [156] Chen JP, Chen SH, Lai GJ. Preparation and characterization of biomimetic silk fibroin/chitosan composite nanofibers by electrospinning for osteoblasts culture. Nanoscale Res Lett. 2012; 7: 170-180.
- [157] Bessa PC, Balmayor ER, Hartinger J, Zanoni G, Dopler D, Meinel A, Banerjee A, Casal M, Redl H, Reis RL, van Griensven M. Silk fibroin

- microparticles as carriers for delivery of human recombinant bone morphogenetic protein-2: *in vitro* and *in vivo* bioactivity. *Tissue Eng Part C Methods* 2010; 16: 937-945.
- [158] Zhang XD, Guo ML, Wu HY, Sun YM, Ding YQ, Feng X, Zhang LA. Irradiation stability and cytotoxicity of gold nanoparticles for radiotherapy. *Int J Nanomedicine* 2009; 4: 165-73.
- [159] Wei K, Kim BS, Kim LS. Fabrication and biocompatibility of electrospun silk biocomposites. *Membranes* 2011; 1: 275-298.
- [160] Yanagihara K, Terada S, Miki M, Sasaki M, Yamada H. Effect of the silk protein sericin on the production of adenovirus-based gene-therapy vectors. *Biotechnol Appl Biochem*. 2006; 45:59-64.
- [161] Gwinn MR, Vallyathan V. Nanoparticles: Health effects-pros and cons. *Environ Health Perspect* 2006; 114: 1818-1825.
- [162] Apopa PL, Qian Y, Shao R, Guo NL, Schwegler-Berry D, Pacurari M, Porter D, Shi X, Vallyathan V, Castranova V, Flynn DC. Iron oxide nanoparticles induce human microvascular endothelial cell permeability through reactive oxygen species production and microtubule remodeling. *Part Fibre Toxicol* 2009; 6: 1-14.
- [163] Lum H, Roebuck KA. Oxidant stress and endothelial cell dysfunction. *Am J Physiol Cell Physiol* 2001; 280: C719-741.
- [164] Naqvi S, Samim M, Abdin M, Ahmed FJ, Maitra A, Prashant C, Dinda AK. Concentration-dependent toxicity of iron oxide nanoparticles mediated

- by increased oxidative stress. *Int J Nanomedicine*. 2010; 5: 983-989.
- [165] Varshosaz J, Hassanzadeh F, Mahmoudzadeh M, Sadeghi A. Preparation of cefuroxime axetil nanoparticles by rapid expansion of supercritical fluid technology. *Powder Technol* 2009; 189: 97-102.
- [166] Reverchon E, De Marco I, Adami R, Caputo G. Expanded micro-particles by supercritical antisolvent precipitation: Interpretation of results. *J Supercrit Fluids* 2008; 44: 98-108.
- [167] Chen AZ, Li Y, Chau FT, Lau TY, Hu JY, Zhao Z, Mok DK. Microencapsulation of puerarin nanoparticles by poly(l-lactide) in a supercritical CO₂ process. *Acta Biomater*. 2009; 5: 2913-2919.
- [168] Hu K, Lv Q, Cui FZ, Xu L, Jiao YP, Wang Y, Feng QL, Wang HL and Huang LY. A novel poly(L-lactide) (PLLA)/fibroin hybrid scaffold to promote hepatocyte viability and decrease macrophage responses. *J Bioact Compat Polym*.2007; 22: 395-410.
- [169] Chen G, Zhou P, Mei N, Chen X, Shao Z, Pan L, Wu C. Silk fibroin modified porous poly(epsilon-caprolactone) scaffold for human fibroblast culture *in vitro*. *J Mater Sci Mater Med*. 2004; 15: 671-677.
- [170] Niu L, Zou R, Liu QD, Li L, Chen XM, and Chen ZQ. A novel nanocomposite particle of hydroxyapatite and silk fibroin: biomimetic synthesis and its biocompatibility. *J Nanomater* 2010; 2010: 729457. doi:10.1155/2010/729457.
- [171] Höcherl A, Dass M, Landfester K, Mailänder V, Musyanovych A.

Competitive cellular uptake of nanoparticles made from polystyrene, poly(methyl methacrylate), and polylactide. *Macromol Biosci.* 2012; 12: 454-64.

- [172] Sundaram S, Roy SK, Ambati BK, Kompella UB. Surface-functionalized nanoparticles for targeted gene delivery across nasal respiratory epithelium. *FASEB J.* 2009; 23: 3752-3765.
- [173] Saltan N, Kutlu HM, Hür D, Işcan A, Say R. Interaction of cancer cells with magnetic nanoparticles modified by methacrylamido-folic acid. *Int J Nanomedicine* 2011; 6: 477-484.
- [174] Cai K, Yao K, Lin S, Yang Z, Li X, Xie H, Qing T, Gao L. Poly(D,L-lactic acid) surfaces modified by silk fibroin: effects on the culture of osteoblast in vitro. *Biomaterials* 2002; 23:1153-1160.
- [175] Zhou P, Pan LF, Liu S, Yang HX. Enhanced cell affinity of the silk fibroin-modified PHBHHx material. *J Mater Sci Mater Med.* 2009; 20: 1743-51.
- [176] Alexis F, Pridgen E, Molnar LK, Farokhzad OC. Factors affecting the clearance and biodistribution of polymeric nanoparticles. *Mol Pharm* 2008; 5: 505-515.
- [177] Hou Z, Zhan C, Jiang Q, Hu Q, Li L, Chang D, Yang X, Wang Y, Li Y, Ye S, Xie L, Yi Y, Zhang Q. Both FA- and mPEG-conjugated chitosan nanoparticles for targeted cellular uptake and enhanced tumor tissue distribution. *Nanoscale Res Lett* 2011; 6: 563-573.
- [178] Danhier F, Lecouturier N, Vroman B, Jérôme C, Marchand-Brynaert

- J, Feron O, Pr at V. Paclitaxel-loaded PEGylated PLGA-based nanoparticles: *in vitro* and *in vivo* evaluation. *J Control Release* 2009; 133: 11-17.
- [179] Lv PP, Wei W, Yue H, Yang TY, Wang LY, Ma GH. Porous quaternized chitosan nanoparticles containing paclitaxel nanocrystals improved therapeutic efficacy in non-small-cell lung cancer after oral administration. *Biomacromolecules* 2011; 12: 4230-4239.
- [180] Singla AK, Garg A, Aggarwal D. Paclitaxel and its formulations. *Int J Pharm* 2002; 235: 179-192.
- [181] Yang T, Choi MK. Preparation and evaluation of paclitaxel-loaded PEGylated immunoliposome. *J Control Release* 2007; 120: 169-177.
- [182] Liggins RT, Burt HM. Paclitaxel-loaded poly (L-lactic acid) nanospheres 3: blending low and high molecular weight polymers to control morphology and drug release. *Int J Pharm* 2004; 282: 61-71.
- [183] Zhang Z, Feng SS. The drug encapsulation efficiency, *in vitro* drug release, cellular uptake and cytotoxicity of paclitaxel-loaded poly(lactide)-tocopheryl polyethylene glycol succinate nanoparticles. *Biomaterials* 2006; 27: 4025-4033.
- [184] Huh KM, Min HS, Lee SC, Lee HJ, Kim S, Park K. A new hydrotopic block copolymer micelle system for aqueous solubilization of paclitaxel. *J Control Release* 2008; 126: 122-129.
- [185] Patil YB, Toti US, Khdair A, Ma L, Panyam J. Single-step surface functionalization of polymeric nanoparticles for targeted drug delivery.

- Biomaterials 2009; 30: 859-866.
- [186] Keresztessy Z, Bodnar M, Ber E, Hajdu I, Zhang M, Hartmann JF, Minko T and Borbély J. Self-assembling chitosan/poly-gamma glutamic acid nanoparticle. Colloid Polym Sci 2009; 287: 759-765.
- [187] Brannon-Peppas L, Blanchette JO. Nanoparticle and targeted systems for cancer therapy. Adv Drug Deliv Rev 2004; 56: 1649-1659.
- [188] Wu W, Zheng Y, Wang R, Huang W, Liu L, Hu X, Liu S, Yue J, Tong T, Jing X. Antitumor activity of folate-targeted, paclitaxel-loaded polymeric micelles on a human esophageal EC9706 cancer cell line. Int J Nanomedicine 2012; 7: 3487-3502.
- [189] Shin JY, Yang Y, Heo P, Lee JC, Kong B, Cho JY, Yoon K, Shin CS, Seo JH, Kim SG, Kweon DH. pH-responsive high-density lipoprotein-like nanoparticles to release paclitaxel at acidic pH in cancer chemotherapy. Int J Nanomedicine 2012; 7: 2805-2816.
- [190] Zheng C, Zheng M, Gong P, Jia D, Zhang P, Shi B, Sheng Z, Ma Y, Cai L. Indocyanine green-loaded biodegradable tumor targeting nanoprobe for *in vitro* and *in vivo* imaging. Biomaterials 2012; 33: 5603-5609.
- [191] Wang F, Chen Y, Zhang D, Zhang Q, Zheng D, Hao L, Liu Y, Duan C, Jia L, Liu G. Folate-mediated targeted and intracellular delivery of paclitaxel using a novel deoxycholic acid-O-carboxymethylated chitosan-folic acid micelles. Int J Nanomedicine. 2012; 7: 325-337.